Spring 5-15-2017

The Effect of Diffusive Transport on Mineral Carbonation in Geologic Carbon Sequestration

Wei Xiong
Washington University in St Louis

WASHINGTON UNIVERSITY IN ST. LOUIS
School of Engineering & Applied Science
Department of Energy, Environmental & Chemical Engineering

Dissertation Examination Committee:

Daniel E. Giammar, Chair
John D. Fortner
Sophia E. Hayes
Young-Shin Jun
Philip Skemer

The Effect of Diffusive Transport on Mineral Carbonation in Geologic Carbon Sequestration

by

Wei Xiong

A dissertation presented to
The Graduate School
of Washington University in
partial fulfillment of the
requirements for the degree
of Doctor of Philosophy

May 2017
St. Louis, Missouri

Table of Contents

Table of Contents ii

List of Figures vii

List of Tables x

Acknowledgements xi

Abstract of the Dissertation xiii

Chapter 1. Introduction 1

1.1. Background 1

1.1.1 Overview of geological carbon sequestration 1

1.1.2 CO_2 storage mechanisms 2

1.1.3 Basalt as a host rock for CO_2 storage 3

1.1.4 Research on carbon sequestration in basalt 5

1.1.5 Knowledge gaps regarding GCS in basalt 7

1.2. Research Objectives 7

1.3. Overview of Dissertation 8

Chapter 2. Carbonate Mineral Formation in Forsterite Powder Packed Beds 10

Abstract 10

2.1 Introduction 10

2.2 Materials and Methods 12

2.2.1 Materials 12
2.2.2 Tubular reactor 12
2.2.3 Analytical methods 13
2.3 Results and Discussion 14
2.3.1 Identification of carbonates 14
2.3.2 Quantification of carbonates 17
2.3.3 Environmental implications 19
Acknowledgements 21
Supporting Information 22
Chapter 3. Carbon Sequestration in Olivine and Basalt Powder Packed Beds 28
Abstract 28
3.1 Introduction 29
3.2 Materials and Methods 30
3.2.1 Materials 30
3.2.2 Packed bed experiments 32
3.2.3 Analytical methods 33
3.2.4 Reaction path modeling 34
3.3 Results and Discussion 35
3.3.1 Olivine packed beds 35
3.3.2 Basalt packed beds 39
3.3.3 Siderite formation 43

3.3.4 Environmental implications 45

Acknowledgements 47

Supporting Information 48

Chapter 4. Carbon Sequestration in Fractured Basalt Cores 61

Abstract 61

4.1 Introduction 62

4.2 Results and Discussion 63

4.2.1 Siderite and Fe-Mg-Ca Carbonate formation 63

4.2.2 Uneven distribution of precipitates 66

4.2.3 Conclusions 73

4.3 Materials and Methods 73

4.3.1 Fractured basalt cores 73

4.3.2 Batch experiments 74

4.3.3 Analytical methods 75

4.3.4 1D reactive transport modeling 76

Acknowledgements 77

Supporting Information 78

Chapter 5. Carbon Sequestration in Grand Ronde Basalt 105

Abstract 105

5.1 Introduction 106

5.2 Materials and Methods 107
5.2.1 Fractured Grand Ronde basalt cores 107
5.2.2 Static batch experiment 108
5.2.3 Analytical Methods 109
5.3 Results and Discussion 110
5.3.1 Identification of precipitates 110
5.3.2 Location of precipitates 114
5.3.3 Quantification of precipitates 117
5.3.4 Implications for carbon sequestration 119
Acknowledgements 121
Supporting Information 122
Chapter 6. Conclusions and Recommendations for Future Work 135
6.1 Conclusions 135
6.1.1 Carbonation in porous powder packed beds 135
6.1.2 Carbonation in fractured basalt rocks 136
6.2 Recommendations for Future Work 137
Appendix 1. Carbonation of Olivine Sinters 138
A1.1 Introduction 138
A1.2 Part of Materials and Methods 139
A1.2.1 Synthesis of starting materials 139
A1.2.2 Fo90 experiments 141

A1.2.3 Post-reaction analysis 142
A1.3 Part of Results 143
A1.3.1 Single cylinder experiments (Fo90_s1 and Fo90_s2) 143
A1.3.2 Fractured cylinder experiment (Fo90_f) 144
A1.4 Part of Discussion 145
A1.4.1 Precipitate composition and morphology 145
A1.4.2 Analysis of post-reaction texture 146
A1.4.3 Implications for Geologic Carbon Sequestration 147
Appendix 2. Flood basalt core reacted in wet-scCO_2 149
A2.1 Introduction 149
A2.2 Materials and Methods 150
A2.2.1 Fractured basalt cores 150
A2.2.2 Static batch experiments 151
A2.2.3 Analytical methods 151
A2.3 Results and Discussion 152
Reference 156

List of Figures

Figure 1.1 Carbon mineral sequestration in fractured basalt 5

Figure 1.2 Overview of two research tasks to investigate CO_2 mineral trapping. 8

Figure 2.1 Raman spectra of solids from a tube packed with forsterite after 3 days of exposure of the tube to water at 100˚C in equilibrium with 100 bar CO_2. The major peaks at 824, 855, and 964Δcm^{-1} correspond to the stretching modes of the Si-O(2), Si-O(3) and Si-O(1) bonds in forsterite[45, 47]. The peaks at 1119 cm^{-1} and 1094 cm^{-1} correspond to the CO_3^{2-} symmetric stretching mode (ν_1) in hydromagnesite and magnesite, respectively.[46, 48] 14

Figure 2.2 Combined Raman spectra for the range of carbonate peaks. The peaks are normalized to the highest forsterite peak at 855 cm^{-1} for semi-quantitative assessment of the carbonate content. 15

Figure 2.3 Profiles of inorganic carbon in the forsterite bed after exposure of the tube to CO_2-rich aqueous solution for reaction times up to 60 days. Each point represents the carbon content of a 0.2 cm-thick layer. 17

Figure 2.4 Total carbon in the tube after exposure of a bed packed with forsterite powder to a CO_2-rich solution at 100˚C in contact with 100 bar CO_2. The total carbon is determined from the depth profiles presented in Figure 2.3. 18

Figure 3.1 Raman spectroscopy on olivine powder packed beds reacted for 15 days in water in equilibrium with 100 bar CO_2 and at 100˚C. The peaks at 1094 cm^{-1} represent magnesite. The patterns are normalized to the similar height of olivine peaks in the range of 800-1000 cm^{-1}. 36

Figure 3.2 Total inorganic carbon accumulated in the powder packed beds of a) olivine and b) basalt. 38

Figure 3.3 SEM SE/BSE images of a) magnesite precipitated on the olivine surface in the 0.8-1.0 cm layer of the 53-106 μm Fo_{90} packed bed, with amorphous silica on the surface, b) magnesite on the tape from the 0.8-1.0 cm layer of the <53 μm Fo_{90} packed bed, c) lizardite formation on the reacted flood basalt from 0-0.3 cm layer, d) rhombohedral siderite in between flood basalt powder from the 0-0.3 cm layer, e) pentagon shape siderite on flood basalt from the 0-0.3 cm layer, with amorphous silica on the surface, f) siderite with the composition by WDS analysis..... 39

Figure 3.4 Raman spectra of the pentagonal carbonate mineral in Figure 3.3e and carbonate standards of siderite, calcite and magnesite (standards details in SI). Spectrum intensity is normalized to the maximum point. The pentagonal precipitate was identified as siderite..... 41

Figure 3.5 Dissolved element concentrations in the 200 mL bulk solution of the batch reactors from experiments with basalt packed beds after 4 weeks at 100˚C and 100 bar CO_2 43

Figure 4.1 Carbonate minerals formed in the milled fracture surfaces of flood basalt after reactions for 40 weeks with a) a siderite precipitate formed at 100˚C in water equilbrated with 100 bar CO_2 and b) Fe-Mg-Ca carbonate formed at 150˚C in water equilibrated with 100 bar CO_2. 64

Figure 4.2 X-ray CT images of a) The flood basalt before reaction, b) cross section near the milled fracture surface, c) cross section of the middle of the fracture and d) cross section near the smooth surface of flood basalt reacted in 100˚C for 40 weeks. e) The flood basalt milled surface view and f) the fracture side view of flood basalt reacted in 150˚C for 40 weeks. g) The serpentinized basalt before reaction and h) after reaction in 100˚C for 40 weeks..... 68

Figure 4.3 a) CT segmentation of precipitate volume fraction in each 5-mm long layer along the fracture in the 40-week flood basalt sample and precipitate point count percentage on the fracture

surface. The point count percentage represents the occurrence of carbonates at 110 different locations across the fracture surface at a given distance from the fracture inlet. b) Predicted siderite volume fraction in each grid cell of the fracture domain of flood basalt reacted at 100˚C in reactive transport modeling. 69

Figure 5.1 Raman spectra of the rod and star shape precipitates formed in Grand Ronde basalt with different carbonate mineral standards from the RRUFF database. 111

Figure 5.2 a) SEM-EDX on a rod-shape precipitate on the surface in 20-week core with gold coating b) SEM-EDX on diamond-shape precipitates in 20-week core with gold coating 112

Figure 5.3 3D view of the 40-week core sample and segmented precipitates 115

Figure 5.4 Pore area percentages on the core cross section and pre- and post-reaction CT images. The entire core porosity based on CT segmentation was 4.04 %, 4.83 % and 2.09 % for the pre-reaction 6-week, 20-week and 40-week core, respectively. 116

Figure 5.5 a) Precipitate area in each round cross section CT slice from segmentation. b) Total precipitate volume in the entire core, in the 100 μm fracture and precipitate volume fraction in the fracture. 118

List of Tables

Table 3.1 Composition of flood basalt (FB) and serpentinized basalt (SB) with percentages (by mass) of constituent minerals[64] 31

Table 3.2 Size and surface areas of materials used in packed bed experiments 32

Table 4.1 Estimated carbonate mineral volume in the 100 μm fracture of the cores reacted for 40weeks..... 66

Table 4.2 Basalt compositions [64] 74

Table 5.1 Grand Ronde basalt sample composition 107

Acknowledgements

I would like to express my greatest gratitude to my Ph.D. advisor, Dr. Daniel Giammar for his guidance through my doctoral research. He is a wise and responsible advisor with profound knowledge in the fields of environmental engineering, aquatic chemistry and geochemistry. I am grateful for his encouragement when I was first involved in the topic of geologic carbon sequestration and his unwavering support through the entire research project in the following years. Without his insight and guidance this dissertation would not have been possible. He is not only a great mentor but also an organized and principled man, who will always be a role model in my life.

My deepest gratitude expands to Dr. Philip Skemer, Dr. Sophia Hayes, Dr. John Fortner and Dr. Young-Shin Jun, who kindly served as my thesis committee members. Dr. Philip Skemer and Dr. Sophia Hayes are co-PIs of the research project I have been mainly working on during my Ph.D. study. I am fortunate to have the opportunity to work closely with students and researchers from their groups. I would like to thank Dr. Philip Skemer for his advice and support in the geologic aspects in this project. I am thankful to learn about the use of NMR in relevant field from Dr. Sophia Hayes. I would like to give me sincere appreciation to Dr. John Fortner and Dr. Young-Shin Jun for their valuable suggestions on my research.

I am fortunate to have Dr. Rachel Wells as a close collaborator, who has expertise in rock and mineral characterization. I benefited a lot from valuable discussions with Dr. Brian Ellis, who is also a co-PI of this multi-disciplinary research project from University of Michigan. I sincerely appreciate the effort of his students, Anne Menefee and Jubilee Adeoye in our collaborative publications. I also want to thank Dr. Jill Pasteris for her patient and generous assistance in Raman spectroscopy, Dr. Helene Covey for her help in sample preparation, Daniel

Leib and Dr. James Fitzpatrick for their help in X-ray Computed Tomography. I thank Dr. Rolf Brojin and Dr. Jeremy Moore for their help in the early years of my Ph.D. study.

Special thanks to other former and current members of the Aquatic Chemistry Lab, including Dr. Zimeng Wang, Dr. Fei Wang, Dr. Lin Wang, Dr. Vrajesh Mehta, Zezhen Pan, Chao Pan, Yeunook Bae, Anshuman Satpathy, and all the visiting students.

Research funding from the U.S. Department of Energy and Consortium for Clean Coal Utilization at Washington University is gratefully acknowledged.

Finally, I wish to express my thanks to all my family, especially my husband, Dr. Xinyu Lu, who has always been my strongest emotional support with unconditional love.

Wei Xiong

Washington University in St. Louis

May, 2017

ABSTRACT OF THE DISSERTATION

The Effect of Diffusive Transport on Mineral Carbonation in Geologic Carbon Sequestration

by

Wei Xiong

Doctor of Philosophy in Energy, Environmental & Chemical Engineering

Washington University in St. Louis, 2017

Professor Daniel Giammar, Chair

Geologic carbon sequestration (GCS) is an effective method to mitigate environmental problems due to excessive anthropogenic CO_2 emissions. It involves injecting supercritical CO_2 into deep geologic formations in which CO_2 will ultimately be converted to solid carbonate minerals. Basalt is a promising host rock that is rich in the divalent cations Ca, Mg and Fe that are important for mineral trapping of CO_2. Fractures and pores in basalt reservoirs provide substantial surface area for geochemical reactions during carbon sequestration. The transport in fractures and pores is controlled by diffusion. The coupling of diffusive transport and geochemical reactions leads to carbonate mineral formation in these fractures. This research studied the effect of diffusive transport on mineral carbonation in basalt and olivine powder packed bed systems and in systems with fractured basalts at conditions relevant to GCS. Carbonate minerals can form rapidly in basalt within weeks of reaction. For olivine, carbonate minerals precipitated within one day. Carbonate mineral formation is unevenly distributed along diffusion-limited zones as a result of opposing chemical gradients driven by concentration differences between inner part of the zones and the outside bulk solution. Certain regions in the

fracture have maximum amount of carbonate mineral. Carbonate mineral spatial distribution is influenced by a series of factors including mineral composition, mineral grain size, basalt type, temperature and reaction time. Different carbonation products occur in different experiments. Hydromagnesite formed at early reaction times in forsteritic olivine powder packed bed experiments, and magnesite became the only carbonate mineral type after 8 days of reaction. Mg- and Ca-bearing siderite was observed in fractured flood basalt and serpentinized basalt within 6 weeks of reaction. Calcium carbonate minerals that were predominantly aragonite were found in fractured and porous Grand Ronde basalt. The formation of carbonate minerals did not block the transport pathway and end the overall reaction. Though in different extent, carbonation happened in the entire fracture within the longest experimental time in this research.

Chapter 1. Introduction

1.1. Background

1.1.1 Overview of geological carbon sequestration

Global warming is a serious environmental issue due to excessive emissions of greenhouse gases to the atmosphere. CO_2 is the greenhouse gas that makes the largest contribution as a result of human activity.[1] To reduce CO_2 emissions and mitigate environmental problems, carbon capture and storage was brought out as one of the feasible and efficient technological options.[2] The basic idea of carbon capture and storage is to capture CO_2 arising from the combustion of fossil fuels, transport the captured and separated CO_2 to a storage site where it will be stored away from atmosphere for a very long time.[3] Geologic carbon sequestration (GCS) involves injecting CO_2 into deep geological formations for carbon storage. The injected CO_2 must be compressed to a dense fluid state known as supercritical.[3] The critical temperature and pressure of CO_2 are 31˚C and 74 bar.

Geologic carbon sequestration can be undertaken in a variety of reservoirs such as depleted oil and gas reservoirs and deep saline water-saturated reservoir rocks. Most of the completed and ongoing geologic carbon sequestration projects inject CO_2 into sandstones because of their large storage capacity for site selection.[4, 5] StatoilHydro has been injecting 1 million metric tons of CO_2 per year into a sandstone reservoir that lies 1000 m below the sea surface in the North Sea since 1996.[6] Commercial injections into saline sedimentary formations at 1 Mt/year or more have been conducted at Utsira and Snøhvhit, Norway.[7] Since 2014, the

world's first commercial scale post-combustion coal fired carbon capture and storage project was started at the SaskPower Boundary Dam Power Station in Estevan, Saskatchewan, Canada.[8]

1.1.2 CO_2 storage mechanisms

The effectiveness of geological storage depends on multiple trapping mechanisms.[9] When supercritical CO_2 is injected into deep geologic formations, it displaces underground saline water and migrates buoyantly upwards since it is less dense than water.[3] In this process, which is structural or stratigraphic trapping, the upward migration of CO_2 is restrained by low permeability caprocks.[3] When CO_2 moves through porous rocks and displaces brine, some CO_2 can be trapped in the pore spaces by capillary forces, which is residual trapping.[10, 11] The two trapping mechanisms are physical trapping. Geochemical trapping occurs when CO_2 dissolves in brine (solubility trapping) and reacts with dissolved cations to form solid carbonate minerals (mineral trapping). Geochemical trapping eliminates the buoyant drive for CO_2 to move upwards because CO_2 no longer exists as a separate phase.[3]

Dissolution and precipitation are two important steps during geochemical trapping. Dissolved CO_2 acidifies water through the following reaction (Eq. 1.1)[12]:

$$CO_{2(aq)} + H_2O \rightleftharpoons H_2CO_3 \rightleftharpoons HCO_3^- + H^+ \rightleftharpoons CO_3^{2-} + H^+ \quad \text{Eq. 1.1}$$

The dissolution of CO_2 decreases the pH of the solution and accelerates the dissolution of minerals in the host rocks. Further water-mineral reactions provide divalent cations in solution. For example, dissolution of calcium-bearing plagioclase such as anorthite can contribute Ca^{2+} (Eq. 1.2)[12] and olivine can provide Fe^{2+} and Mg^{2+} (Eq. 1.3):

$$CaAl_2Si_2O_8 + 2H^+ + H_2O = Ca^{2+} + Al_2Si_2O_5(OH)_4 \quad \text{Eq. 1.2}$$

$$(Fe,Mg)_2SiO_4 + 4H^+ = 2(Fe,Mg)^{2+} + SiO_2 + H_2O \quad \text{Eq. 1.3}$$

The dissociated bicarbonate and carbonate ions could react with divalent cations in solution, precipitating as carbonate minerals (Eq. 1.4, Eq. 1.5)[12]:

$$(Ca,Mg,Fe)^{2+} + HCO_3^- = (Ca,Mg,Fe)CO_3 + H^+ \quad \text{Eq. 1.4}$$

$$(Ca,Mg,Fe)^{2+} + CO_3^{2-} = (Ca,Mg,Fe)CO_3 \quad \text{Eq. 1.5}$$

Mineral trapping is considered the most permanent form of geologic carbon storage.[13] Mineral carbonation reactions are thermodynamically favored but proceed slowly.[14] Most minerals in sandstone reservoirs are not reactive for carbonation reactions so it may take hundreds to thousands of years for CO_2 mineral trapping to happen.[3] Formations containing richer Ca, Mg and Fe can potentially result in mineral trapping over much shorter time scales.

1.1.3 **Basalt as a host rock for CO_2 storage**

Basalt is a common rock type on Earth, forming the top igneous layer in oceanic crust and covering ~10% of continental surface area, such as the Siberian Traps and the Columbia River Basalt Group.[12, 15, 16] Basalt is composed of basic minerals with the highest potential for CO_2 mineralization, such as olivine, pyroxene, serpentine, plagioclase and basaltic glass.[14] Unlike sandstone reservoirs which have porosity and permeability for physical trapping but limited capacities for mineral trapping, basalt has become a target host rock for geologic carbon sequestration due to its great capacity for mineral carbonation.[14, 17]

Basalt is rich in Ca, Mg and Fe which present in carbon mineralization source minerals, such as olivine, pyroxene and plagioclase feldspar [14]. Olivine is the most reactive among common basalt-forming minerals and can be easily weathered to serpentine. The minerals react with dissolved CO_2 and may form different types of carbonate minerals. Such reactions may generally be formulated as [18] :

$$\underset{\text{Mg-olivine}}{2Mg_2SiO_4} + \underset{\text{Mg-pyroxene}}{Mg_2Si_2O_6} + 4H_2O = \underset{\text{serpentine}}{2Mg_3Si_2O_5(OH)_4} \quad \text{Eq. 4.1}$$

$$\underset{\text{Mg-olivine}}{Mg_2SiO_4} + 2CO_2 = \underset{\text{magnesite}}{2MgCO_3} + SiO_2 \quad \text{Eq. 4.2}$$

$$\underset{\text{Mg-olivine}}{Mg_2SiO_4} + \underset{\text{CaMg-pyroxene}}{CaMgSi_2O_6} + 2CO_2 + 2H_2O = \underset{\text{serpentine}}{Mg_3Si_2O_5(OH)_4} + \underset{\text{magnesite}}{MgCO_3} + \underset{\text{calcite}}{CaCO_3} \quad \text{Eq. 4.3}$$

When CO_2 is injected into basalt reservoirs, it dissolves in underground brine and decreases the pH of the solution, accelerating mineral dissolution. The solution needs to become supersaturated with respect to carbonate minerals in order for those minerals to precipitate. The saturation index is defined as the logarithm of ion activity products over mineral solubility products, showing in Eq. 1.6 and Eq. 1.7, taking magnesite ($MgCO_3$) as an example. The saturation index needs to be at least larger than 0 for the solution to become supersaturated and for precipitates to form.

$$MgCO_3 \rightleftharpoons Mg^{2+} + CO_3^{2-},\ K_{sp,\ magnesite} = \{Mg^{2+}\}_{eq}\{CO_3^{2-}\}_{eq} \quad \text{Eq. 1.6}$$

$$SI = \log \frac{IAP}{K_{sp}} = \log \frac{\{Mg^{2+}\}\{CO_3^{2-}\}}{K_{sp,magnesite}} \quad \text{Eq. 1.7}$$

Fractures and pores in basalt provide substantial surface area for carbonation reactions. In fractures and pores, the transport of fluids is controlled by mass diffusion, allowing cations to accumulate and reach supersaturation status in localized zones. CO_2 mineral trapping in fractured basalt is controlled by the coupling of transport processes and geochemical reactions (Figure 1.3). The concentration difference between the inside of the fracture and the outside bulk solution leads to chemical gradients along the fracture, which can result in spatial distribution of carbonate mineral formation in fractured basalt. Certain locations may be most favorable for

precipitation and block the fracture for further reactions in deeper unreacted zones. Carbonate minerals may form on the surface of the fracture without blocking transport pathways. Stress induced by rapid precipitation may lead to fracturing and subsequent increase in reactive surface area.[12]

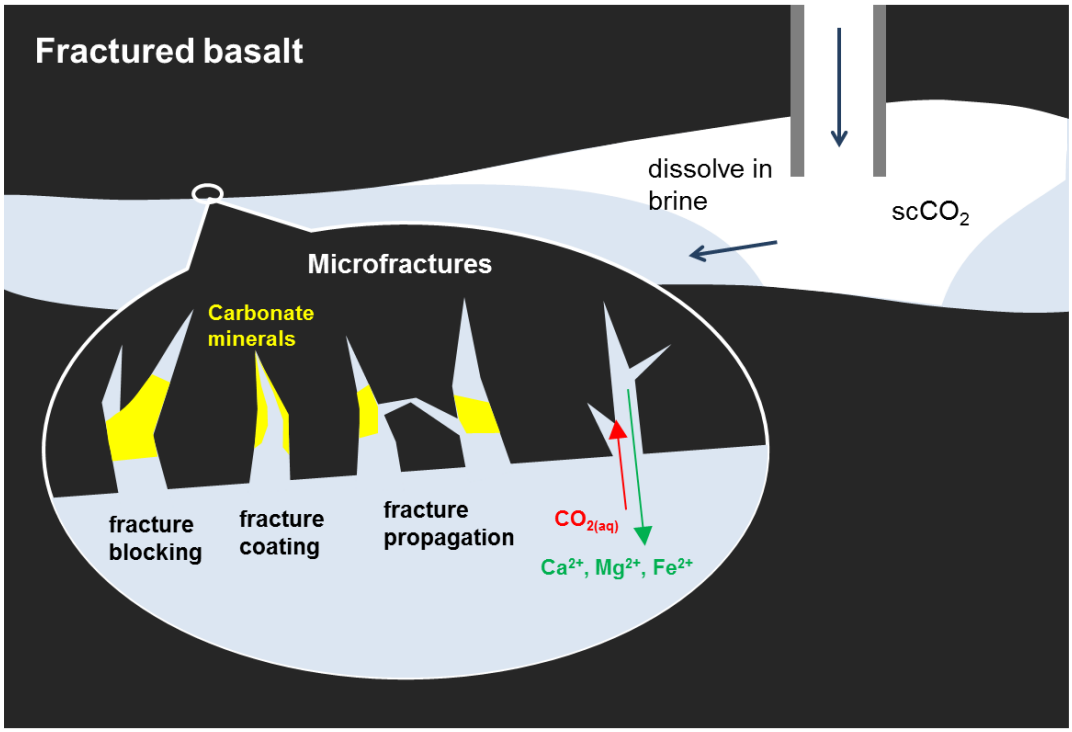

Figure 1.1 Carbon mineral sequestration in fractured basalt

1.1.4 **Research on carbon sequestration in basalt**

Pilot injections of CO_2 into basalt formations have been undertaken. The CarbFix project in Iceland injected 175 tons of pure CO_2 in Phase I and 73 tons of CO_2-H_2S mixture in Phase II at 400~800 m depth basaltic lavas[19]. The injection site is near the Hellisheidi geothermal power plant at east of Reykjavik[19]. CO_2 was released as bubbles at 350-m depth into dwon-flowing water within the injection well so that CO_2 could dissolve in water before entering the basalt

reservoir[20]. Only 5 % of the injected mass is CO_2.[20] The formation water temperature and pH in the injection interval range from 20˚C to 33˚C and from 8.4 to 9.4, and it is oxygen-depleted. [21] It was reported that 95 % of the injected CO_2 into basalt was mineralized to calcite within 2 years.[19] In the BigSky project in Wallula, Washington State, United States, CO_2 is injected as a separate buoyant phase into a porous basaltic layer at more than 800 m depth. Up to 1000 metric tons of CO_2 will be injected into the reservoir formation of which the pre-injection temperature and pressure are 36˚C and 77 bar. CO_2 was stored in tanks and was preheated to 44˚C before injection. Carbon mineralization to ankerite nodules was observed 2 years after injection.[22] The two ongoing pilot-scale basalt injection projects both confirmed rapid carbon mineralization in basalt reservoirs.[23]

In the laboratory, basalt has been studied in different systems in a variety of conditions relevant to geologic carbon sequestration. Previous study discussed the dissolution rate and mechanisms of homogeneous basaltic glass powders from Iceland as a function of pH (1~11) and temperature (6~300˚C).[24] Experiments with the same basaltic glass in CO_2-rich water at 40˚C for up to 260 days suggested the dissolution was incongruent with the overall water composition and secondary mineralogy depended on reaction progress and pH, which is determined by the dissociation of CO_2 and the dissolved ions from basaltic.[25] Different carbonation products were reported in different studies. Fe-bearing magnesite formed on the surface of mid-ocean ridge basalt (MORB) powder during the reaction with CO_2-rich water at 150˚C and 280 bar CO_2 for 2-45 days. Other types of Ca-Mg-Fe carbonate solid solutions were also observed in experimental study with basalt.[26]

1.1.5 **Knowledge gaps regarding GCS in basalt**

Most of the laboratory studies on carbon sequestration in basalt investigated basalt powder or grains in well-mixed systems. In basalt reservoirs, the majority of exposed reactive surfaces are located in pores and along fractures, in which the transport is controlled by mass diffusion. The concentration difference between the diffusion-limited zones and advective or turbulent bulk solution drives geochemical gradients that determine mineral dissolution and carbonate formation. The formation of secondary precipitates may affect the transport pathways, thus influencing further reaction. Our limited understanding of the mechanisms and extent of carbonate mineral formation in fractured basalt poses challenges to accurately estimating the storage capacity of basalt reservoirs and assessing their long-term security.

1.2. Research Objectives

The overall objective of this research is to understand the coupling of diffusive transport and dissolution-precipitation reactions in porous and fractured minerals and rocks at conditions relevant to geologic carbon sequestration. Two specific objectives are listed below.

Objective 1: Determine the timing and location of carbonate precipitation in packed beds of materials with reactive minerals that can promote mineral trapping of CO_2 at conditions relevant to GCS.

Objective 2: Explore the fracture and pore space evolution due to carbonation reactions in fractured basalt rocks at conditions relevant to GCS.

1.3. Overview of Dissertation

This study includes two related main tasks that address the specific research objectives (Figure 1.4). Task 1 is to investigate carbonate mineral formation in a powder porous packed bed in CO_2-rich water at high temperature (100˚C) and high pressure (100 bar CO_2). Task 2 is to explore carbonate mineral formation in low-porosity rock cores with fractures and pores in CO_2-rich water at GCS-related conditions. Both experimental systems examine similar types of minerals and rocks, including forsterite (Mg end-member of olivine), natural olivine and different basalt samples. Both systems mimic the dead-end zones in which transport is controlled by diffusion.

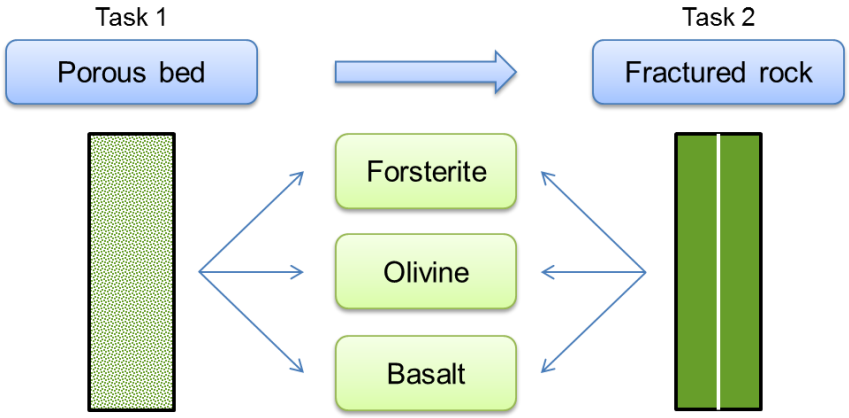

Figure 1.2 Overview of two research tasks to investigate CO_2 mineral trapping.

A set of experiments were designed and conducted to address the two tasks. Chapter 2 and Chapter 3 present experimental studies using porous packed bed system in Task 1. Chapter 2 discusses the timing, location and type of carbonate minerals formed in synthetic forsterite powder packed beds in water equilibrated with 100 bar CO_2 at 100˚C, reacting from 1 day to 60 days. Chapter 3 investigates the particle size and chemical composition effects on mineral

carbonation in olivine and basalt powder packed beds. The work in Chapter 2 and Chapter 3 has been published in two peer-reviewed papers.

Chapter 4 and Chapter 5 include static batch experiments using different types of fractured basalt described in Task 2. Chapter 4 discusses carbon mineral sequestration in artificial dead-end fractures in flood basalt and serpentinized basalt cores in water equilibrated with 100 bar CO_2 in 100˚C or 150˚C for up to 40 weeks. Chapter 5 explores the carbonate minerals formed in fractures and pores in the porous Grand Ronde basalt cores in CO_2-rich water at 100˚C for up to 40 weeks. The work in Chapter 4 is in preparation for a co-authored publication. The reactive transport modeling and CT segmentation in Chapter 4 were done by Brian Ellis' Group, including Anne Menefee and Jubilee Adeoye, at the University of Michigan. The work in Chapter 5 will be submitted to a peer-reviewed journal as a co-authored paper after further analysis is done by Todd Schaef and Jake Horner from Pacific Northwest National Laboratory. Chapter 6 includes conclusions obtained from the overall research makes recommendations for future work.

The two appendices in the end include experimental studies that are relevant to this research topic but may not be published as an independent paper. Appendix 1 contains experimental results to investigate carbonation in low-porosity olivine sintered aggregates. This has become part of a published paper in which I am a co-author. Appendix 2 describes the same fractured flood basalt core as in Chapter 4 reacted in water-saturated CO_2 (i.e., a phase that is predominantly CO_2 with trace amounts of H_2O) at 100˚C and 100 bar. The reaction progress in the wet-CO_2 system is very slow and very limited observable carbonate precipitate was found. The results may not be enough for a full publication, but they may be useful for future study in similar reacting system.

Chapter 2. Carbonate Mineral Formation in Forsterite Powder Packed Beds

This chapter was published in Xiong, W.; Giammar, D., Forsterite Carbonation in Zones with Transport Limited by Diffusion. Environmental Science & Technology Letters 2014, 1, (8), 333-338.[27]

Abstract

Diffusive limitations to transport can significantly influence carbonation processes in geologic carbon sequestration. A tube packed with forsterite and exposed at one end to a CO_2-rich solution at 100˚C and 100 bar CO_2 was used to explore the timing and spatial localization of carbonate precipitation along a one-dimensional diffusion-limited zone. The identity and quantity of carbonate mineral formation as a function of depth were determined using Raman spectroscopy and total carbon analysis. Carbonate mineral precipitation was observed as early as 1 day. Hydromagnesite formed before magnesite. Carbonate precipitation was spatially localized with the highest amount formed at 0.5 cm into the packed bed. Magnesite precipitation did not block the flux of carbon deeper into the tube, although the overall carbonation rate did decline after 30 days.

2.1 Introduction

Geologic carbon sequestration (GCS) can mitigate environmental problems caused by anthropogenic CO_2 emissions by injecting captured CO_2 into deep geologic formations. Storage mechanisms include stratigraphic and structural trapping, solubility trapping, hydrodynamic trapping, and mineral trapping[3]. During mineral trapping, dissolved CO_2 reacts with cations

released from silicate minerals to form carbonate minerals. Most current GCS reservoirs are sandstone and carbonate saline aquifers[3, 28, 29] that have favorable porosity and permeability for CO_2 injection but limited capacities for mineral trapping. Mafic (i.e. rich in Fe and Mg) basalt and peridotite formations have drawn attention as alternative storage sites because of their greater potential for mineral carbonation[12, 17, 30, 31]. Pilot-scale CO_2 injections into basalts have been conducted in Washington state and Iceland[32].

Forsterite (Mg_2SiO_4) reaction in CO_2-water systems involves magnesium release followed by precipitation of magnesium carbonate solids.[33-38] Because CO_2-water interactions with forsterite in basalt, peridotite, and other rocks will occur along fractures of various dimensions and lengths, diffusive transport can limit the overall extent of reactions, and reaction rates in diffusion-limited zones can be very different from those at volume-averaged conditions.[39-41] In experiments with peridotite cubes, carbonate mineral formation was only observed along fractures, and the overall porosity decreased by 50% when 10% of the olivine had been converted to carbonates.[42] CO_2-mineralization may be more viable in open systems with fluid flow carrying away the products of silicate mineral dissolution, while fracture clogging could limit peridotite carbonation in a closed system.[43]

The objective of this study was to investigate the impact of geochemical gradients caused by diffusive limitations to transport on the timing and spatial distribution of carbonate precipitation. A one-dimensional diffusion-limited packed bed was studied at a temperature and pressure relevant to GCS.

2.2 Materials and Methods

2.2.1 Materials

Forsterite powder (99% Mg_2SiO_4, Alfa Aesar) was sonicated in ethanol for 10 min to remove fine particles and any organic contamination. Settling and decanting in ultrapure water (resistivity>18.2 MΩ·cm) ten times isolated particles in the 5-40 μm fraction , but some particles finer than 5 μm remained associated with the larger particle surfaces (Figure S2.1). The specific surface area (SSA) determined by BET-N_2 adsorption was 3.7 m^2/g, which is 10 times larger than the value corresponding to 5 μm forsterite spheres and is consistent with the presence of the finer particles.

2.2.2 Tubular reactor

The pretreated forsterite was wet packed to 3 cm in a borosilicate glass tube (1 cm diameter and 5 cm length). The porosity was 0.48 ± 0.03. The tube was fixed vertically to the head of a high temperature high pressure reactor (Parr Instrument Company) so that it would be immersed in CO_2-rich solution when the reactor was sealed. A 300 mL PTFE liner with 200 mL ultrapure water was put into a stainless steel pressure vessel that was then attached to the reactor head and heated to 100˚C. A syringe pump (500D, Teledyne Isco) provided a constant CO_2 pressure (100 bar) on the headspace (Figure S2.2a). For most geologic systems, at the depth (1 km) corresponding to 100

bar the temperature from the geothermal gradient would be around 50˚C;[44] however, experiments were performed at 100˚C because this allowed for faster laboratory investigation

and because the carbonation reaction is exothermic,[18] which would lead to *in situ* temperatures higher than those from the natural geothermal gradient.

The 200 mL solution was stirred at 60 rpm to mix the solution without disturbing the forsterite in the tube. After reacting for a certain period (1, 3, 5, 8, 15, 30 and 60 days), a sample of the bulk solution was collected and filtered through a 0.22 μm filter and acidified. The tube was taken out of the reactor. The water above the solid was removed and the solid sample was air-dried (21˚C, 15% relative humidity) in the tube until its weight became stable.

2.2.3 Analytical methods

Aqueous samples were analyzed by inductively coupled plasma mass spectroscopy (ICP-MS Agilent 7500ce) for dissolved Mg and Si concentrations. The intact solid sample in the glass tube was directly scanned with Raman spectroscopy using a HoloLab Series 5000 Laser Raman Microprobe (Kaiser Optical) with a 532 nm laser and a 20 power objective that probes a 5μm-diameter area. After Raman analysis, the sample was removed from the tube in 0.2-cm layers and analyzed for total carbon in a TOC analyzer at 900˚C with O_2 flow. The original and pretreated forsterite had total carbon (TC) contents of 1.67 ± 0.47 mg/g and 0.44 ± 0.02 mg/g, respectively, with no inorganic carbon (determined by IC module). Particle surface morphology was characterized by scanning electron microscopy (FEI Nova 230) of gold-coated samples (Figure S2.3).

2.3 Results and Discussion

2.3.1 Identification of carbonates

Carbonate minerals were identified by Raman spectroscopic analysis of the solids along the length of the packed bed. Figure 2.1 shows both short range and long range (270-1300 Δcm^{-1}) spectra for the solids after 3 days of reaction (Figure S2.4 has full spectra for other reaction times). Peaks at 824, 855, and 964 Δcm^{-1} that correspond to the stretching modes of the three types of Si-O bonds in forsterite[45] appeared in each sample. Magnesite and hydromagnesite are identified by the strong peaks at 1094 and 1119 cm^{-1}, respectively, that are associated with the CO_3^{2-} symmetric stretching mode.[46] This diagnostic region for carbonate minerals is shown in Figure 2.2 for all reaction times and depths with peak heights normalized to the highest forsterite peak (855 cm^{-1}) for semi-quantitative assessment of the carbonate content.

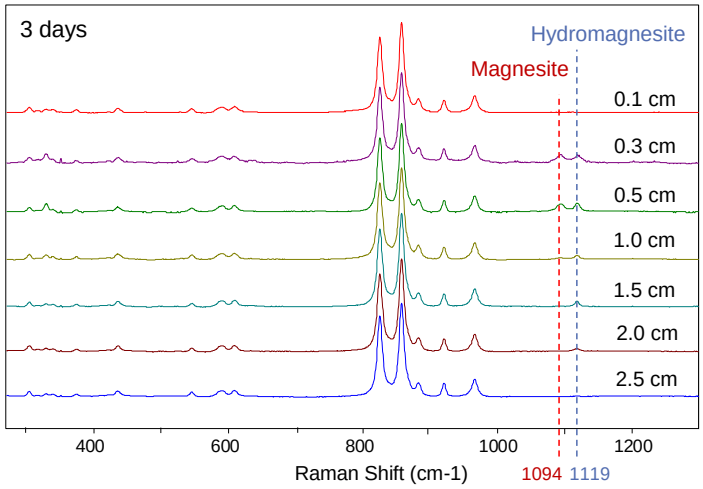

Figure 2.1 Raman spectra of solids from a tube packed with forsterite after 3 days of exposure of the tube to water at 100˚C in equilibrium with 100 bar CO_2. The major peaks at 824, 855, and 964Δcm^{-1} correspond to the stretching modes of the Si-O(2), Si-O(3) and Si-O(1) bonds in forsterite[45, 47]. The peaks at 1119 cm^{-1} and 1094 cm^{-1} correspond to the CO_3^{2-} symmetric stretching mode (ν_1) in hydromagnesite and magnesite, respectively.[46, 48]

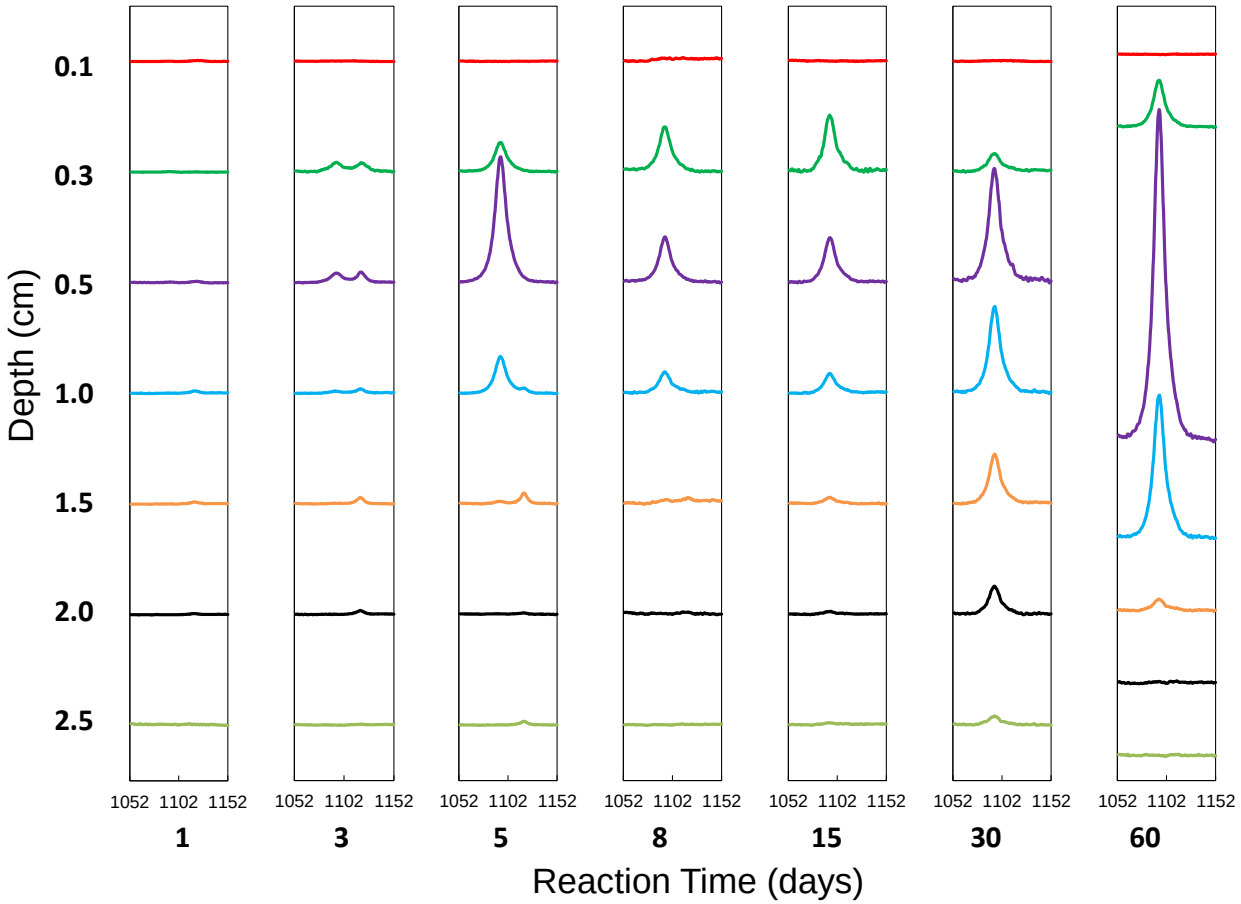

Figure 2.2 Combined Raman spectra for the range of carbonate peaks. The peaks are normalized to the highest forsterite peak at 855 cm^{-1} for semi-quantitative assessment of the carbonate content.

Carbonates were never observed in the top layer of the packed beds, which was due to the low pH environment provided by the bulk solution and the diffusion of Mg^{2+} out of the tube. After 1 day of reaction, hydromagnesite and some magnesite appeared at 0.5 cm. After 5 days magnesite became the dominant carbonate solid, and from 8 days on magnesite was the only carbonate present. Hydromagnesite was probably an intermediate solid because its formation is kinetically more favorable than that of magnesite. Hydromagnesite is not as thermodynamically

stable as magnesite, especially as the ratio of carbonate to hydroxide increases, and it transformed to magnesite over time. Previous work also observed hydromagnesite initially[49], and nesquehonite ($MgCO_3 \cdot 3H_2O$) and dypingite ($Mg_5(CO_3)_4(OH)_2 \cdot 5H_2O$) have appeared as intermediate species in the formation of magnesite ($MgCO_3$) under different conditions.[50, 51]

The Raman spectra show that magnesite precipitated at 0.3 cm and reached the highest amount at 0.5 cm. This spatial localization of precipitation is probably caused by opposing gradients in the concentrations of Mg^{2+} and CO_3^{2-} that generated the requisite extent of supersaturation at a specific location. The pH difference between the bulk solution and the packed bed creates a pH gradient in the tube. As forsterite dissolves, the consumption of H^+ increases the pH. The gradient in pH and the diffusion of Mg^{2+} out of the tube generate a gradient in the Mg^{2+} concentration with higher concentrations at greater depth. The diffusion of aqueous inorganic carbon into the tube leads to a gradient in its concentration with the highest concentration at the top of the tube. The concentration gradient of CO_3^{2-} is then set by the gradients of pH and dissolved inorganic carbon.

For forsterite-rich rocks the formation of carbonates may block the pore space and reduce surface area for reaction. On the other hand, the volume increase can exert stresses that may be relieved by cracking and additional expansion, creating new surface area for reaction.[18, 52, 53] A gap in the packed bed was observed at about 0.5 cm for the 5-day solid sample in both duplicate experiments (Figure S2.5), but these were not observed in the structure of the loosely packed bed for other reaction times. The formation of a gap is consistent with the volume increase associated with conversion of forsterite to magnesite.

2.3.2 Quantification of carbonates

Less than 3.3 mg/g of inorganic carbon (IC) was found in the top (0-0.2 cm) layer, followed by a sharp increase to a maximum in the 0.4-0.6 cm layer (Figure 2.3), which is consistent with the Raman spectroscopy results. Although Raman spectroscopy detected almost no carbonates at the bottom of the tube, total inorganic carbon was still appreciable, indicating successful penetration of carbonate into the deeper zones.

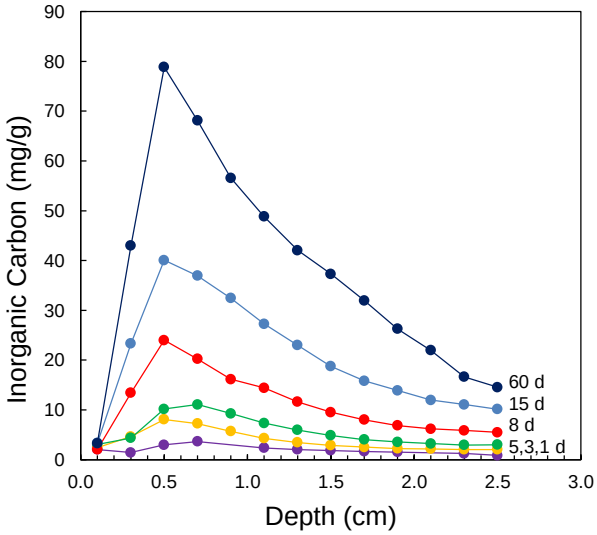

Figure 2.3 Profiles of inorganic carbon in the forsterite bed after exposure of the tube to CO_2-rich aqueous solution for reaction times up to 60 days. Each point represents the carbon content of a 0.2 cm-thick layer.

The overall extent of carbonation increased almost linearly until 30 days and subsequently declined (Figure 2.4), which may be due to increased resistance to diffusive solute transport. The overall carbonation extent was determined by adding the carbon masses in each layer. After 30 and 60 days of reaction, the solid sample could maintain its cylindrical shape (from 0.5 cm to the bottom) even without the glass tube, indicating that the powder was cemented through the precipitation of magnesite.

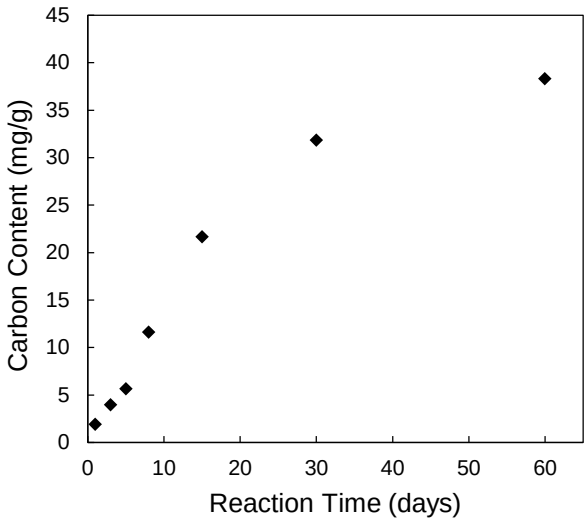

Figure 2.4 Total carbon in the tube after exposure of a bed packed with forsterite powder to a CO_2-rich solution at 100˚C in contact with 100 bar CO_2. The total carbon is determined from the depth profiles presented in Figure 2.3.

Because of the high solid-to-water ratio in the packed bed, the solution in the pores could attain the necessary supersaturated concentrations for magnesium carbonate precipitation. In the 100˚C 100 bar CO_2 open system, the pH of the bulk the solution outside of the tube is 3.2 (calculated by GWB, applying Duan's model for CO_2 solubility[54]), which could facilitate the dissolution of forsterite but would be too low for carbonates to precipitate. In an experiment in which the same amount of forsterite as in the tubular reactor experiments was reacted with complete mixing of the 200-mL suspension for 30 days (Figure S2.2b), the dissolved Mg concentrations in the bulk solution were higher (Figure S2.6), but no carbonate minerals precipitated (as determined by inorganic carbon measurement). Previous flow-through experiments also observed that magnesite formed only in diffusion-limited domains and not in advective flow paths.[49]

The opposing gradients in CO_3^{2-} and Mg^{2+} caused by diffusive transport limitations resulted in specific locations that reached the supersaturation needed to precipitate carbonates.[49] The location at 0.5 cm below the packed bed surface was so favorable for carbonate minerals to precipitate that the highest IC amount was observed. The formation of carbonates did not completely block the pores, and the supply of inorganic carbon to the deeper zones by diffusion was sufficient to result in continuous precipitation of magnesite with time; however, the consumption of inorganic carbon in the zone of maximum precipitation did result in lower amounts of carbonate mineral precipitation in deeper regions.

2.3.3 Environmental implications

Carbonation in diffusion-limited zones will have rates and products much different from those predicted using volume-averaged properties. In a well-mixed system, the pH is too low and the required supersaturation could not be achieved for carbonate precipitation. Although the experimental systems studied here were deliberately simple, the results are relevant to fractured rocks in which diffusion-limited dead-end fractures are open to bulk advective flow. Dead-end fractures could represent a substantial amount of a rock's reactive surface area. The one-dimensional packed bed experiments revealed that carbonate precipitation is spatially localized in diffusion-limited zones as a result of opposing geochemical gradients. The carbonation process did not shut itself down within the time of this study, but it did slow down after 30 days.

The texture of fractures in deep geological formations can be very different from the packed bed of forsterite particles. The packed bed can expand as carbonate minerals precipitate, but precipitation in fractured rocks could result in either complete filling of pores or the creation of new fractures from the pressure exerted by the volume expansion. Complete pore filling

would block diffusive transport paths in the fractures and shutdown the carbonation process. To better understand coupled reactive and transport effects in geologic carbon sequestration, experiments that study the spatial distribution of carbonates in intact rocks are needed.

Acknowledgements

We thank Jill Pasteris for assistance with Raman spectroscopy and Jeremy Moore for helpful discussions. This research was sponsored by the Consortium for Clean Coal Utilization at Washington University.

Supporting Information

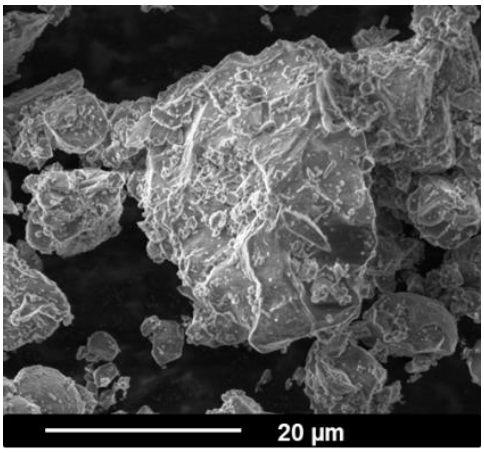

Figure S2.1 Scanning electron micrograph of pretreated forsterite powder showing the remaining attachment of fine particles to the surfaces of the larger particles.

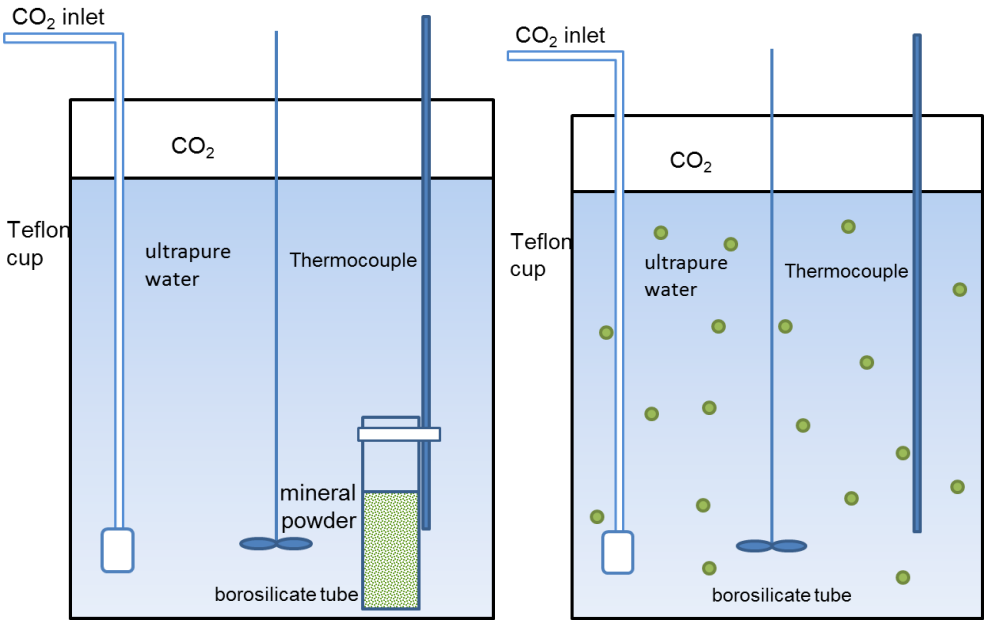

Figure S2.2 a) High pressure and temperature reactor with 200 mL of CO_2-rich solution into which a tube packed with forsterite powder is immersed. CO_2 is pumped into the reactor by a syringe pump. A constant CO_2 headspace pressure of 100 bar is then maintained by the pump. The reactor is heated to 100˚C using an external heating mantle. **b)** Well-mixed system setup. For the well-mixed system, instead of packing forsterite in the tube, the same amount of solid (3.97 g) was dispersed within the bulk solution at the same conditions. Aqueous samples were collected from the bulk solution after 1, 3, 5, 8, 15, and 30 days.

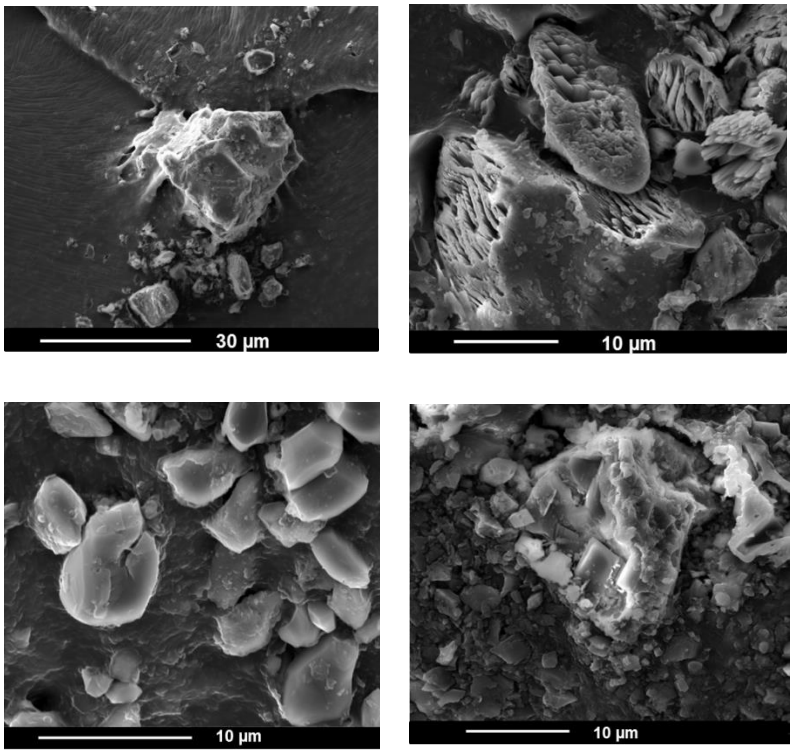

Figure S2.3 Scanning electron micrographs of solid samples from the tubular reactor after a) 8 days at 0-0.2 cm depth, b) 60 days at 0-0.2 cm depth c) 8 days at 0.4-0.6 cm depth, and d) 60 days at 0.4-0.6 cm depth. Most particles from 60 days of reaction were present as small and irregular particles like those surrounding the large particle in panel d. The shape and texture of the small particles were different with reaction time. For 8 days, the particle surface was relatively smooth, while there were sharp edges on the particle after 60 days of reaction.

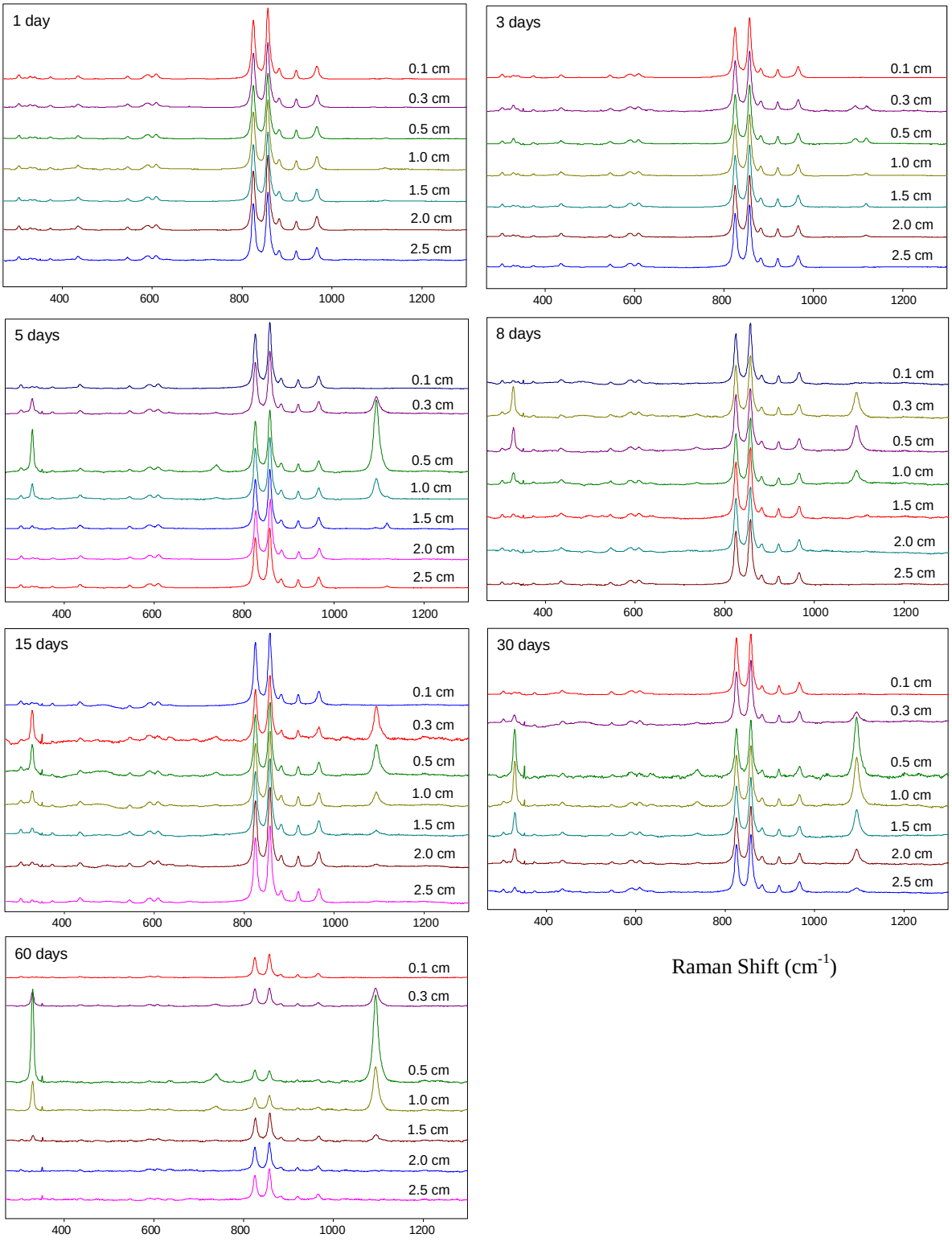

Figure S2.4 Raman spectra of samples for reaction times from 1 day to 60 days.

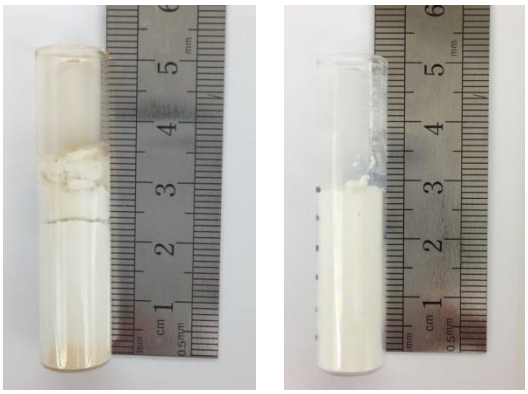

Figure S2.5 Packed bed of forsterite after 5 days of reaction for (a) the wet packed bed immediately after removal from the reactor and (b) the packed bed after manually applying pressure to close the gap that had developed at 0.5 cm and air-drying.

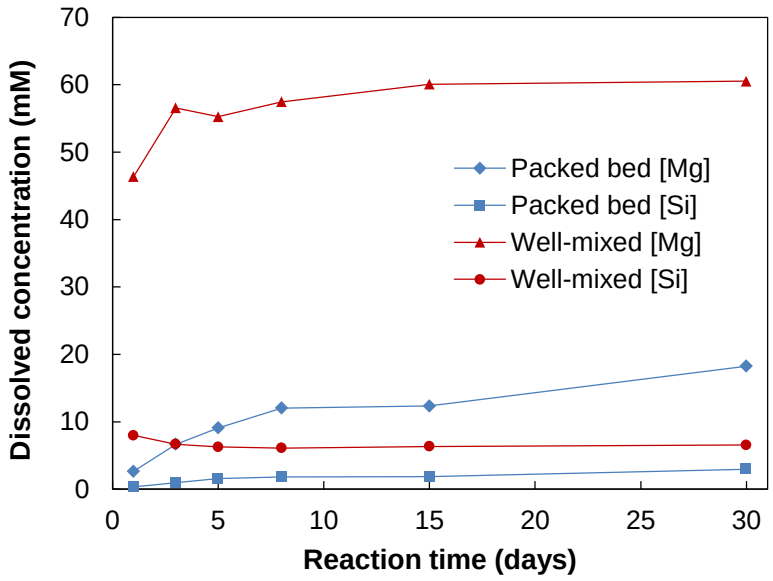

Figure S2.6 Dissolved Mg and Si concentrations in the bulk solution in packed bed system and in well-mixed system. The dissolution of forsterite in both systems was incongruent. The concentrations in the bulk solution from the packed bed system became stable after 30 days of reaction.

Chapter 3. Carbon Sequestration in Olivine and Basalt Powder Packed Beds

This chapter was published in Xiong, W.; Wells, R. K.; Giammar, D. E., Carbon Sequestration in Olivine and Basalt Powder Packed Beds. Environ Sci Technol 2017, 51, (4), 2105-2112.[55]

Abstract

Fractures and pores in basalt could provide substantial pore volume and surface area of reactive minerals for carbonate mineral formation in geologic carbon sequestration. In many fractures solute transport will be limited to diffusion, and opposing chemical gradients that form as a result of concentration differences can lead to spatial distribution of silicate mineral dissolution and carbonate mineral precipitation. Glass tubes packed with grains of olivine or basalt with different grain sizes and compositions were used to explore the identity and spatial distribution of carbonate minerals that form in dead-end one-dimensional diffusion-limited zones that are connected to a larger reservoir of water in equilibrium with 100 bar CO_2 at 100˚C. Magnesite formed in experiments with olivine, and Mg- and Ca-bearing siderite formed in experiments with flood basalt. The spatial distribution of carbonates varied between powder packed beds with different powder sizes. Packed beds of basalt powder with large specific surface areas sequestered more carbon per unit basalt mass than powder with low surface area. The spatial location and extent of carbonate mineral formation can influence the overall ability of fractured basalt to sequester carbon.

3.1 Introduction

Geological carbon sequestration (GCS) involves injecting CO_2 into deep geological formations for long term storage. Ultimately CO_2 can be converted into carbonate minerals, in a process known as mineral trapping that provides stable long-term sequestration.[3] Most subsurface carbon storage projects have injected CO_2 into sandstone basins, which can have good permeability and porosity for injection but minimal mineral trapping capacity resulting from the lack of reactive calcium-, magnesium-, and iron-silicate minerals required to neutralize the acidity of the injected CO_2 and release the divalent cations needed for carbonate mineral precipitation.[3, 20, 29] Basalt is a common mafic rock that contains minerals rich in these divalent cations, making it a good candidate for CO_2 mineral sequestration.[15, 56]

Research has shown great potential for geological carbon sequestration in basalts.[15, 57] Recent pilot-scale CO_2 injections have taken place in southwest Iceland by the CarbFix project and in the northwest United States near Wallula, Washington by the Big Sky Carbon Sequestration Partnership.[20] Olivine, $(Mg_xFe_{1-x})_2SiO_4$, has the fastest dissolution kinetics and highest carbonate-forming potential among minerals found in basalt.[58] Many laboratory studies have been conducted regarding the dissolution and carbonation of olivine and olivine-rich rocks in conditions relevant to geologic carbon sequestration. Most experiments were done with well-mixed systems in which the olivine or basalt powders have maximum accessibility to dissolved CO_2 in the solution, which provides a good means of quantifying reaction rates and identifying reaction products.[23, 34, 35, 38] Batch experiments with high solid-to-water ratio showed rapid mineralization of basalt powders.[59] Interfacial reactions such as dissolution and precipitation are still the rate-limiting factors since diffusion is not strongly inhibited in boundary films that attach to the surface of mineral and rock grains.[60-62] However, reactions in basalt reservoirs may

primarily occur in poorly mixed fractures and pores. Diffusion-limited zones can achieve extents of supersaturation with respect to potential carbonate precipitates much higher than in the bulk solution. Our previous studies of the coupling of dissolution-precipitation reactions and diffusive transport in beds packed with forsterite (Mg_2SiO_4) powder found that carbonate mineral precipitation was spatially localized within the beds as a result of geochemical gradients in pH, dissolved inorganic carbon, and dissolved magnesium.[27, 63]

The present study builds on these earlier packed bed experiments by examining reactions with basalts and not just single mineral systems and by systematically exploring the effects of particle size and composition on carbonate mineral formation. The objectives of the study were to determine the influence of mafic rock and mineral composition and particle size on the location and extent of carbonate mineral formation upon reaction with CO_2-rich aqueous solutions in zones with transport limited to diffusion. A set of laboratory experiments with basalts and olivine in different composition and grain sizes were conducted in bench-scale systems equilibrated with 100 bar CO_2 at 100˚C. After different reaction times the identities, amounts, and locations of carbonate minerals were determined using Raman spectroscopy, electron microscopy, and total carbon analysis.

3.2 Materials and Methods

3.2.1 Materials

Forsteritic olivine fine powder (Fo_{99}, 99% Mg_2SiO_4) was purchased from Alfa Aesar. San Carlos olivine grains (Fo_{90}, $Mg_{1.8}Fe_{0.2}SiO_4$), Columbia River flood basalt (Pullman, Washington), and serpentinized basalt (Valmont Butte, Colorado) rocks were purchased from Ward's Science.

Basaltic glass from the Stapafell Mountains was provided by Sigurdur Gislason's research group in Iceland. The compositions of the flood basalt and the serpentinized basalt are listed in Table 3.1, and additional rock and mineral characterization information are available.[64] The basaltic glass is homogeneous compared to the other two basalts and has a chemical formula consistent with $SiTi_{0.02}Al_{0.36}Fe(III)_{0.02}Fe(II)_{0.17}Mg_{0.28}Ca_{0.26}Na_{0.08}K_{0.008}O_{3.45}$ (normalized to one Si).[26, 65] The forsterite powder was sieved to yield particles smaller than 53 µm. Olivine was ground and sieved to fractions of <53 µm and 53-106 µm. The olivine powder was sonicated in acetone and rinsed in water to remove organic contaminants and fine particles on the surface. Part of the <53 µm olivine powder was further pulverized in a ball mill (FRITSCH pulverisette) to increase its specific surface area and match that of the <53 µm forsterite (Table 3.2). Basalt rocks were ground and sieved to generate the 53-106 µm size fraction and then cleaned in the same procedure as olivine powders. Although the basalt rocks went through the same grinding and sieving processes, the flood basalt has a much larger BET surface area than the serpentinized basalt and the basaltic glass. The reactive surface area was very small for the basaltic glass powder due to the nature of glass, which tends to form smooth, conchoidal fracture surfaces (Figure S3.1a, S3.1d, S3.1g).

Table 3.1 Composition of flood basalt (FB) and serpentinized basalt (SB) with percentages (by mass) of constituent minerals[64]

Composition	FB		SB	
Ca-pyroxene	22%	$Ca_{0.63}Fe_{0.48}Mg_{0.83}Ti_{0.03}Al_{0.09}Si_{1.92}O_6$	21%	$Ca_{0.83}Fe_{0.25}Mg_{0.85}Ti_{0.03}Al_{0.07}Si_{1.96}O_6$
Olivine	9%	$Mg_{1.21}Fe_{0.78}Ca_{0.01}SiO_4$	1%	$Mg_{1.38}Fe_{0.59}Mn_{0.02}Si_{1.01}O_4$
Serpentine	1%		14%	$Na_{0.01}Mg_{0.6}Al_{0.27}K_{0.01}Ca_{0.11}Mn_{0.05}Fe_{1.82}Si_3O_9H_x$
K-rich matrix*	33%	$Ca_{0.04}Na_{0.33}K_{0.64}Fe_{0.01}Al_{1.06}Si_{2.93}O_8$	32%	$Ca_{0.03}Na_{0.32}K_{0.66}Fe_{0.05}Al_{1.05}Si_{2.94}O_8$
Orthopyroxene	1%		1%	
Plagioclase	31%	$Ca_{0.59}Na_{0.40}Fe_{0.03}Al_{1.57}Si_{2.40}O_8$	28%	$Ca_{0.55}Na_{0.43}Fe_{0.02}Al_{1.57}Si_{2.43}O_8$

* The K-rich matrix is composed of submicron fine grains within a glass matrix and not a single phase mineral although the WDS data can be normalized to fit a feldspar composition.

Table 3.2 Size and surface areas of materials used in packed bed experiments

No.	Mineral and rock	Sieving size (μm)	BET surface area (m^2/g)
1	Forsterite (Fo_{99})	<53	3.7
2	Olivine (Fo_{90})	<53	3.7
3	Olivine (Fo_{90})	53-106	0.2
4	Flood basalt	53-106	6.4
5	Serpentinized basalt	53-106	0.9
6	Basaltic glass	53-106	0.2

3.2.2 Packed bed experiments

Experiments were conducted with glass tubes that were packed with powders as in previous research.[27] The powders were wet-packed to depths of 3 cm in the borosilicate tubes (1 cm diameter and 5 cm length). After packing, the tube with the wet packed bed was weighed and powder mass was calculated. The olivine powder in the tube was around 4 g with 1.1 g of DI water. The basalt powder is around 3.6 g with 1.3 g of DI water. Packed bed porosities were 0.48-0.50 based on the powder mass and density and the measured bed volume. The tubes were fixed vertically inside a high-pressure and –temperature reactor with a PTFE liner (Parr Instrument). The reactor was loaded with 200 mL ultrapure water, which was sufficient to fully immerse the tube when the reactor was sealed and to leave approximately 50 mL of headspace. A syringe pump (500D, Teledyne Isco) provided a constant CO_2 pressure (100 bar) to the

headspace. The reactor was heated to 100˚C. The pump stopped adding CO_2 to the reactor within 1 hour, indicating that equilibrium between CO_2 and water had been reached. The olivine and the basalt powder packed beds reacted for 15 and 28 days, respectively. The reactors were not stirred so as to minimize any loss of powder from the tube. After reaction, the reactors were cooled and depressurized before samples were removed from the vessel. A liquid sample was collected from the bulk solution and filtered through a 0.22 μm filter and acidified for analysis. The tube with the intact reacted powder packed bed was removed and dried in a desiccator until its weight became stable.

3.2.3 Analytical methods

The specific surface areas of unreacted materials were measured by a BET−N_2 adsorption analyzer (Quantachrome Instruments, NOVA 2000e). Aqueous samples were analyzed by inductively coupled plasma mass spectrometry (Perkin Elmer, Elan DRC II). For olivine packed beds, the intact solid sample in the glass tube was air-dried for at least a week and directly scanned through the glass via Raman spectroscopy (HoloLab Series 5000 Laser Raman Microprobe, Kaiser Optical) with a 532 nm laser and a 20 power objective that probes a 5 μm area. Raman spectroscopy can identify carbonate minerals based on the appearance and location of peaks associated with CO_3^{2-} vibrations. Reacted powders from basalt packed beds were examined by Raman spectroscopy instead of the intact packed bed due to the fluorescence background in large amount of reacted basalt powders. The reacted olivine powders were taken out and examined by scanning electron microscopy (FEI Nova 230) with energy-dispersive X-ray spectroscopy (EDX) after gold-coating. The reacted basalt powders were imaged with a scanning electron microscope (SEM) (JEOL 7001LVF FE-SEM) after carbon-coating, and

elemental analysis was collected using energy dispersive spectroscopy (EDX) analysis. X-ray diffraction (Bruker d8 Advance) and electron probe microanalysis (JEOL JXA-8200) with wavelength-dispersive spectrometry (WDS) were used to identify secondary precipitates in the flood basalt packed bed. The powder samples were scooped layer by layer from the tube in 0.2-cm layers for the olivine packed beds and 0.3-cm layers for the basalt packed beds due to technical difficulty to determine the layer border in the loose basalt powder packed beds. Each layer of powder was analyzed for total carbon in a carbon analyzer operated at 900˚C with an O_2 flow. Total inorganic carbon (i.e., the carbon from carbonate minerals) was calculated via subtracting the total carbon amount of the sample by the total carbon background of the unreacted powder. The total inorganic carbon amounts were 0.84 mg/g, 1.00 mg/g and 0.44 mg/g in unreacted 53-106 μm Fo_{90}, <53 μm Fo_{90} and <53 μm Fo_{99}, respectively. The amounts were 0.00 mg/g, 0.01 mg/g and 0.03 mg/g in unreacted flood basalt, serpentinized basalt, and basaltic glass.

3.2.4 Reaction path modeling

We performed reaction path modeling in Geochemists' Workbench 8.0 (GWB) to examine how the minerals present in the same amount as in the flood basalt would react in 200 mL and 1.3 mL water (see the model in SI). The minerals in the flood basalt were assigned to different end-members that are documented in the GWB default database to give the same amount of cations. Temperature was set at 100˚C. Dissolved aqueous CO_2 was calculated[54] and fixed in the model as an open system. The minerals are assumed to dissolve congruently at the same rate. The model represented an ideal mixed system for two bounding conditions of the actual system. The first was with the solid to water ratio of 3.6 g per 200 mL as in the bulk

solution (i.e., if the basalt was suspended in the full 200 mL volume and was not isolated in the packed bed). The second was with 3.6 g per 1.3 mL as in the wet packed bed (i.e., if there was no exchange between the water in the packed bed and the bulk solution).

3.3 Results and Discussion

3.3.1 Olivine packed beds

Raman spectroscopy of materials in the three olivine packed beds had a peak at 1094 cm^{-1}, which corresponds to the CO_3^{2-} symmetric stretching mode (ν_1) in magnesite[46, 58] (Figure 3.1). The peaks at 824, 855, and 964 cm^{-1} correspond to the stretching modes of the three types of Si−O bonds in olivine[45]. Magnesite was the only carbonate mineral formed in all three olivine packed beds. Carbonate minerals were rare in the layer that was closest to the CO_2-saturated bulk solution (0~0.2 cm); the bulk solution had an initial pH down to 3.2 (calculated based on charge balance and predicted CO_2 solubility[54]) that facilitated olivine dissolution but kept the solution far from saturation with respect to carbonate minerals. Peak heights in Raman spectroscopy give a semi-quantitative assessment of the amount of material (e.g., magnesite) present. The trend of the peak height shows that in the <53 μm Fo_{90} and Fo_{99} beds, carbonate minerals were most abundant in the 0.4-0.6 cm layer and gradually decreased in abundance down into the bed. In the 53-106 μm Fo_{90} bed, the carbonate peaks were much shorter than in the <53 μm Fo_{90} and Fo_{99} beds, indicating less carbonate mineral formation in the packed beds with larger grain size and smaller surface area, regardless of composition. The dissolved inorganic carbon diffuses into the packed bed, while the cations released from the olivine are diffusing out. Magnesite forms when the critical saturation ratio in the pore water is reached, which requires the accumulation of

released cations and dissolved inorganic carbon as well as a sufficiently high pH. The opposing chemical gradients in concentrations of cations and dissolved inorganic carbon may result in the spatial localization of carbonate mineral formation; such localization was experimentally observed in our earlier work and was also supported by reactive transport simulations that predicted a zone of greatest solution saturation with respect to magnesite.[63] A thin orange layer (1~2 mm thick) also occurred on the top of the two Fo_{90} packed beds (Figure S3.2). This is due to the oxidation of Fe^{2+} released from Fo_{90} dissolution by residual O_2 in the solution. This orange layer did not occur in the packed bed with the Fo_{99} powder because that material had almost no iron.

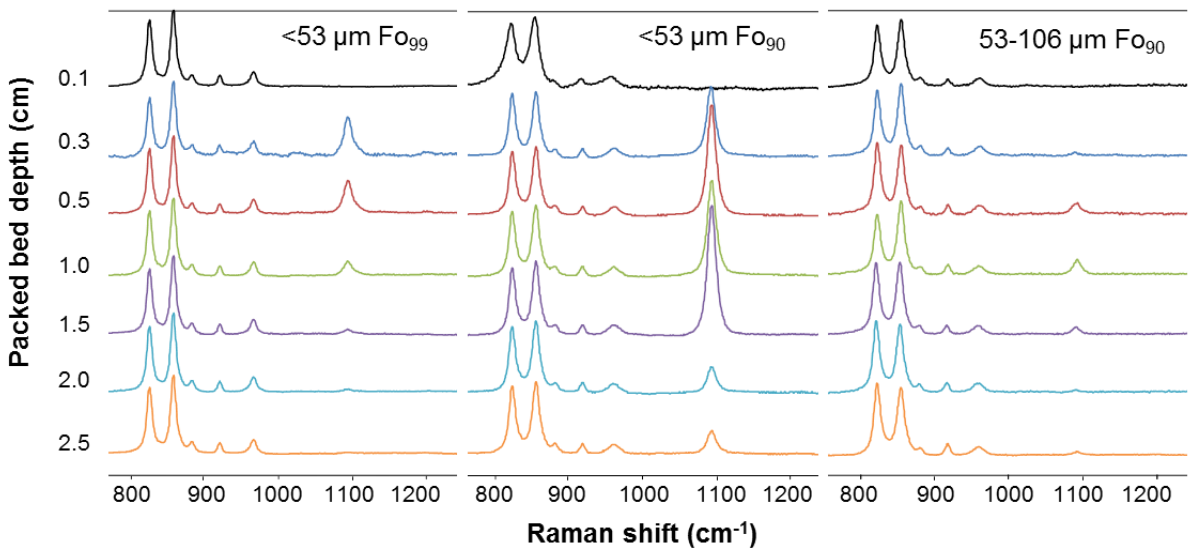

Figure 3.1 Raman spectroscopy on olivine powder packed beds reacted for 15 days in water in equilibrium with 100 bar CO_2 and at 100˚C. The peaks at 1094 cm^{-1} represent magnesite. The patterns are normalized to the similar height of olivine peaks in the range of 800-1000 cm^{-1}.

The total carbon analysis quantitatively confirmed the spatial distribution of magnesite in the <53 μm Fo_{90} and Fo_{99} beds that had been observed using Raman spectroscopy (Figure 3.2a).

Very limited inorganic carbon was observed in the top layer that was closest to the bulk solution. The inorganic carbon amount increased to the highest amount (50 mg/g and 40 mg/g for <53 μm Fo_{90} and <53 μm Fo_{99}, respectively) in the 0.4-0.6 cm layer and gradually decreased along the bed to the bottom. For the 53-106 μm Fo_{90} bed, the trend of carbonate distribution was relatively smooth. The top 0~0.2 cm layer had little carbonate as well. The highest amount of inorganic carbon (10 mg/g) appeared in the 0.2-0.4 cm layer. The total carbon amount gradually decreased from 10 mg/g to 7 mg/g along the tube below the second layer (0.2-0.4 cm). More magnesite formed in the <53 μm Fo_{90} packed bed than in the <53 μm Fo_{99} packed bed even though they have the same initial specific surface area. Iron-containing olivine dissolves faster than pure forsterite.[66] A greater abundance of magnesite in the Fo_{90} packed bed is probably due to a greater release of Mg and Fe into solution. The lower abundance of magnesite within the Fo_{99} packed bed is probably the result of slower dissolution compared to that of iron-bearing olivine. The total inorganic carbon sequestered in the entire 53-106 μm Fo_{90} bed (8 mg/g) was much less than in the <53 μm Fo_{90} bed (30 mg/g) and <53 μm Fo_{99} bed (22 mg/g). Larger surface areas from the smaller particles facilitated greater olivine dissolution and made more Mg and Fe available for carbonate precipitation. The inorganic carbon amounts in the packed beds were normalized to the initial surface areas of the powders to yield values of 42 mg/m^2, 8 mg/m^2, and 6 mg/m^2 for the 53-106 μm Fo_{90}, <53 μm Fo_{90} and <53 μm Fo_{99} packed beds, respectively. The comparison of the amounts from the <53 μm Fo_{90} and <53 μm Fo_{99} confirm the greater reactivity of the Fo_{90}, and the comparison of the two size fractions for the Fo_{90} indicates that surface area is not the only factor controlling the amount of carbonate mineral formation; the larger particle size sequestered less total carbon, but it actually sequestered more carbon per unit surface area. A

portion of surface area in the <53 µm powder packed bed may not have been accessible for reaction.

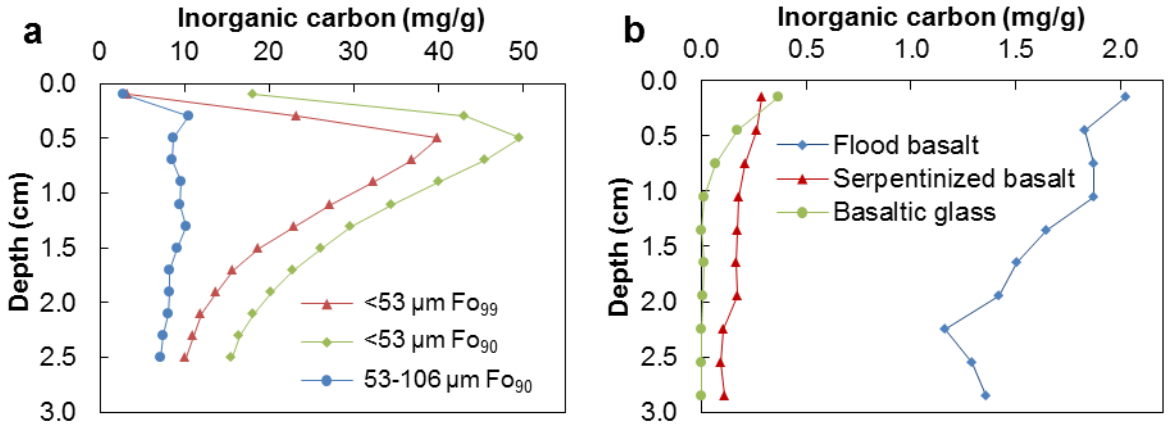

Figure 3.2 Total inorganic carbon accumulated in the powder packed beds of a) olivine and b) basalt.

Euhedral magnesite crystals are observed within the packed powder beds. The magnesite in the Fo_{99} packed bed was pure $MgCO_3$, while the magnesite in the Fo_{90} packed beds contained trace amounts of Fe. Scattered amorphous silica was found on the surfaces of both magnesite and olivine. Magnesite was found on the surface of the 53-106 µm Fo_{90} particles (Figure 3.3a), indicating heterogeneous growth of the carbonate on the silicate mineral. The magnesite size was approximately 20 µm, which was larger than the magnesite that formed in the <53 µm Fo_{90} packed beds with sizes around 5 µm (Figure 3.3b). Considering the total carbon analysis and the sizes of the magnesite particles, the number of magnesite particles in the <53 µm packed bed should be much greater than in the 53-106 µm packed bed.

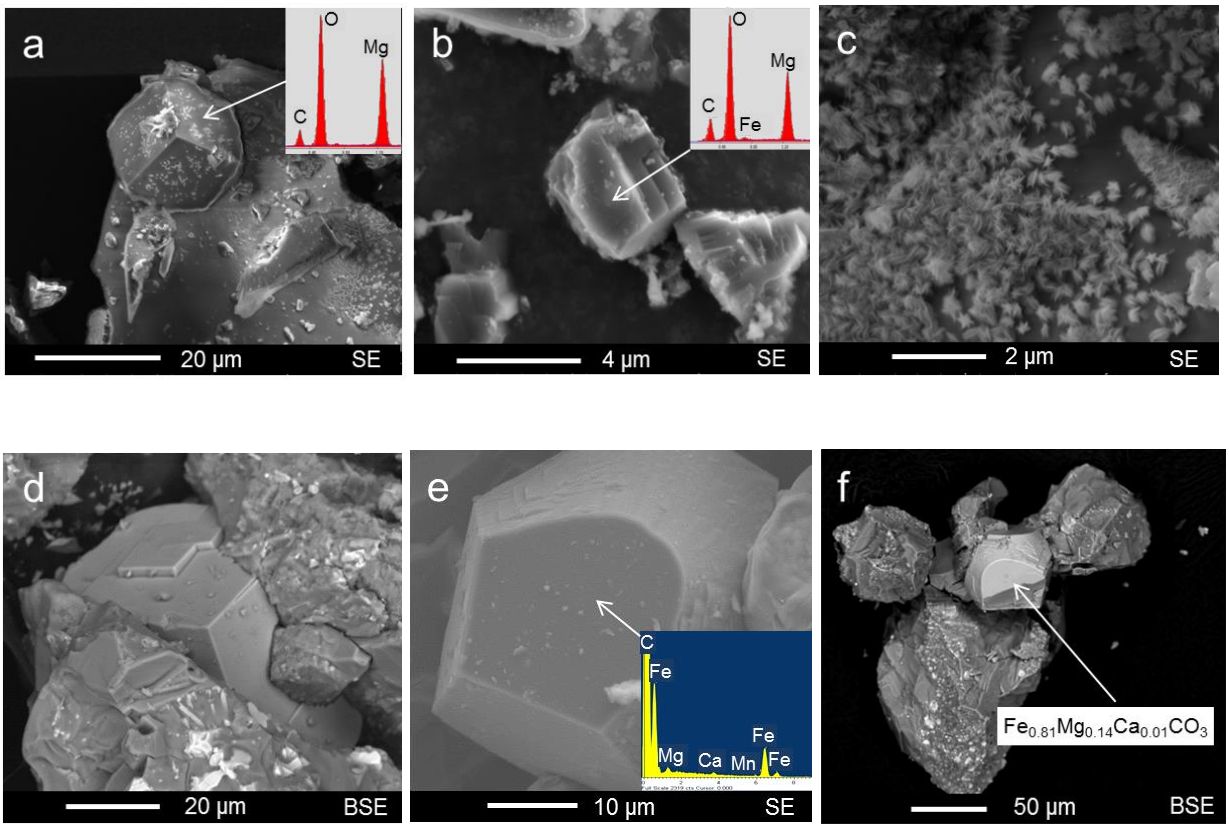

Figure 3.3 SEM SE/BSE images of a) magnesite precipitated on the olivine surface in the 0.8-1.0 cm layer of the 53-106 µm Fo_{90} packed bed, with amorphous silica on the surface, b) magnesite on the tape from the 0.8-1.0 cm layer of the <53 µm Fo_{90} packed bed, c) lizardite formation on the reacted flood basalt from 0-0.3 cm layer, d) rhombohedral siderite in between flood basalt powder from the 0-0.3 cm layer, e) pentagon shape siderite on flood basalt from the 0-0.3 cm layer, with amorphous silica on the surface, f) siderite with the composition by WDS analysis

3.3.2 Basalt packed beds

Multiple secondary precipitates were formed in the basalt powder packed beds during the reaction. Euhedral carbonate minerals, ranging in size from 10 µm to 50 µm, were observed on

the surface of the flood basalt powder (Figure 3.3d-f). WDS analysis showed that the precipitate had a composition of $Fe_{0.81}Mg_{0.14}Ca_{0.01}CO_3$, which is Mg- and Ca-containing siderite (Figure 3.3f, Table S3.1). Raman spectroscopy (Figure 3.4) determined that the carbonate mineral was siderite by comparison with carbonate mineral standards from the RRUFF online database (standard details in SI). The evolution of Raman peaks is a function of Fe content in $FeCO_3$-$MgCO_3$ solid solutions, thus Raman spectroscopy can determine the Fe amount.[67] Comparing the peaks at 285, 719 and 1085 cm^{-1} with the spectra provided in a previous study[67] suggests that the Fe content in the siderite could be 80~100 %, which is consistent with the WDS analysis. SEM-EDX showed that the precipitate was a Fe-rich carbonate mineral with small amounts of Ca and Mg (Figure 3.3e, S3.3). XRD also confirmed that siderite and montesommaite (a K-rich zeolite) formed in the flood basalt after reaction (Figure S3.4). The observed siderite morphology including pentagon, rhombohedra, pyramid and column (Figure S3.1b-c) was also reported in a previous study about reactions of fayalite (Fe_2SiO_4) with CO_2-rich water.[68] Lizardite, $Mg_3Si_2O_5(OH)_4$, (Figure 3.3c), a serpentine from alteration of Mg silicates, was identified on the surface of the reacted flood basalt powder by its distinct six-pointed star shape.[69] Individual lizardite crystals were very small, with the size ranging from 100 nm to 200 nm, but they formed massively and covered part of the surface of some individual flood basalt grains. It was common to find trace amounts of amorphous silica precipitated on both the basalt surface and carbonate mineral surface. The surfaces of the serpentinized basalt and basaltic glass were a little rougher post-reaction than the starting unreacted surfaces (Figure S3.1d-i). No observable secondary precipitates were found on the reacted serpentinized basalt and basaltic glass samples tested in the SEM.

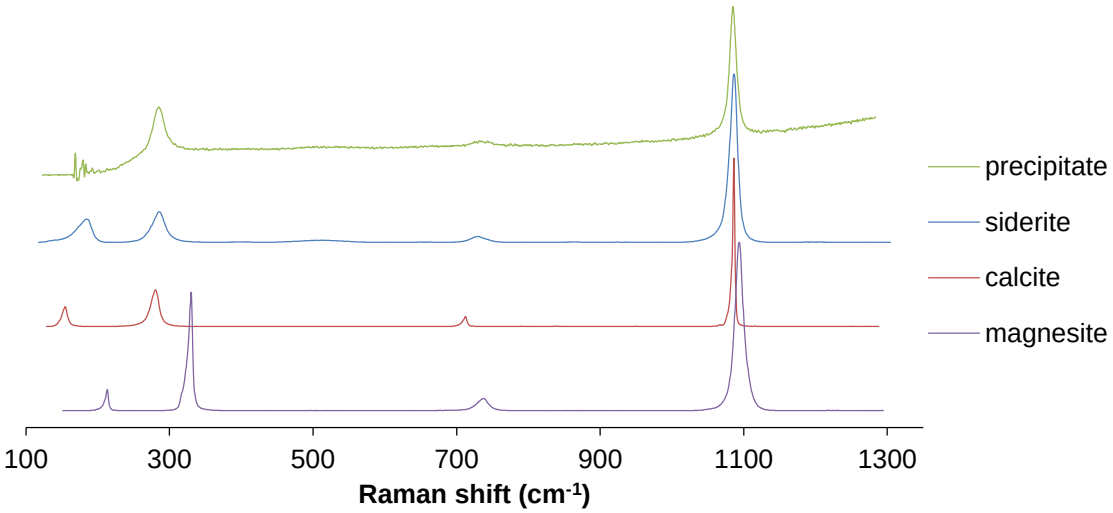

Figure 3.4 Raman spectra of the pentagonal carbonate mineral in Figure 3.3e and carbonate standards of siderite, calcite and magnesite (standards details in SI). Spectrum intensity is normalized to the maximum point. The pentagonal precipitate was identified as siderite.

The total amount of inorganic carbon sequestered in basalt packed beds was 1-2 orders of magnitude lower than that in olivine packed beds (Figure 3.2b). The low inorganic carbon amount in the packed beds of serpentinized basalt and basaltic glass indicated very limited formation of carbonate minerals, which is consistent with the lack of any observed secondary minerals in SEM imaging. The average inorganic carbon amount in the entire packed beds was 1.6 mg/g, 0.5 mg/g and 0.05 mg/g for flood basalt, serpentinized basalt, and basaltic glass, respectively. The calculated inorganic carbon amount per BET surface area (6.4 m^2/g, 0.9 m^2/g, 0.2 m^2/g) in the entire packed beds was 0.3 mg /m^2, 0.6 mg/m^2 and 0.3 mg/m^2 for flood basalt, serpentinized basalt, and basaltic glass, respectively. With the same size range, more reactive surface area resulted in more carbon sequestered by basalt powder. Unlike in the olivine powder packed beds where the location of maximum carbonate mineral formation occurred at layers lower than the top layer, the highest carbon amount occurred in the top 0-0.3 cm layer within the

basalt packed beds. This could be due to a thicker layer (0.3 cm instead of 0.2 cm) in basalt packed beds that lowered the analysis resolution.

The concentrations of elements that were transported out of the packed beds and into the bulk solution provide information about dissolution and precipitation that occurred inside the beds (Figure 3.5). Mass balance calculations can provide a rough estimate of the major minerals in the packed beds of basalt that dissolved. Assuming that the minerals in basalt dissolve congruently, we prepared mass balance equations (see supporting information) for Mg, Ca, Al (and Mn) that relate the dissolved concentrations to the amounts of specific minerals that would have dissolved. We did not apply this approach to the mass balance of Fe, because portions of the Fe released from silicate minerals precipitated in the beds as siderite and iron oxides, indicated by the limited amount of dissolved Fe present in the bulk solution (Figure 3.5). The plagioclase and the K-rich matrix will provide negligible amounts of divalent cations so we neglected these two components in the calculation. The dissolved Ca was primarily from pyroxene in both basalts. The pyroxene is Ca-rich and would fall within the diopside field.[64] Since olivine dissolution is about two orders of magnitude faster than serpentine at 90˚C in acidic solution[70] and there was 9% olivine in the flood basalt, the 1% of serpentine was not considered in the mass balance calculations for the flood basalt. For the serpentinized basalt, the serpentine is more abundant (14%) and cannot be neglected. For experiments with flood basalt, pyroxene, and olivine were calculated to be the two minerals that released the vast majority of Mg and Fe from the primary silicate minerals. While in experiments with serpentinized basalt, pyroxene, and serpentine are the major minerals that released the most Mg and Fe. For both basalts, much of the iron did not reach the bulk solution and would have been retained in secondary phases.

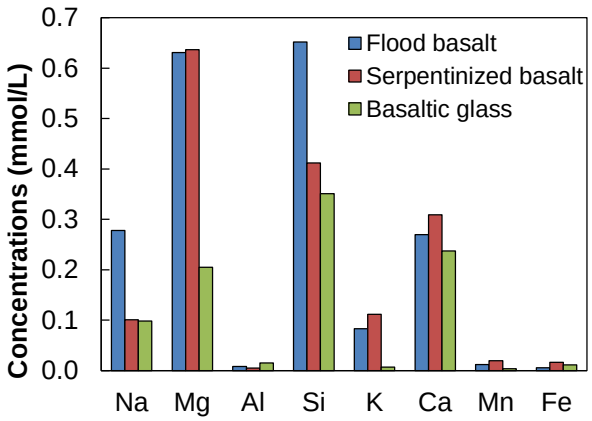

Figure 3.5 Dissolved element concentrations in the 200 mL bulk solution of the batch reactors from experiments with basalt packed beds after 4 weeks at 100˚C and 100 bar CO_2

3.3.3 Siderite formation

Carbonate mineral formation within the basalt packed powder bed was enabled by a locally high pH and supersaturated environment. Previous numerical and experimental studies of basaltic glass also demonstrated that secondary mineral formation depends on reaction progress and pH.[71, 72] In the present reaction path modeling, the pH increases from 3.2 to 5.0 (in 200 mL water) or to 5.7 (in 1.3 mL water) at the end of the reaction process (Figure S3.5a). This range is consistent with a previous modelling study that suggested that at 100 bar CO_2, the pH initially drops to ~ 3.5, and the basalt-CO_2-H_2O interactions can only bring the pH back to ~5.8.[70] For the model with basalt reaction in 200 mL of water, siderite forms first when the pH is approximately 4.2 and magnesite and calcite are predicted to form later when the pH is higher than 4.9 (Figure S3.5a). For modeling the reaction in 1.3 mL water, the three carbonate minerals appear almost simultaneously at the beginning of the reaction (Figure S3.6a), with siderite forming slightly earlier than magnesite and calcite as the pH reaches 4.7 (Figure S3.6b). Comparing the sodium concentration in the aqueous solution of the model (Figure S3.5b) with the measured

concentration of 0.3 mM at the end of the experiment (Figure 3.5), the reaction progress after the experimental duration is estimated to be about 0.02, indicating that the experimental reaction was still in the very early stage of the overall reaction progress. This reaction progress is only a rough estimate because it is based on the assumption of all minerals in the flood basalt dissolving at the same rates, when in fact the olivine and pyroxenes that will release Fe, Mg, and Ca are likely to be dissolving faster than the feldspar that would be releasing Na.

Siderite is expected to be the first carbonate mineral to form in this study. The solubility products (K_{sp}) of calcite, magnesite and siderite, the common carbonate products during GCS reactions, are $10^{-9.22}$, $10^{-9.41}$, $10^{-11.45}$ at 100˚C (calculated from SUPCRT 92). With the same amount of dissolved CO_2 in the system, the concentration of Fe^{2+} required to reach supersaturation for siderite is two orders of magnitude lower than the concentrations of Mg^{2+} or Ca^{2+} to reach supersaturation for magnesite or calcite. However, siderite has much slower precipitation kinetics than calcite. [73, 74] Our study showed rapid siderite precipitation within 4 weeks. Another experimental study on basaltic glass also demonstrated that Fe-rich carbonates were initially saturated or supersaturated but with increasing reaction time, the Fe-rich carbonate became undersaturated whereas calcite, dolomite and magnesite became saturated at pH > 6.5,[25] which is not the case in this study. In the present study, based on measured dissolved ions in the bulk solution (Figure 3.5), the saturation indices of siderite, magnesite and calcite in 100˚C 100 bar CO_2 were calculated (Figure S3.7). All of the carbonate minerals were undersaturated in the bulk solution during reaction, with siderite closest to achieving saturation. The undersaturation in the bulk solution and the observation of siderite in the packed bed indicate that siderite formed first among carbonate minerals and can only form in diffusive-transport controlled powder packed beds instead of the bulk solution. The packed bed experiments also indicate that in basalt

reservoirs carbonate minerals are likely to form only in fractures and pores where transport is diffusion-controlled so that the ions can accumulate and reach the saturation extents necessary for precipitation.

The carbonate products can vary according to different basalt and reaction conditions. A study of mid-ocean ridge basalt (MORB) powder carbonation at 150˚C and 280 bar CO_2 provided evidence that iron-bearing magnesite formed following olivine dissolution.[23] The MORB contains 12 wt % of olivine (Fo_{85}), which contains less iron than the olivine (Fo_{61}) in the flood basalt in this study. As discussed previously, olivine dissolution is faster for more iron-rich materials and siderite is easier to form than magnesite, so it is not surprising that the MORB carbonation product was magnesite and in the present study the product was siderite. In the Iceland CarbFix CO_2 injection project into basalt, which has a temperature and pH of 20-30˚C and 8.4-9.4, the carbonate precipitate is calcite.[19] Monitoring fluids from the CarbFix site indicate saturation or supersaturation with respect to calcite following CO_2 injection.[19] The alkalinity of the formation waters and the dissolution of preexisting carbonate minerals may also contribute to the neutralization of the injected CO_2-rich water to bring up the pH.[19] In the carbon sequestration project led by the BigSky Partnership, ankerite $Ca(Fe,Mg,Mn)(CO_3)_2$ nodules were found to form in vesicles of the Grand Ronde basalt.[22] Experimental study on basalt glass showed that at < 100˚C, the main carbonation products are Ca-Mg-Fe carbonates and at >150˚C, calcite became the dominant carbonate products instead.[26]

3.3.4 Environmental implications

For carbon sequestration in basalt, carbonate mineral formation would occur in diffusion-limited zones such as fractures and pores rather than in well-mixed zones like those of the bulk

solution in our experiments. The powder packed beds can be related to dead-end fractures and vesicles in natural basalt, but with larger surface area. Carbonate mineral formation can be spatially distributed along and within a zone with transport limited to diffusion. High solid-water ratio in diffusion limited zones leads to accumulation of dissolved cations and gradients in their concentrations between the diffusion-limited region and the well-mixed outer solution. Opposing gradients of dissolved cations and dissolved inorganic carbon enable the solution to reach the critical saturation ratio for precipitation at certain locations. Rock and mineral composition can be an important factor regarding the carbonation capacity. Iron-containing olivine sequestered more carbon than the magnesium-endmember forsterite. The accessible reactive surface area also plays a crucial role in dissolution and carbonation reactions. Rougher fracture surface with large accessible reactive surface areas may end up with larger amounts of carbon mineral trapping.

Basalt carbonation is sufficiently rapid that siderite formed after only 4 weeks of reaction in this study, indicating that rapid mineral trapping is possible in basalt reservoirs. This is very fast when compared with the time-scales for mineral trapping in sandstones, which may take hundreds to thousands of years[3]. Documenting basalt formations with numerous fractures and pores that provide a large reactive surface area will be an important aspect when selecting reservoirs for GCS. The permeability-porosity relationship is different in the powder packed beds and the fractured basalt due to the fundamental difference in pore structure and connection[75], which may influence the distribution of reaction products in basalt rock. Future studies with fractured basalt cores are necessary to investigate the effect of carbonation reactions on transport in microfractures and pores inside bulk rocks.

Acknowledgements

We thank Professor Jill Pasteris for helping with the Raman spectroscopy. We thank Professor Sigurdur Gislason for providing the basaltic glass from Iceland. We appreciate the insights of three reviewers who provided valuable comments to improve the manuscript. This work was funded by the Consortium for Clean Coal Utilization at Washington University and the U.S. Department of Energy (DE-FE0023382).

Supporting Information

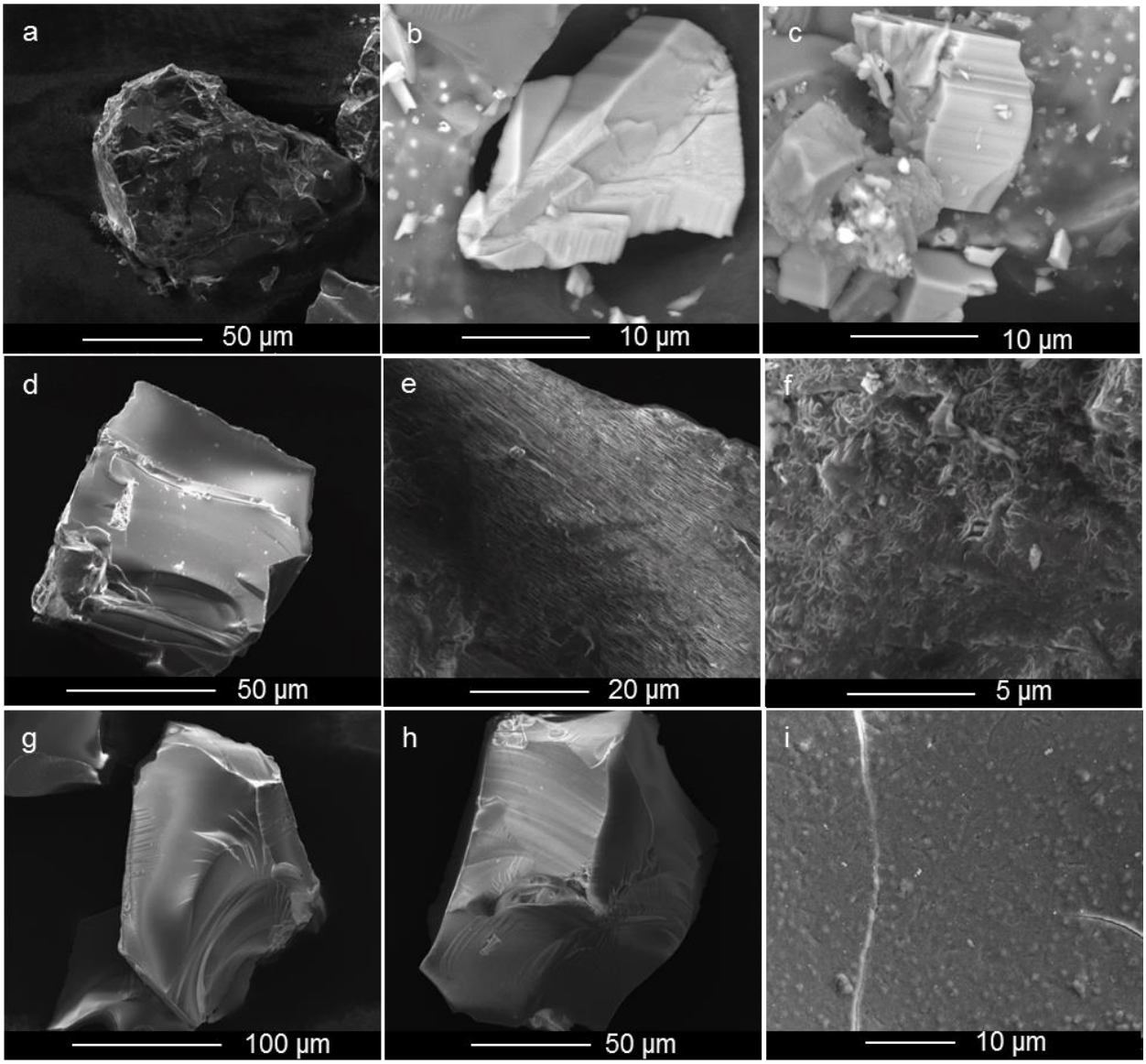

Figure S3.1 SEM-SE images of a) unreacted flood basalt, b) siderite growth in pyramid geometry in flood basalt packed bed, d) siderite in column geometry in flood basalt packed bed, d) unreacted serpentinized basalt, e) and f) surface of the reacted serpentinized basalt powder at two magnifications, g) unreacted basaltic glass, and h) and i) surface of the reacted basaltic glass powder at two magnifications.

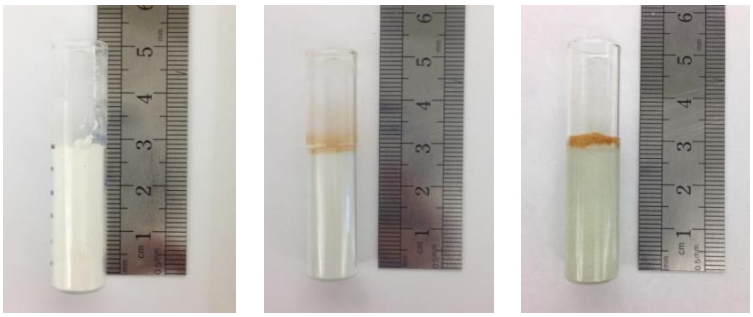

Figure S3.2 Photos of the olivine packed beds after reaction. a) 0-53 µm forsterite packed bed. b) 0-53 µm olivine packed bed. c) 53-106 µm olivine packed bed.

Table S3.1 WDS data point composition of the precipitate shown in Figure 3.3f

Na wt%	Mg wt%	Al wt%	Si wt%	K wt%	Ca wt%	Mn wt%	Fe wt%	Ti wt%	O wt%	C wt%	Total	Composition
0.05	3.00	0.02	0.07	0.00	0.52	0.68	40.56	0.03	43.21	10.92	99.04	$Fe_{0.81}Mg_{0.14}Ca_{0.01}CO_3$

Raman spectroscopy standards information

The following standards are from RRUFF online database.

Name: Siderite

RRUFF ID: R050349

Ideal Chemistry: $FeCO_3$

Locality: Litchfield County, Connecticut, USA

Source: California Institute of Technology

Owner: RRUFF

Description: Grayish brown rhombohedral cleavage fragment

Status: The identification of this mineral has been confirmed by X-ray diffraction and chemical analysis

Chemistry

RRUFF ID: R050349.2

Sample Description: Microprobe Fragment

Measured Chemistry: $(Fe_{0.83}Mg_{0.09}Mn_{0.05}Ca_{0.01})_{\Sigma=0.98}CO_3$

Raman Spectrum: R050349 Unoriented 532nm

Name: Calcite

RRUFF ID: R040070

Ideal Chemistry: $CaCO_3$

Locality: Pryor Mountain, Big Horn County, Montana, USA

Source: University of Arizona Mineral Museum 6965 [view label]

Owner: RRUFF

Description: Orange scalenohedral crystals

Status: The identification of this mineral has been confirmed by X-ray diffraction and chemical analysis

Chemistry

RRUFF ID: R040070.2

Sample Description: Microprobe Fragment

Measured Chemistry: $(Ca_{0.99}Mg_{0.01})CO_3$

Raman Spectrum: R040070 Unoriented 532nm

Name: Magnesite

RRUFF ID: R040114

Ideal Chemistry: $MgCO_3$

Locality: Snarum, Norway

Source: University of Arizona Mineral Museum 7562 [view label]

Owner: RRUFF

Description: Tan colored cleavage fragment

Status: The identification of this mineral has been confirmed by X-ray diffraction and chemical analysis

Chemistry

RRUFF ID: R040114.2

Sample Description: Microprobe Fragment

Measured Chemistry: $(Mg_{0.98}Fe_{0.01})C_{1.00}O_3$

Raman Spectrum: R040114 Unoriented 532nm

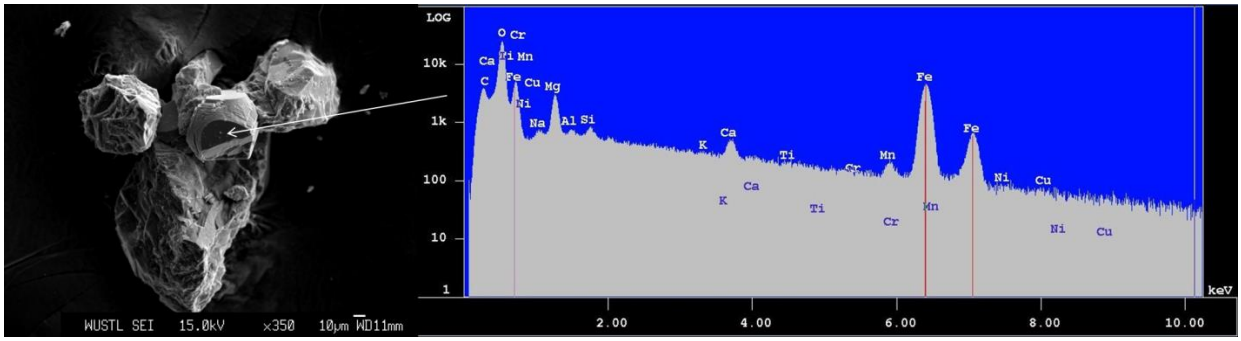

Figure S3.3 SEM image with EDS analysis for the siderite in flood basalt

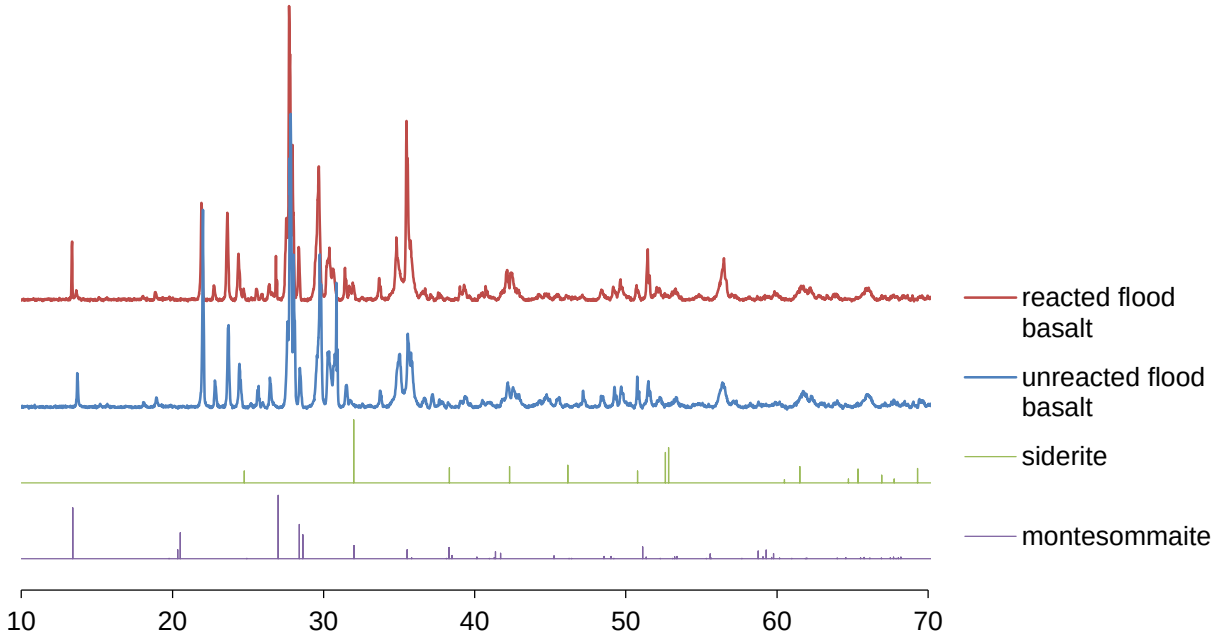

Figure S3.4 XRD spectra of unreacted and reacted flood basalt, with standards of siderite ($FeCO_3$, PDF 00-029-0696) and montesommaite ($K_{2.15}Na_{0.1}Al_{2.25}Si_{5.75}O_{16}(H_2O)_{2.5}$, PDF 04-017-1392) that match the new peaks after reaction. Comparison between XRD spectra before and after reaction shows new peaks after reaction. The new peaks at $2\theta = 31.9$ and 24.7 match with siderite standard, indicating the formation of siderite after reaction.

Mass Balance Calculations

Flood basalt

To list mass balance equations to relate the concentrations of elements in the bulk solution to the amounts of silicate minerals that dissolved, we make the following assumptions:

1. Ca and Mg are trace amounts in siderite that forms, and the siderite is pure $FeCO_3$

2. All Al is from plagioclase.

3 The silicate minerals dissolve congruently.

The K-rich matrix can be normalized to the composition $Ca_{0.04}Na_{0.33}K_{0.64}Fe_{0.01}Al_{1.06}Si_{2.93}O_8$, but it is not a single mineral phase. Its dissolution would contribute dissolved Al, but Al concentrations are very low, indicating very limited dissolution of the matrix. Consequently, we neglect the dissolution of the K-rich matrix in the mass balance calculations.

We also neglect serpentine and orthopyroxene because these two minerals only make up 1% of the flood basalt and they are not very reactive minerals compared to olivine.

We designate the amount of minerals (in mmol) that dissolved with letters and indicate their exact compositions and total abundances (by mass percentage) below.

plagioclase = a, pyroxene = b, olivine =c

a	plagioclase	31%	$Ca_{0.59}Na_{0.4}Fe_{0.03}Al_{1.57}Si_{2.4}O_8$
b	pyroxene	22%	$Ca_{0.63}Fe_{0.48}Mg_{0.83}Ti_{0.03}Al_{0.09}Si_{1.92}O_6$
c	olivine	9%	$Mg_{1.21}Fe_{0.78}Ca_{0.01}SiO_4$
	K-rich matrix	33%	neglect
	orthopyroxene	1%	neglect
	serpentine	1%	neglect

To solve for the three unknown variables (a, b, and c), we need three unique equations. Here we use Ca, Mg, and Al mass balance equations (1-1, 1-2, and 1-3). The Ca and Mg are major cations dissolved in the bulk solution. We do not include a mass balance equation for Fe, because part of the Fe had converted to carbonate minerals and iron oxides in the bed and is not released to the bulk solution.

Al balance $1.57a\ mmol = 0.008\ mmol/L \times 0.2\ L$ (1-1)

Ca balance $0.59a + 0.63b + 0.01c\ mmol = 0.27\ mmol/L\ \times 0.2\ L$ (1-2)

Mg balance $0.83b + 1.21c\ mmol = 0.63\ mmol/L\ \times 0.2\ L$ (1-3)

By solving Eqs. (1-1), (1-2) and (1-3), we calculate the amounts of minerals that had dissolved.

		mmol
a	plagioclase	0.001
b	pyroxene	0.084
c	olivine	0.046

Amounts of cations from individual minerals:

mmol	Plag	Pyx	olivine	Sum
Ca	0.0006	0.0529	0.0005	0.0540
Mg	--	0.0697	0.0557	0.1254
Fe	0.0000	0.0403	0.0359	0.0762

The percentages of the total released amounts of each element that are estimated to have come from specific minerals are given below.

%	Plag	Pyx	olivine
Ca	1.09	98.05	0.85
Mg	0.00	55.61	44.39

Fe	0.04	52.89	47.07

Serpentinized basalt

For serpentinized basalt, the mass balance equations are similar to those performed for the flood basalt. We make the same three assumptions used above for the flood basalt. As with the flood basalt we also assume that the K-rich matrix and plagioclase dissolution are negligible. However, for the serpentinized basalt, we do include serpentine with an estimated formula of $Na_{0.01}Mg_{0.6}Al_{0.27}K_{0.01}Ca_{0.11}Mn_{0.05}Fe_{1.82}Si_3O_9H_x$. We do not have a definitive chemical formula for the serpentine because of a lack of OH information from the WDS analysis, and this estimate introduces some uncertainty into the calculations.

The K-rich matrix can also release Mn, which is not considered in the Mn balance. This may result in the overestimation of olivine and serpentine.

We designate the amounts (in mmol) of minerals that dissolved with letters.

plagioclase = a, pyroxene = b, serpentine = c, olivine =d

a	plagioclase	28%	$Ca_{0.55}Na_{0.43}Fe_{0.02}Al_{1.57}Si_{2.43}O_8$
b	pyroxene	21%	$Ca_{0.83}Fe_{0.25}Mg_{0.85}Ti_{0.03}Al_{0.07}Si_{1.96}O_6$
c	serpentine	14%	use assumed formula
d	olivine	1%	$Mg_{1.38}Fe_{0.59}Mn_{0.02}Si_{1.01}O_4$
	K-rich matrix	32%	neglect
	orthopyroxene	1%	neglect

With the addition of an initial dissolving mineral phase, we need an additional equation to solve for the four unknowns. We add Mn mass balance here.

Mass balance equations

Al balance $1.57a\ mmol = 0.005\ mmol/L \times 0.2\ L$ (2-1)

Ca balance $0.55a + 0.83b + 0.11c\ mmol = 0.31\ mmol/L \times 0.2\ L$ (2-2)

Mg balance $0.85a + 0.6c + 1.38d\ mmol = 0.64\ mmol/L \times 0.2\ L$ (2-3)

Mn balance $0.04c + 0.02d\ mmol = 0.02\ mmol/L \times 0.2\ L$ (2-4)

By solving Eqs. (2-1), (2-2), (2-3) and (2-4), we can get the amounts of the minerals that had dissolved.

		mmol
a	Plagioclase	0.001
b	pyroxene	0.062
c	serpentine	0.093
d	olivine	0.014

Released cations from individual minerals:

mmol	Plag	Pyx	Srpt	olivine	Sum
Ca	0.00033	0.0515	0.0102	--	0.0620
Mg	--	0.0527	0.0558	0.0193	0.1278
Fe	1.2E-05	0.0155	0.1693	0.0083	0.1930

The percentages of the total released amounts of each element that are estimated to have come from specific minerals are given below.

%	Plag	Pyx	Srpt	olivine
Ca	0.53	82.97	16.49	--
Mg	0.00	41.23	43.66	15.12
Fe	0.01	8.03	87.68	4.28

Reaction path modeling done in Geochemists' Workbench 8.0

The minerals in the flood basalt were assigned to different end-members that are documented in the GWB default database to give the same amount of cations. React temperature was set at 100˚C. At 100˚C, 100 bar CO_2, the calculated CO_2(aq) is 0.81 mol/kg based on Duan and Sun's model (Reference 21). The CO_2(aq) was fixed as an open system.

The flood basalt amount in the packed bed was 3.65 g. Different mineral amounts were calculated according to their composition in the basalt.

The water volume was 200 mL (as in the bulk solution) or 1.26 mL (as inside the packed bed). These two water volumes represent bounding conditions for interpretation of the actual system.

Input in React

Fixed CO_2(aq)

Flood basalt composition			**Input**	formula	mol	**g**	**g**
pyroxene	22%	0.803 g	**Diopside**	$CaMgSi_2O_6$	0.00053	**0.16**	
$Ca_{0.63}Fe_{0.48}Mg_{0.83}Ti_{0.03}Al_{0.09}Si_{1.92}O_6$			**Hedenbergite**	$CaFe(SiO_3)_2$	0.00177	**0.44**	
simplify	$Ca_{0.65}Fe_{0.5}Mg_{0.85}Si_2O_6$	0.0035 mol	**Enstatite**	$MgSiO_3$	0.00124	**0.12**	**0.15**
olivine	9%	0.329 g	**Forsterite**	Mg_2SiO_4	0.00112	**0.16**	
$Mg_{1.21}Fe_{0.78}Ca_{0.01}Si_{1.00}O_4$			**Fayalite**	Fe_2SiO_4	0.00073	**0.15**	
simplify	$Mg_{1.21}Fe_{0.79}SiO_4$	0.0018 mol					
serpentine	1%	0.037 g	**Greenlite**	$Fe_3Si_2O_5(OH)_4$		**0.03**	
Fe : Mg=2.45			**Chrysotile**	$Mg_3Si_2O_5(OH)_4$		**0.01**	
K-matrix	33%	1.205 g	**K-Feldspar**	$KAlSi_3O_8$	0.00287	**0.80**	
$Ca_{0.04}Na_{0.33}K_{0.64}Fe_{0.01}Al_{1.06}Si_{2.93}O_8$			**Albite**	$NaAlSi_3O_8$	0.00154	**0.41**	**0.84**
simplify	$Na_{0.35}K_{0.65}AlSi_3O_8$	0.0044 mol					
orthopyroxene	1%	0.037 g	**Enstatite**	$MgSiO_3$		**0.03**	
Mg : Fe=1.31:0.59			**Ferrosilite**	$FeSiO_3$		**0.01**	
plagioclase feldspar	31%	1.132 g	**Anorthite**	$CaAl_2Si_2O_8$	0.00247	**0.69**	
$Ca_{0.59}Na_{0.40}Fe_{0.03}Al_{1.57}Si_{2.40}O_8$			**Albite**	$NaAlSi_3O_8$	0.00167	**0.44**	
simplify	$Ca_{0.59}Na_{0.4}Al_{1.58}Si_{2.4}O_8$	0.0042 mol					

Suppress: Dolomite-ord, Dolomite, Dolomite-dis, Quartz, Tridymite, Chalcedony, Cristobalite

1) 200 mL water

This is the boundary condition in which the total amount of flood basalt in the packed bed would react with all 200 mL of water in the reactor as a well-mixed system.

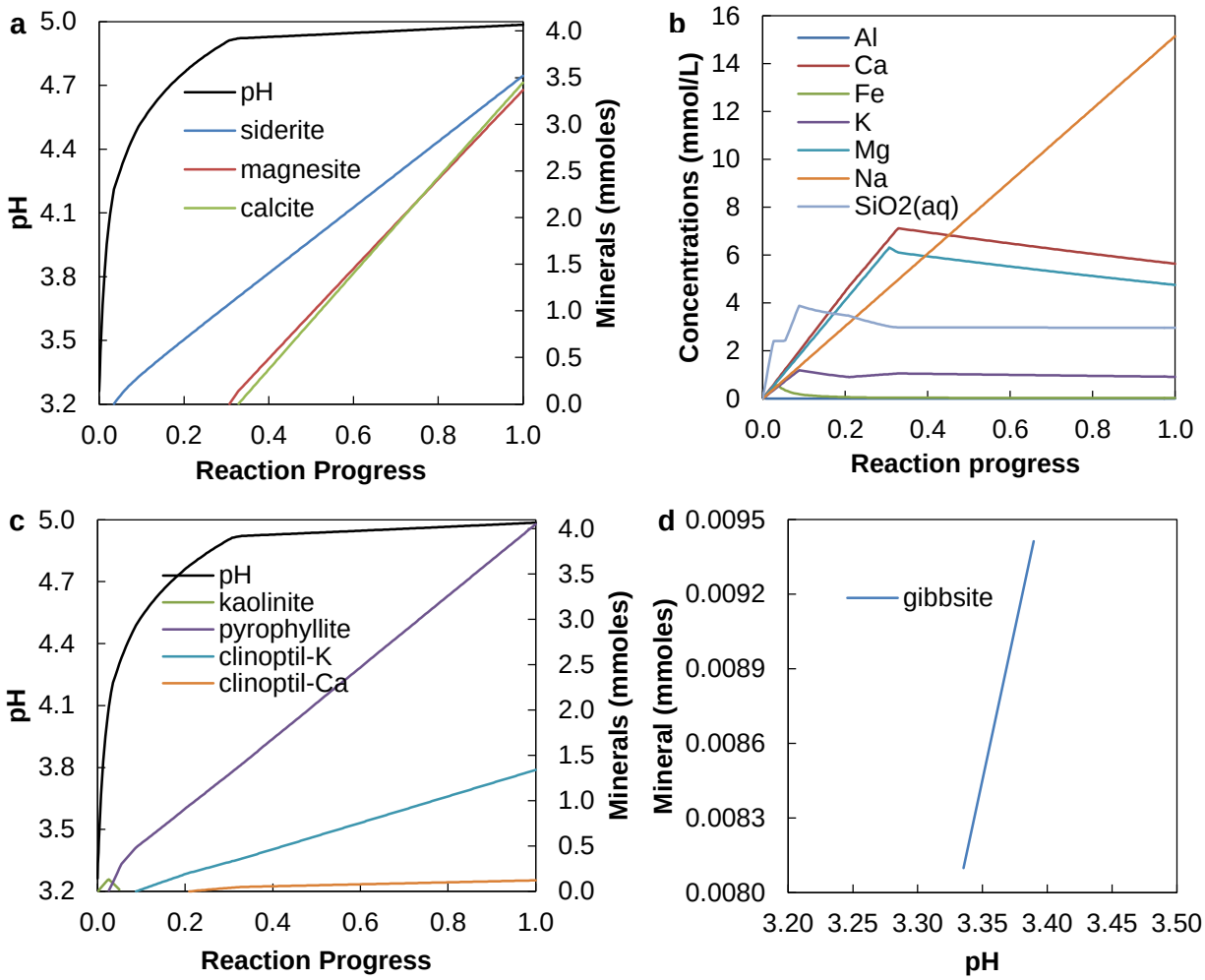

Figure S3.5 a) Carbonate mineral formation and pH evolution as a function of reaction progress in 200 mL water; b) Dissolved ion concentrations in the aqueous phase as a function of reaction progress in 200 mL water; c) Secondary silicate mineral formation and pH evolution as a function of reaction progress in 200 mL water; d) Gibbsite formation as a function of pH in 200 mL water.

2) 1.26 mL water

This is the boundary condition in which the flood basalt in the packed bed only reacts with the 1.26 mL of water present in the pore space of the packed bed.

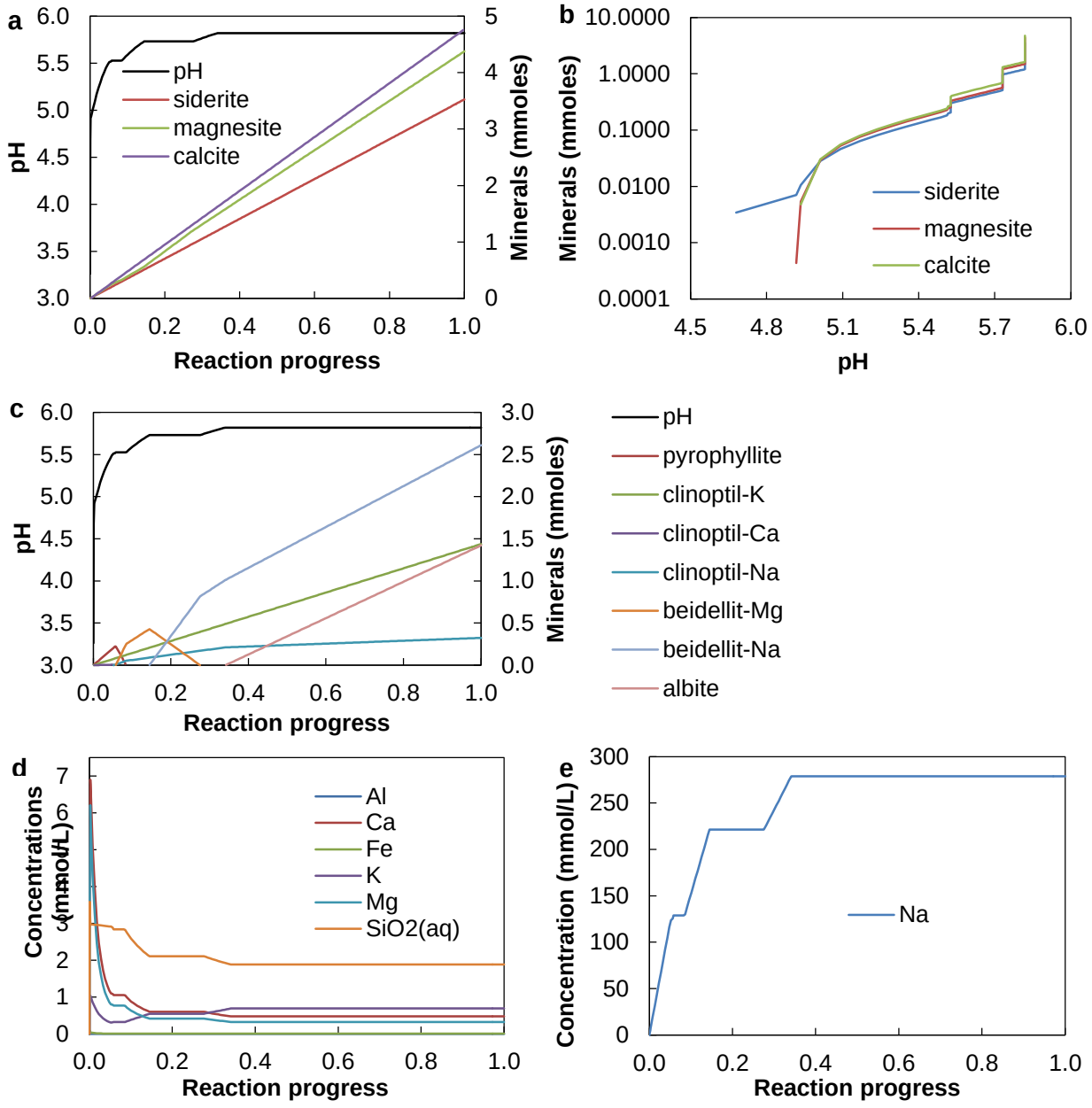

Figure S3.6 a) Carbonate mineral formation and pH evolution as a function of reaction progress in 1.26 g water; b) Carbonate mineral formation as a function of pH in 1.26 g water; c) Secondary silicate mineral formation and pH evolution as a function of reaction progress in 1.26

g water; d) Dissolved ion concentrations in the aqueous phase as a function of reaction progress in 1.26 g water; e) Dissolved Na^+ concentration in the aqueous phase as a function of reaction progress in 1.26 g water.

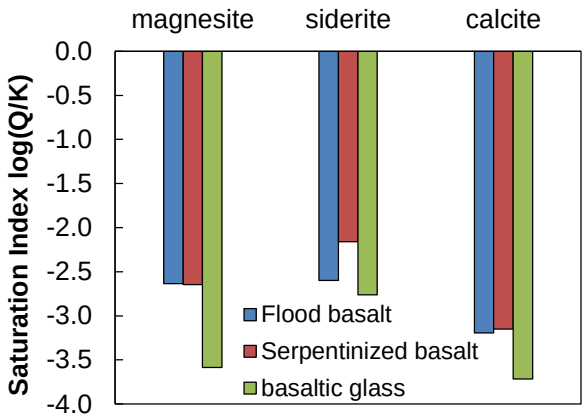

Figure S3.7 Calculated saturation indices of magnesite, siderite and calcite in the bulk solution based on measured dissolved ions.

Chapter 4. Carbon Sequestration in Fractured Basalt Cores

Abstract

Basalt is a potential host rock for geologic carbon sequestration due to its high mineral trapping capacity. Fractures in basalt can provide substantial surface area for reactions, and limited mass transfer in fractures can allow accumulation of carbonate-forming cations. In this study, flood basalt and serpentinized basalt with artificially created fractures were reacted in water equilibrated with 100 bar CO_2 at 100˚C or 150˚C for up to 40 weeks. Carbonation in the basalt fracture was experimentally observed as early as 6 weeks. Mg- and Ca-bearing siderite minerals were observed in both basalts reacted at 100˚C, and Mg-Fe-Ca carbonate minerals formed in the fractured flood basalt cores reacted at 150˚C. Carbonate minerals in the flood basalt had a maximum amount in a particular location, but this carbonate-rich zone did not completely block the fracture. X-ray μCT segmentation shows that 5.4% and 15% of the flood basalt fracture was filled with carbonate precipitates after 40 weeks of reaction at 100˚C and 150˚C, respectively. Limited siderite clusters were found in localized areas in the serpentinized basalt. A reactive transport model was developed in CrunchTope to examine how geochemical gradients drive silicate mineral dissolution and carbonate precipitation in the fracture. The model predicts the formation of siderite-dominant carbonate minerals as early as 1 day. The predicted location of maximum siderite abundance is consistent with experimental observations, and the predicted total carbonate volume predicted is comparable to that estimated by CT segmentation.

4.1 Introduction

Geological carbon sequestration can reduce CO_2 emissions to the atmosphere by injecting captured CO_2 into deep geologic formations [3, 76]. Most injections are in porous sedimentary rocks, which have large storage capacity but limited mineral trapping capacity [77]. Basalt is a potential host rock for CO_2 sequestration due to its great mineral trapping capacity of CO_2 [12]. Basalt is an igneous rock rich in Ca-, Mg- and Fe-bearing minerals that can react with dissolved CO_2 to form carbonate minerals, thereby trapping the injected CO_2 in stable solid phases. A recent report on the CarbFix site in Iceland revealed that 95 % of the injected CO_2 into basalt was converted into carbonate minerals within 2 years [19]. At the Big Sky basalt pilot project in Washington State, extensive carbon mineralization of injected CO_2 was also observed after two years [22]. These timescales for mineral trapping are orders of magnitude shorter than those anticipated for sandstone reservoirs [78].

Basalt is rich in divalent cations for carbonation reactions. Major divalent cations such as Ca, Mg and Fe present in carbon mineralization source minerals, such as olivine [$(Fe,Mg)_2SiO_4$], pyroxene [$(NaCa)(Mg,Fe,Al)(Al,Si)_2O_6$] and plagioclase feldspar [$NaAlSi_3O_8$-$CaAl_2Si_2O_8$] [14]. Olivine has the fastest dissolution rate and largest mineral trapping capacity among common basalt-forming minerals [14, 35].. The injected CO_2 dissolves in water, decreases the pH and accelerates the dissolution of the silicate minerals. The dissolution of the minerals releases divalent cations and also increases the pH, which increases the amount of carbonate ion present. Ultimately carbonate minerals that include calcite, magnesite, siderite and ankerite can precipitate [14, 18]. Olivine can be weathered to serpentine, which is hydrous magnesium iron silicate mineral [14].

The majority of exposed reactive surfaces in basalt reservoirs are located in pores and fractures. Solute transport in such fractures can be limited to diffusion, and overall transport processes may be influenced by the coupling of transport processes and geochemical reactions. The formation of carbonate minerals has the potential to (a) inhibit further mineral trapping by blocking fracture throats, (b) self-accelerate mineral trapping by creating new fractures through the volume expansion associated with replacement of silicate minerals with carbonate minerals [18], or (c) have no effect on trapping if carbonate minerals form uniformly in the fracture. Our limited understanding of the interaction between diffusive transport and dissolution/precipitation reactions in fractured basalt poses challenges to accurately estimating the storage capacity of fractured basalt. The objectives of this study are to determine when, where and what types of carbonate minerals form in fractures of basalt and to explore the influence of carbonation on transport and reactions in the fracture.

4.2 Results and Discussion

4.2.1 Siderite and Fe-Mg-Ca Carbonate formation

Mg- and Ca-bearing siderite (Figure 4.1, Figure S4.1) was observed in the fractures of the flood basalt (FB) and serpentinized basalt (SB) after reacting in water equilibrated with 100 bar CO_2 at 100˚C as early as 6 weeks. Raman spectra of the precipitates have diagnostic peaks for siderite (Figure S4.2). For the flood basalt, siderite formed on the surface of the basalt fracture. Typical precipitate sizes increased from 20 µm at 6 weeks to ~100 µm at 40 weeks. For serpentinized basalt, siderite formed in large mm-scale clusters with individual crystals growing in different orientations (Figure S4.1a). The clusters tended to occur on red areas that could be

large serpentine or pyroxene grains covered by iron oxides (Figure S4.3). A small amount of amorphous silica formed on the siderite surfaces. For flood basalt reacted at 150˚C, a Fe-Mg-Ca carbonate formed with similar amounts of Fe and Mg and less Ca (Figure 4.1b). The richer Mg-content of the this carbonate shifted the Raman peaks to higher frequency than those of the Fe-rich siderite formed at 100˚C (Figure S4.2) [67], and the precipitates were 100~200 μm after 40 weeks. Previous long-term static experiments with different flood basalts also showed significant differences in precipitate compositions and morphologies [57].

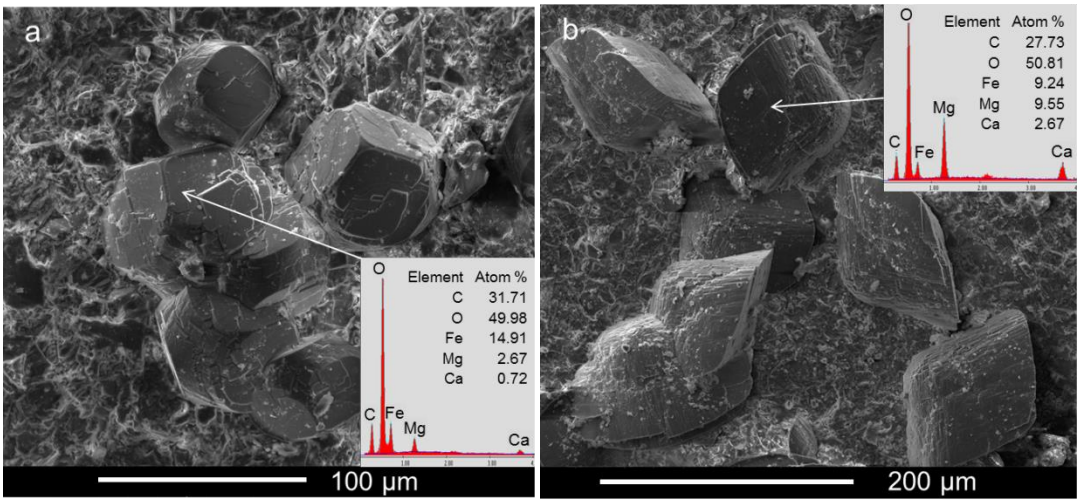

Figure 4.1 Carbonate minerals formed in the milled fracture surfaces of flood basalt after reactions for 40 weeks with a) a siderite precipitate formed at 100˚C in water equilbrated with 100 bar CO_2 and b) Fe-Mg-Ca carbonate formed at 150˚C in water equilibrated with 100 bar CO_2.

Siderite has been predicted to form in basalt in previous studies but has only rarely been observed in field and laboratory research. In the CarbFix project calcite formed at the site conditions of 20-30˚C and alkaline pH of 8.4-9.4 [19]. Other carbonate minerals such as ankerite, siderite and mixed Ca-Mg-Fe carbonates were not observed although they were supersaturated in the monitoring fluids [79]. In the Big Sky CO_2 injection into the Columbia River Basalt (CRB),

ankerite nodules [$Ca(Fe,Mg,Mn)(CO_3)_2$] precipitated in the basalt pores at the site conditions of 77 bar and 36-44˚C [22]. In laboratory study in which similar CRB as in the Big Sky project reacted in CO_2-rich water for 180 days, calcite was identified at 120~255 bar, 55~116˚C while kutnohorite [$Ca(Mn,Ca)(CO_3)_2$] formed at 310 bar and 137˚C. [80] An experimental study with Icelandic basaltic glass found that the main carbonation products are Ca-Mg-Fe carbonates for reactions below 100˚C and that calcite became dominant for reactions above 150˚C. [26] Another study with mid-ocean ridge basalt (MORB) provided evidence that Fe-bearing magnesite formed at 150˚C and 280 bar CO_2 [23]. In our previous study with powder packed beds of the same flood basalt, Mg- and Ca-bearing siderite was observed at 100˚C, 100 bar CO_2 within 4 weeks [55].

In this study the observed precipitation of siderite in the flood basalt fracture was consistent with modeling results and measured bulk fluid compositions. The precipitates observed were carbonate solid solutions with dominant Fe and Mg and Ca substitutions (Figure 4.1). The reactive transport modeling predicts carbonate mineral formation as early as 1 day and indicates that siderite is the thermodynamically most favorable carbonate mineral in the basalt after 40 weeks of reaction (Table 4.1). The model can only predict pure carbonate mineral end-members, which is a limitation when its output is compared to experimental results with carbonate minerals that contain cation substitutions. Calcite is predicted to precipitate quickly and to then re-dissolve (Table S4.1). Although magnesite is supersaturated sometimes (Figure S4.4), little magnesite is predicted to form. Siderite and calcite quickly reach saturation status and precipitate (Figure S4.4). In the experiment, the bulk solution chemistry provides information on basalt dissolution from the top surface of the cores. After 40 weeks of reaction the most abundant divalent cation in the bulk solution was Mg^{2+} followed by Ca^{2+} and Fe^{2+} (Figure S4.5). The model-predicted order of Mg^{2+}, Ca^{2+} and Fe^{2+} concentrations in the fracture

from highest to lowest (Figure S4.6) is consistent with the experimentally measured concentrations in the bulk solution. The solubility product (K_{sp}) of siderite is two orders of magnitude smaller than magnesite and calcite (Table S4.2). At the experimental conditions, siderite has the highest calculated saturation indices in the bulk solution (Figure S4.7), followed by magnesite and calcite. The calculated pH is 3.2 initially and rises to 4~5 after reaction both in the bulk solution and the model system (Figure S4.7d, Figure S4.8).

Table 4.1 Estimated carbonate mineral volume in the 100 μm fracture of the cores reacted for 40weeks

Quantification methods	40-week samples	FB 100C	SB 100C	FB 150C
Modeling prediction of precipitate volume in the fracture domain (mm^3)	Calcite	0	0	0.70
	Magnesite	1.89×10^{-4}	3.86×10^{-5}	1.25
	Siderite	1.04	0.51	1.42
	Total carbonate	1.04	0.51	3.37
CT segmentation of precipitates in the fracture (mm^3)	Precipitates	1.73	0.39	7.09
	Fraction[a]	5.43 %	0.88 %	14.75 %

[a] Percentage of the initial fracture volume that becomes filled with carbonates.

4.2.2 Uneven distribution of precipitates

Carbonate minerals were unevenly distributed along the flood basalt fracture as observed using CT imaging (Figure 4.2). More siderite precipitated on the milled surface (Figure 4.2b) than the polished smooth surface (Figure 4.2d). The precipitate volume in every 5 mm layer from the fracture inlet to the bottom was estimated by CT segmentation (Figure 4.3a, Figure S4.9). For flood basalt reacted at 100˚C, limited siderite formed near the fracture inlet. More siderite formed towards the middle and the amount decreased toward the bottom of the fracture. The location of the maximum siderite abundance occurred at 10-25 mm from the fracture inlet. Some carbonate precipitates were large enough to span the 100-μm fracture. Individual precipitates

were generally larger at 150˚C than at 100˚C (Figure 4.2e). CT segmentation showed that most carbonate precipitates formed at distances 10 mm or more from the fracture inlet (Figure S4.9c). As observed with optical microscopy, carbonate minerals formed on the entire fracture surface (Figure S4.10c), forming a sugar-like coating after 30~40 weeks of reaction. A lot of smaller precipitates (~20 μm) which could not be captured by CT due to resolution limitation were observed in the top 3 mm of the fracture (Figure S4.11). The formation of small precipitates may have been affected by the cooling and degassing process during sample collection. Larger precipitates are probably more representative of the carbonate minerals that formed during the cumulative reaction time. In serpentinized basalt reacted at 100˚C, siderite minerals formed in mm-scale clusters at locations deeper in the fracture zone (Figure 4.2h, Figure S4.10b). The porphyritic serpentinized basalt contains mm-scale mineral grains. Zones near large pyroxene and serpentine grains might have created localized supersaturated environments for precipitation. Siderite was less abundant (Figure S4.9a) in serpentinized basalt than in the flood basalt reacted at 100˚C.

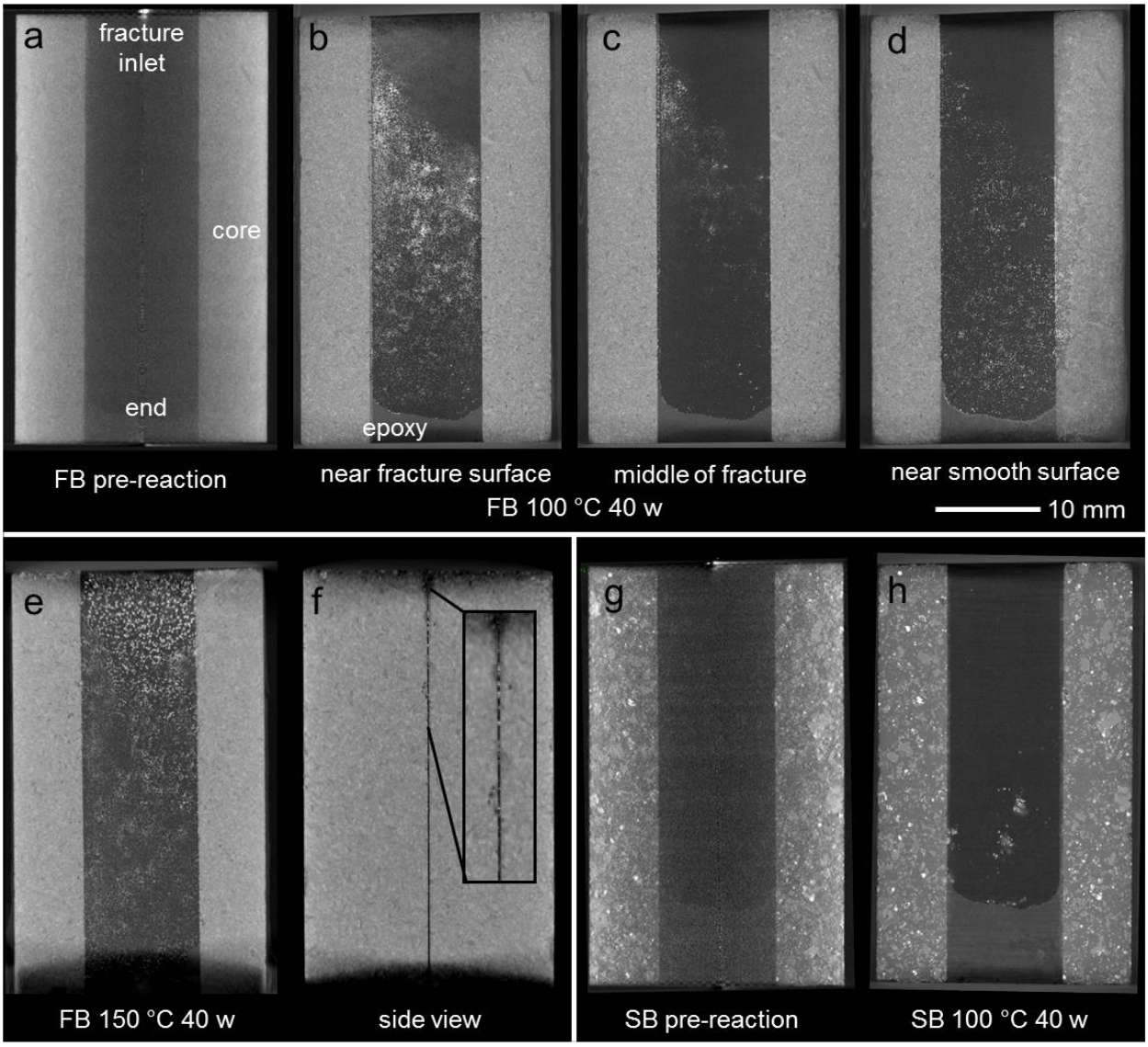

Figure 4.2 X-ray CT images of a) The flood basalt before reaction, b) cross section near the milled fracture surface, c) cross section of the middle of the fracture and d) cross section near the smooth surface of flood basalt reacted in 100˚C for 40 weeks. e) The flood basalt milled surface view and f) the fracture side view of flood basalt reacted in 150˚C for 40 weeks. g) The serpentinized basalt before reaction and h) after reaction in 100˚C for 40 weeks.

The spatial distribution of carbonate minerals was also analyzed by point counting. The point count percentage indicates precipitate presence regardless of size at specific depths within the fracture (Figure 4.3a, Figure S4.9). For flood basalt reacted at 100˚C (Figure 4.3a), as total siderite in the fracture increased with longer reaction time, the location of the maximum presence moved towards the fracture inlet, indicating that siderite built up from the inner part of the fracture. The point count trend of carbonate mineral percentage is generally consistent with CT segmentation, except that it indicates appreciable presence of precipitates at deeper parts of the fracture, especially for the flood basalt reacted in 150˚C (Figure 4.9c). Many of the carbonate minerals in the deepest part of the fracture were too small to be resolved by CT, while point counting still confirmed the existence of many small precipitates.

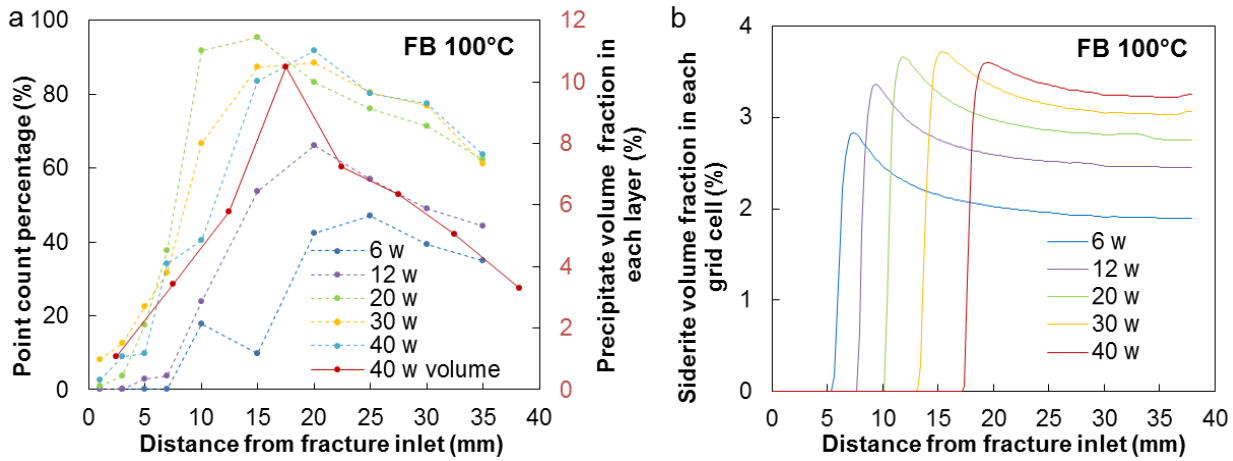

Figure 4.3 a) CT segmentation of precipitate volume fraction in each 5-mm long layer along the fracture in the 40-week flood basalt sample and precipitate point count percentage on the fracture surface. The point count percentage represents the occurrence of carbonates at 110 different locations across the fracture surface at a given distance from the fracture inlet. b) Predicted siderite volume fraction in each grid cell of the fracture domain of flood basalt reacted at 100˚C in reactive transport modeling.

Although certain locations were filled with more carbonate precipitates than others, the transport pathways into the deeper fracture zone were not blocked in our experiments for as long as 40 weeks of reaction. Carbonate mineral formation was also present in deeper fracture below the location where most carbonate minerals occur. For flood basalt reacted at 100˚C for 40 weeks, the largest siderite abundance appeared 15-20 mm from the fracture inlet (Figure 4.3a). CT segmentation estimated that 10.5% of the available fracture space in this 5-mm long region was occupied by carbonate minerals. Even in the maximum precipitation zone, there was still enough space for solutes to diffuse through the fluid in the fracture. Our previous study with olivine packed beds and olivine aggregates also demonstrated that extensive magnesite formation in certain locations would not entirely block mass transfer to and reaction in deeper unreacted zones [27, 81].

The spatial distribution of carbonate precipitation is a result of opposing chemical gradients along the diffusion-limited dead-end fracture as demonstrated in the reactive transport modeling. Confidence in the model was gained by the similar predicted total carbonate volume (Table 4.1) with that determined by CT segmentation and similar predicted siderite spatial distribution to that observed in the experiment (Figure 4.3a). Dissolved CO_2 diffuses into the fracture and the concentration of dissolved inorganic carbon is the highest at the fracture inlet and decreases with distance into the fracture (Figure S4.12). At the fracture inlet, pH is low (Figure S4.8) and the cation concentrations are small as in the bulk solution [63]. Cations released from the minerals on the fracture walls diffuse out of the fracture to the bulk solution driven by concentration differences. The distribution of divalent cations along the length of the fracture (Figure S4.6) is determined by the interactions of dissolution/precipitation reactions and

diffusive transport towards the bulk solution. The predicted siderite formation along the fracture (Figure 4.3b) follows similar spatial distribution trends as observed in the experiment. Only a limited amount of siderite formed near the fracture inlet. The predicted amount of siderite increases sharply below the dissolution-only region and siderite reaches the maximum amount at about 10-20 mm from the fracture inlet in flood basalt reacted at 100˚C. The predicted maximum carbonate extent occurred at the very top region (<10 mm) of the fracture in the flood basalt at 150˚C (Figure S4.9d). For serpentinized basalt reacted in 100˚C, although siderite formed on several localized areas, in general most siderite was in the deeper fracture zone (Figure S4.12a). The predicted maximum siderite location (25 mm) in a 40-week serpentinized basalt core (Figure S4.9b) was consistent with that experimental observation. Other potential secondary precipitates were also predicted by the model (Figure S4.13-S4.15).

The model indicated the source minerals for divalent cations for carbonation reactions. The main composition difference between the flood basalt and the serpentinized basalt is the olivine/serpentine content. The reactive transport modeling shows rapid dissolution of olivine and pyroxene that leads to depletion of these minerals within 40 weeks of reaction in the flood basalt modeling system reacted in 100˚C and 150˚C (Figure S4.16, S4.17). For serpentinized basalt, pyroxene and serpentine are the main sources for divalent cations and dissolve away quickly (Figure S4.18). The plagioclase and the K-rich matrix compositions are similarly abundant in flood basalt and serpentinized basalt. An appreciable amount of plagioclase dissolves during reaction, providing supplementary Ca to the main Ca source of pyroxene. The presence of 9% olivine in the flood basalt allows release of more dissolved Fe^{2+} than from the serpentinized basalt (Figure S4.6), making it possible for more siderite to precipitate in the flood basalt.

A divergence of the current model predictions from experimental observations is that carbonates are predicted to precipitate and then later dissolve at specific locations nearest the fracture inlet (Figure 4.3b). From experimental observations carbonate minerals in the fracture continued to increase at all locations until 20~30 weeks of reaction and became almost stable until 40 weeks (Figure 4.3a). The size of precipitates increased over time in the flood basalt. No obvious re-dissolution happened to the carbonate precipitates within the reaction time. The re-dissolution of carbonate minerals predicted by the model is probably because the model uses a confined-size system with a finite amount of initial silicate minerals. The system can run out of primary minerals to buffer the low pH in a CO_2-rich open system. The model depicts a porous medium that has relevant dimensions to represent the experimental fractured basalt zone. The fractured basalt in the experiment was in a closed system and the bulk environment could become equilibrated later in the experiment. Moreover, during the experiment, the basalt rock surrounding the fracture continued to dissolve and supply cations from near surface zones. Because the walls of the fracture are thick and new mineral surfaces can be exposed as dissolution occurs, it is not likely that any silicate minerals will be completely dissolved away. Overall, the current reactive transport model depicts the chemical gradients along the fracture and estimates the carbonate mineral amount very well despite the limitation of allowing complete depletion of minerals at specific depths in the fracture. In real basalt reservoirs with large spatial scales of reactions in zones moving away from injection sites, it is possible that the carbonate minerals precipitated at early stages following CO_2 injection will actually re-dissolve later.

4.2.3 Conclusions

CO_2 mineralization happened rapidly within 6 weeks in fractured basalt in this experiment and the reactive transport modeling predicts carbonate formation in as early as 1 day. The carbonation products were mainly siderite in this study. Carbonate minerals were unevenly distributed along microfractures. The zones of maximum carbonate formation did not block prevent further mineral trapping reactions in deeper region within the fracture for the conditions of this study.

4.3 Materials and Methods

4.3.1 Fractured basalt cores

Columbia River flood basalt (FB) from Pullman, Washington and serpentinized basalt (SB) from Valmont Butte, Colorado were purchased from Ward's Science. The compositions of the flood basalt and the serpentinized basalt are listed in Table 4.2 [81]. Multiple cylindrical cores with 2.54 cm diameter and 4.3 cm length were made from the two basalts. Each core was cut into half cylinders. A straight 11 mm wide groove was milled on one surface using a milling machine (Roland Model MDX-40a) with a 0.5 mm diamond bur (Figure S4.19). The milled half-cylinder was polished with sandpaper until the groove was 100 μm. The groove depth was determined by comparing the z-value of the spots on the groove and the spots on the closest polished surface in an optical microscope (ZEISS, Observer Z1). The surface of the other half cylinder was also polished. The two half cylinders were attached together to form one cylinder with the 100 μm groove in the middle as a dead-end microfracture. The bottom and the side surfaces of the core

were coated with epoxy (MasterBond EP42HT-2), only exposing the top surface with the fracture opening.

Table 4.2 Basalt compositions [64]

Composition	Flood basalt (FB)	Serpentinized basalt (SB)
pyroxene	22% $Ca_{0.63}Fe_{0.48}Mg_{0.83}Ti_{0.03}Al_{0.09}Si_{1.92}O_6$	21% $Ca_{0.83}Fe_{0.25}Mg_{0.85}Ti_{0.03}Al_{0.07}Si_{1.96}O_6$
Olivine	9% $Mg_{1.21}Fe_{0.78}Ca_{0.01}SiO_4$	1% $Mg_{1.38}Fe_{0.59}Mn_{0.02}Si_{1.01}O_4$
Serpentine	1%	14% $Mg_{0.6}Al_{0.27}Ca_{0.11}Mn_{0.05}Fe_{1.82}Si_3O_9H_x$
Matrix and glass	33% $Ca_{0.04}Na_{0.33}K_{0.64}Fe_{0.01}Al_{1.06}Si_{2.93}O_8$	32% $Ca_{0.03}Na_{0.32}K_{0.66}Fe_{0.05}Al_{1.05}Si_{2.94}O_8$
Plagioclase	31% $Ca_{0.59}Na_{0.40}Fe_{0.03}Al_{1.57}Si_{2.40}O_8$	28% $Ca_{0.55}Na_{0.43}Fe_{0.02}Al_{1.57}Si_{2.43}O_8$
Other minerals [a]	4%	4%

[a] Other minerals include 1% orthopyroxene, 3% ilmenite in FB; 1% orthopyroxene, 3% of apatite, chromite and glass in SB

4.3.2 Batch experiments

Three batch experiments were conducted. In each batch, five cores were placed on a multilevel PTFE holder, which was in a PTFE liner inside of a 600 mL stainless steel high pressure vessel (Parr Instrument) (Figure S4.20). Ultrapure water (320 mL in total, 64 mL per core) was added to fully immerse the cores at the beginning of the experiment. Reactions with FB cores and Batch with SB cores were heated to 100˚C and a third reactor with FB cores was heated to 150˚C by heating tapes (Omega, CSi32 Series). A headspace of 100 bar CO_2 was maintained by a syringe pump (500D, Teledyne Isco). Core samples were collected together with 64 mL of the bulk aqueous solution in the reactors after reacting for 6, 12, 20, 30 and 40 weeks.

Aqueous samples were filtered using 0.2 μm PES syringe filters (Environmental Express). Before starting each experiment, 10 bar CO_2 was pumped into the reactor headspace and was immediately degassed to 1 bar for three times to minimize residual O_2. The process of cooling and depressurizing for sample collection and restarting the reactor was ~5 hours.

4.3.3 Analytical methods

The 40-week cores were scanned by X-ray computed tomography (CT) before (Scanco uCT 40, voxel resolution 15 μm) and after reaction (Zeiss Xradia Versa 520, 23.8-24.8 μm, and Nikon Metrology XTH225, 20.5 μm). CT segmentation on precipitates was done using Ilastic code [82] (detailed description in SI). After CT scanning of intact cores was performed, the two half cylinders were separated. Optical microscopy (LEICA, DFC295) was used to detect precipitates along the milled surface. Raman spectra of observable precipitates were collected with a laser Raman microprobe using a 532 nm laser (HoloLab Series 5000, Kaiser Optical). The precipitate morphology and elemental composition were examined by scanning electron microscopy and energy dispersive X-ray spectroscopy (FEI Nova 230). The precipitate distribution on the groove was assessed by both CT segmentation on the precipitate volume in each 5 mm layer and a point counting station (LEICA, DM2700p) with a 10X objective. The point counting was carried out by moving a 100 μm square field of view step-by-step horizontally across the 11-mm wide fracture (110 steps) at certain fracture depths and counting the number of squares that contained a precipitate regardless of precipitate size or abundance. The carbonate point count percentage at each depth is the percentage of the number of squares with carbonate in them divided by the total squares counted. Aqueous samples were analyzed by

inductively coupled plasma mass spectrometry (Perkin Elmer, Elan DRC II) and ion chromatography (Theromo Scientific, DIONEX ICS-1600).

4.3.4 1D reactive transport modeling

The models were developed in CrunchTope [83]. Details of the model are in the supporting information. The fractured basalt core is modeled as an equivalent porous medium with dimensions and water:rock ratios calculated from the geometry (Figure S4.21) of the reactive zone of the fracture in the core based on observations from pre- and post-reaction CT scans. A constant flux (Dirichlet) boundary, consisting of pure water equilibrated with CO_2 at 100 bar and the experimental temperature (100˚C or 150˚C), was imposed at the inlet. CO_2 fugacity was calculated directly in the code [54]. Diffusion was the only transport mechanism considered in the system with fixed diffusion coefficients [84]. The input of primary minerals was based on mineral composition of the basalts [64]. Calcite, magnesite, siderite, amorphous silica, and gibbsite were included as secondary precipitates. The precipitation was defined by volume fraction which was updated at each time step according to user-defined specific surface areas (Table S4.3) from literature [85-88]. Mineral dissolution and precipitation are assumed to proceed reversibly according to the transition state theory. In the absence of adequate precipitation kinetic data, literature-reported dissolution rate equations [89-94] are applied to account for precipitation rates given the assumption of reversible reactions (Table S4.4).

Acknowledgements

We thank Professor Jill Pasteris for her help in Raman spectroscopy. We thank Dr. Hélène Couvy for helping to prepare core samples. We thank Daniel Leib and Professor James Fitzpatrick for their help in X-ray Computed Tomography. This work was funded by the U.S. Department of Energy (DE-FE0023382).

Supporting Information

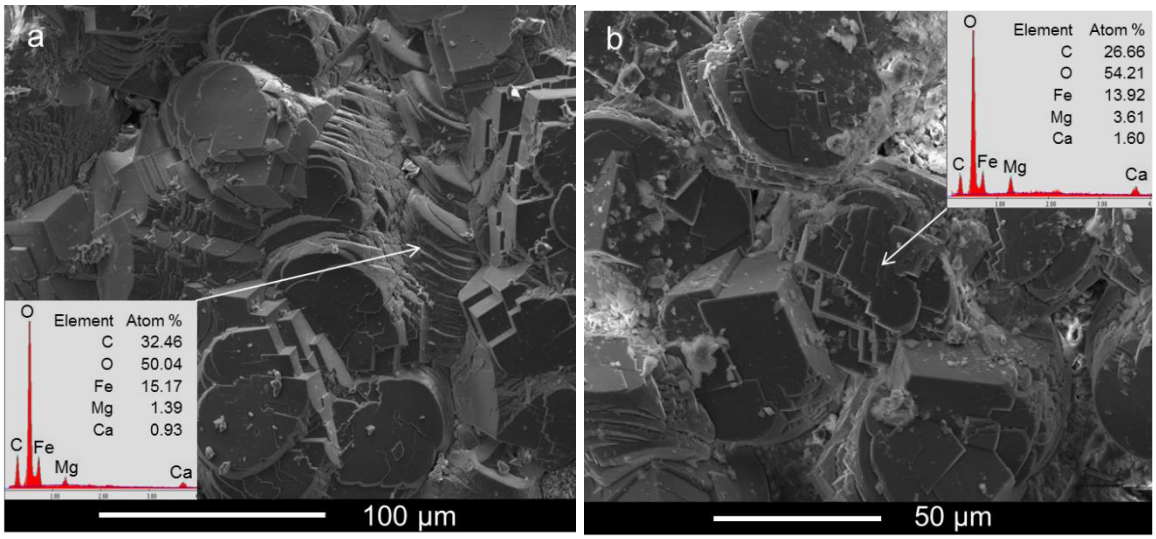

Figure S4.1 Carbonate minerals formed in the milled fracture surfaces with a) siderite cluster on in serpentinized basalt reacted at 100˚C in water equilbrated with 100 bar CO_2 for 40 weeks, b) a siderite precpitate in flood basalt reacted reacted at 100˚C in water equilbrated with 100 bar CO_2 for 20 weeks.

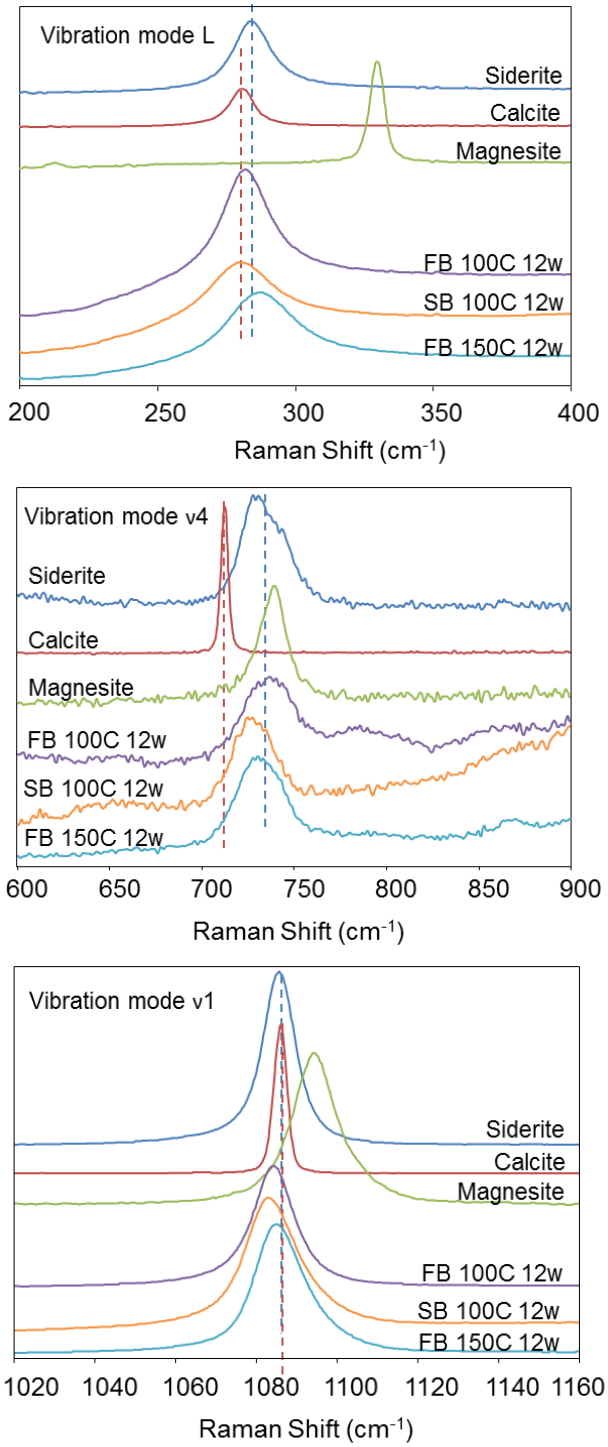

Figure S4.2 Comparison of Raman spectra of precipitates on flood basalt reacted at 100˚C and 150˚C and serpentinized basalt reacted at 100˚C with siderite, calcite and magnesite standards. Raman peaks in the range of a) 200-400 cm^{-1}; b) 600-900 cm^{-1}; c) 1020-1160 cm^{-1}.

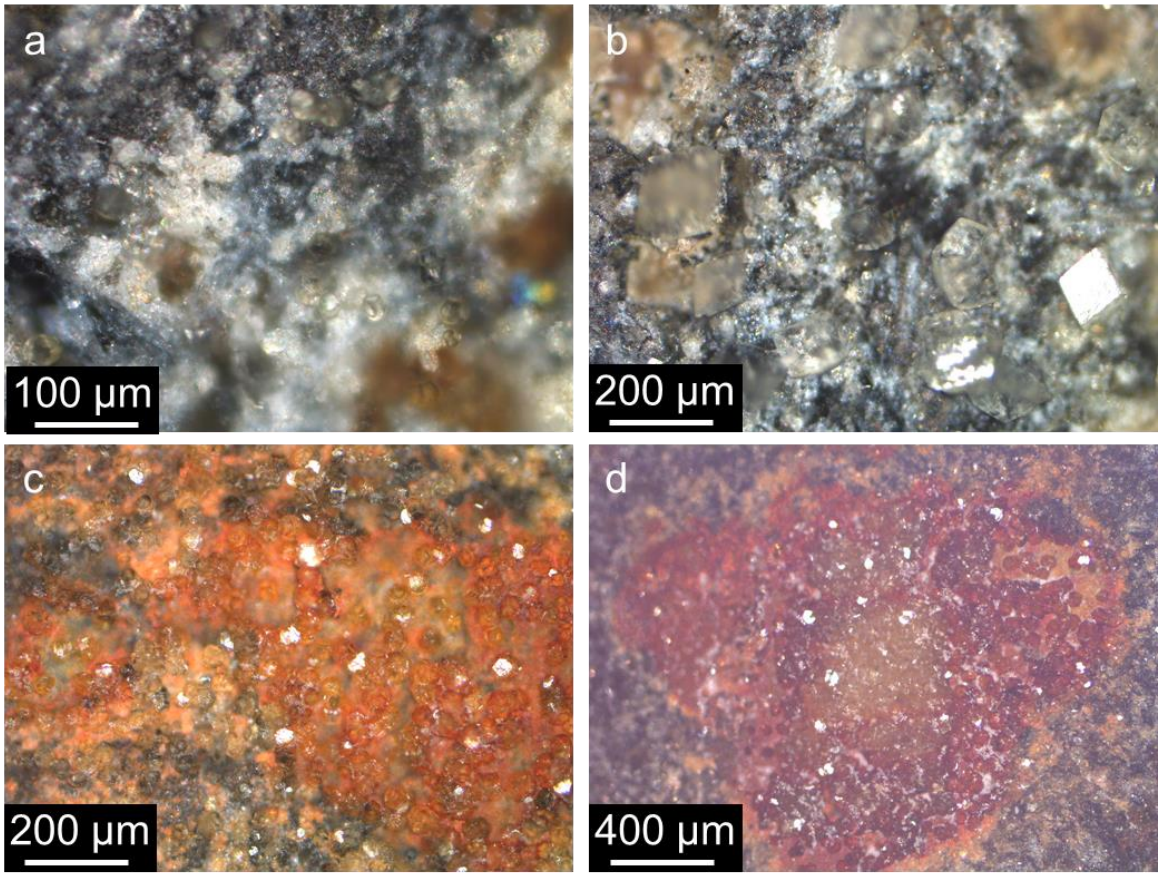

Figure S4.3 Optical microscopic images of a) precipitates at 1 cm from the fracture inlet on the milled surface of flood basalt reacted at 100˚C 100 bar for 6 weeks, b) precipitates at 1 cm from fracture inlet on the milled surface of flood basalt reacted at 150˚C 100 bar for 12 weeks, c) precipitates at 1 cm from fracture inlet on the milled surface of serpentinized basalt reacted at 100˚C 100 bar for 6 weeks, d) precipitates at 1 cm from fracture inlet on the milled surface of serpentinized basalt reacted at 100˚C 100 bar for 12 weeks.

Table S4.1 Predicted carbonate volume in the entire fracture during reaction

Reaction time	6 weeds	12 weeks	20 weeks	30 weeks	40 weeks
FB 100C (mm^3)					
total calcite	0.27	0.38	0.25	0.00	0.00
total magnesite	1.99×10^{-4}	2.64×10^{-4}	2.63×10^{-4}	2.29×10^{-4}	1.89×10^{-4}
total siderite	1.01	1.24	1.26	1.21	1.04
Total carbonate	1.28	1.62	1.51	1.21	1.04
SB 100C (mm^3)					
total calcite	0.576	0.627	0.256	0	0
total magnesite	0.000	0.000	0.000	7.00×10^{-5}	3.86×10^{-5}
total siderite	0.288	0.432	0.510	0.529	0.509
Total carbonate	0.864	1.059	0.766	0.529	0.509
FB 150C (mm^3)					
total calcite	1.71	1.51	1.28	0.99	0.70
total magnesite	1.53	1.49	1.42	1.34	1.25
total siderite	1.61	1.56	1.51	1.46	1.42
Total carbonate	4.86	4.56	4.21	3.79	3.37

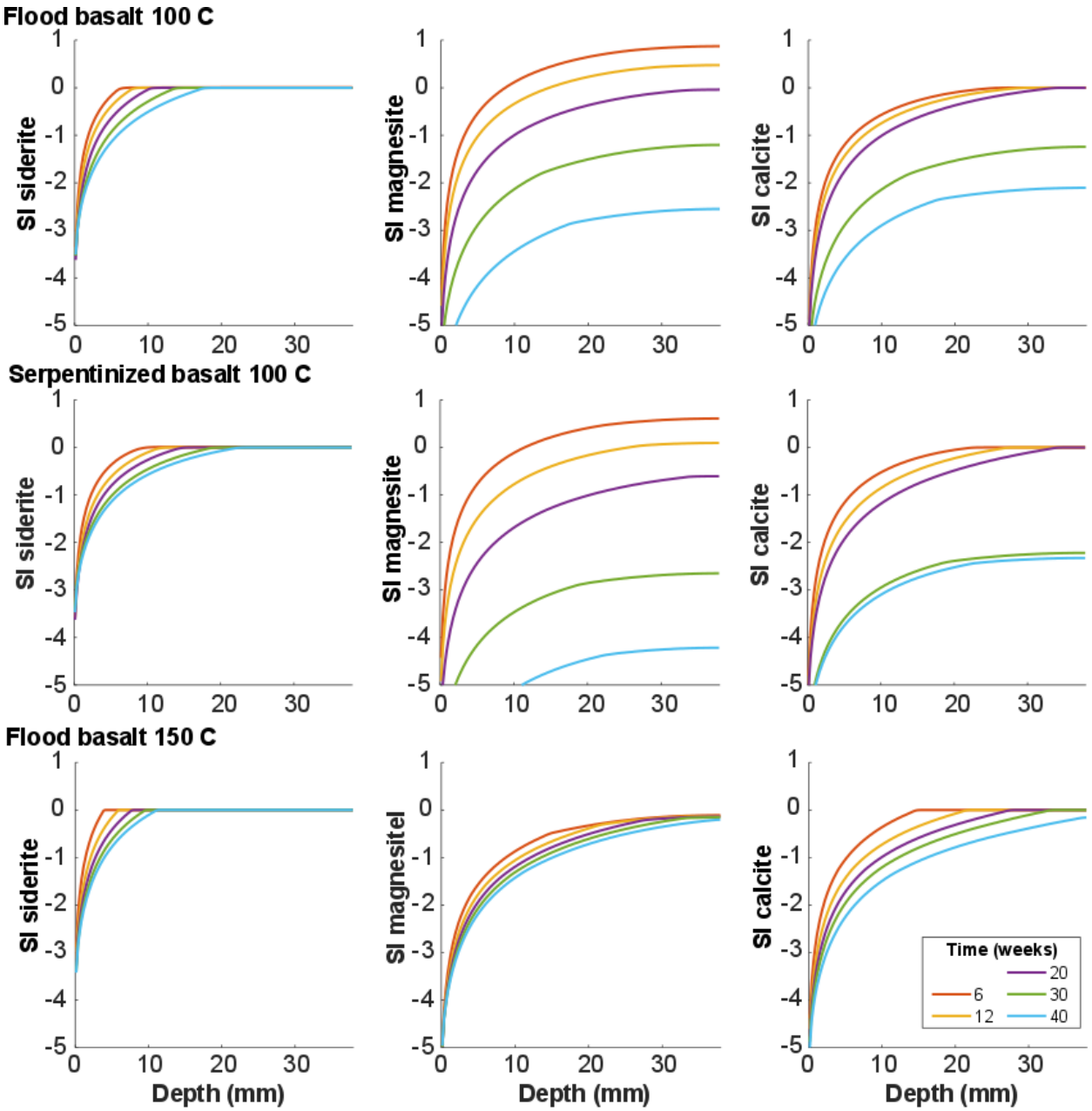

Figure S4.4 Saturation indices of magnesite, calcite and siderite predicted by the model. Magnesite is supersaturated in some cases but is not kinetically allowed to precipitate. Depth is the distance from the fracture inlet.

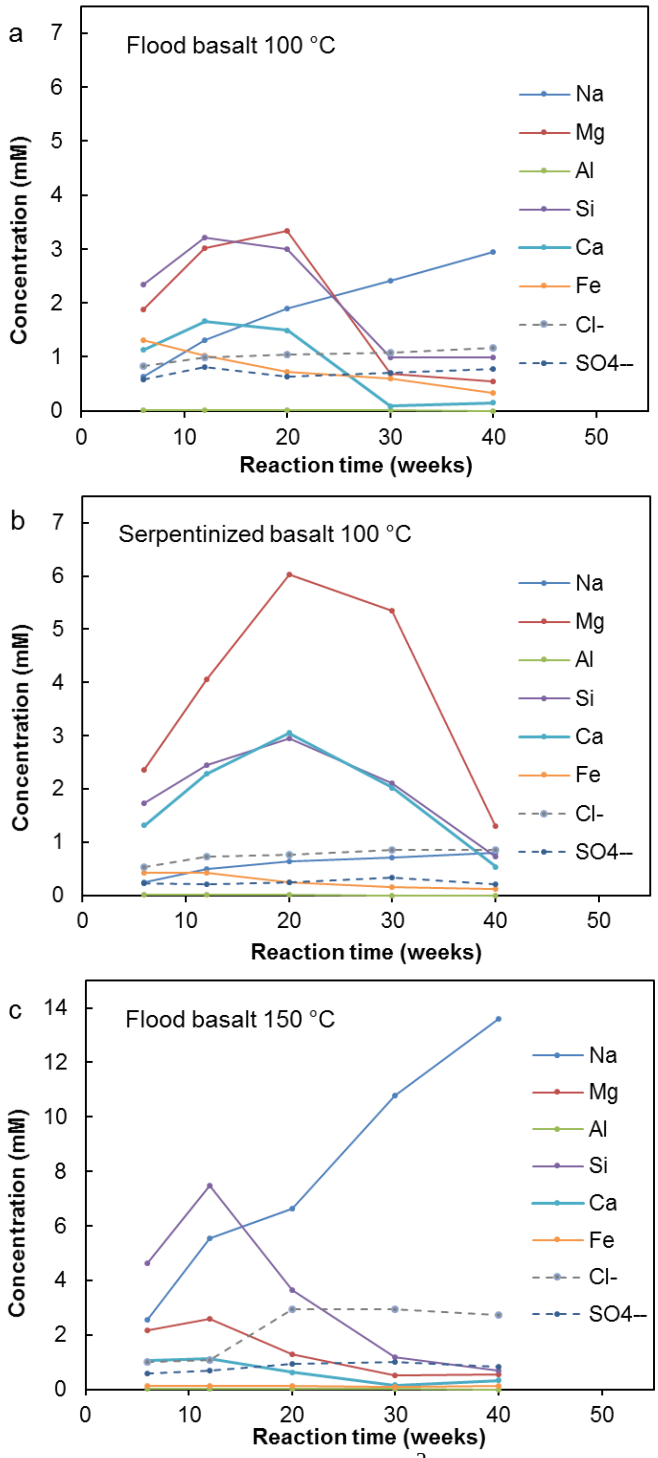

Figure S4.5 Dissolved cations, $SiO_{2(aq)}$, Cl^- and SO_4^{2-} in the bulk solution of a) flood basalt reacted at 100˚C; b) serpentinized basalt reacted in 100˚C; c) flood basalt reacted at 150˚C.

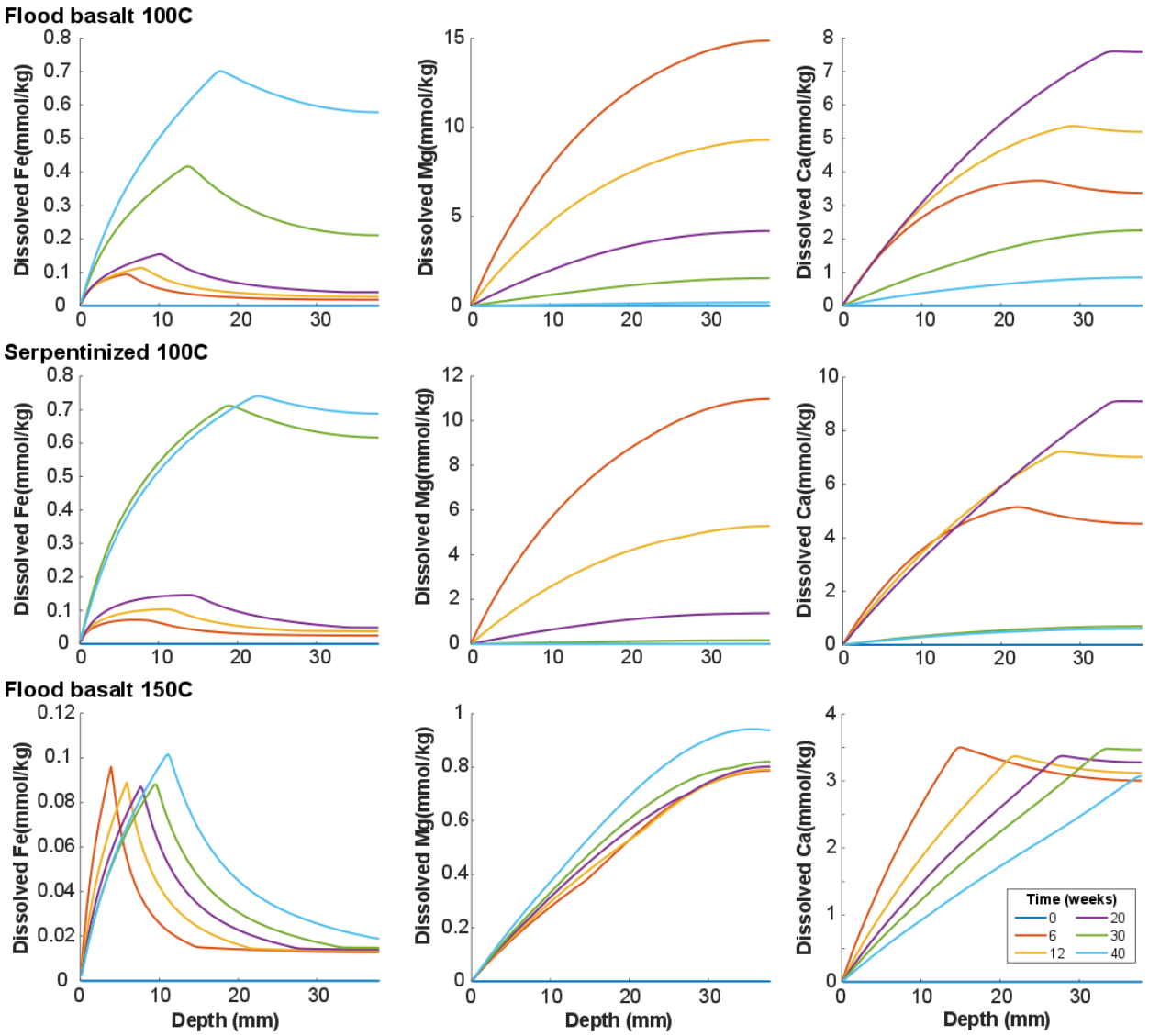

Figure S4.6 Predicted dissolved divalent cation concentrations in the fracture domain predicted by the model. The concentrations are zero at 0 mm, which is the fracture inlet directly contacting the infinite diluted bulk solution in the model. Depth is the distance from the fracture inlet.

Table S4.2 Solubility products at 100 bar (calculated from SUPCRT 92)

Log K_{sp}	100˚C	150˚C
siderite	-11.489	-12.374
magnesite	-9.408	-10.461
calcite	-9.216	-10.006
amorphous silica	-2.162	-1.959

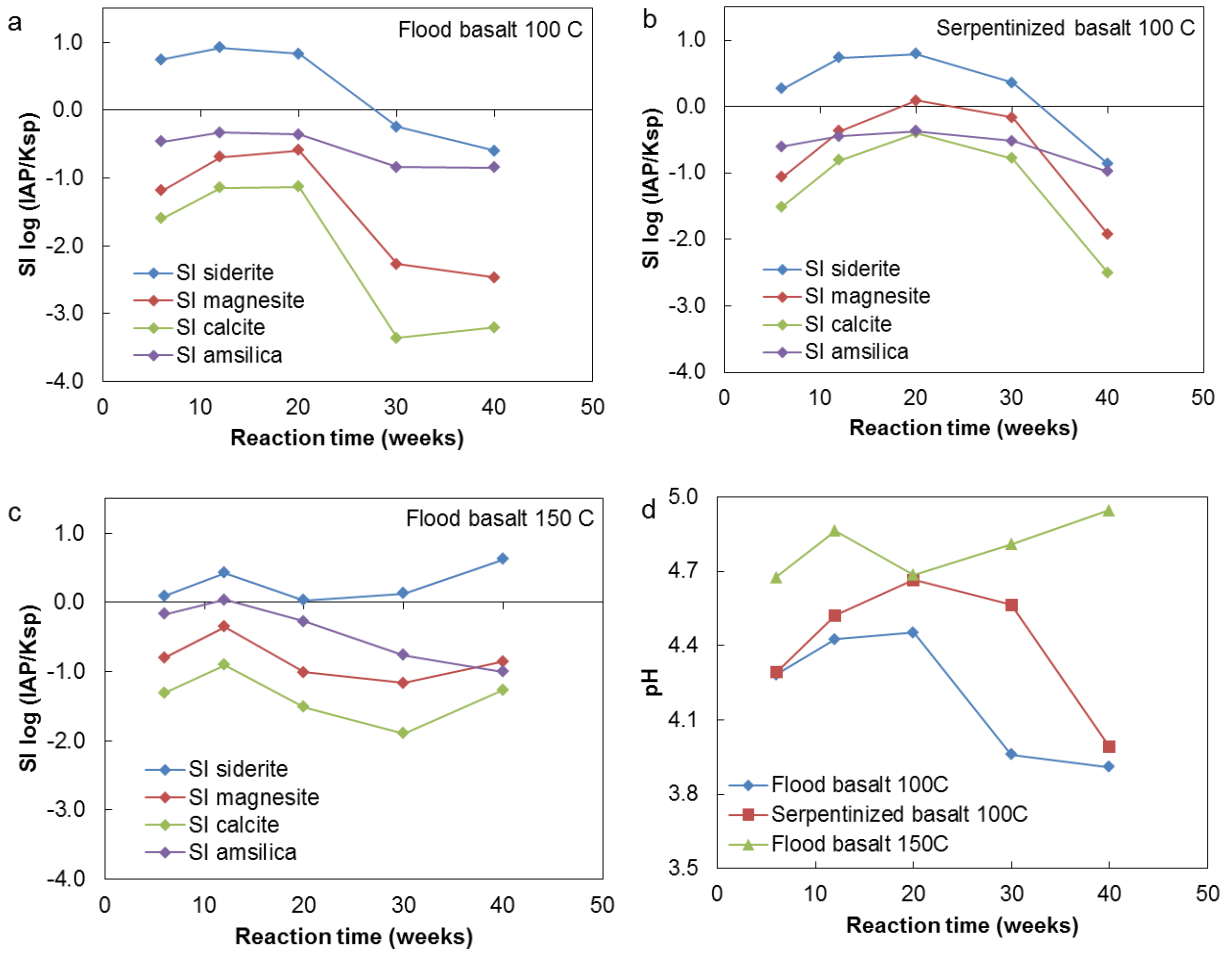

Figure S4.7 Saturation indices of the water in the bulk solution outside of the cores with the milled fractures for a) flood basalt reacted at 100˚C and 100 bar CO_2; b) serpentinized basalt reacted in 100˚C 100 bar CO_2; c) flood basalt reacted at 150˚C and 100 bar CO_2. d) Calculated pH of the bulk solution in three batches.

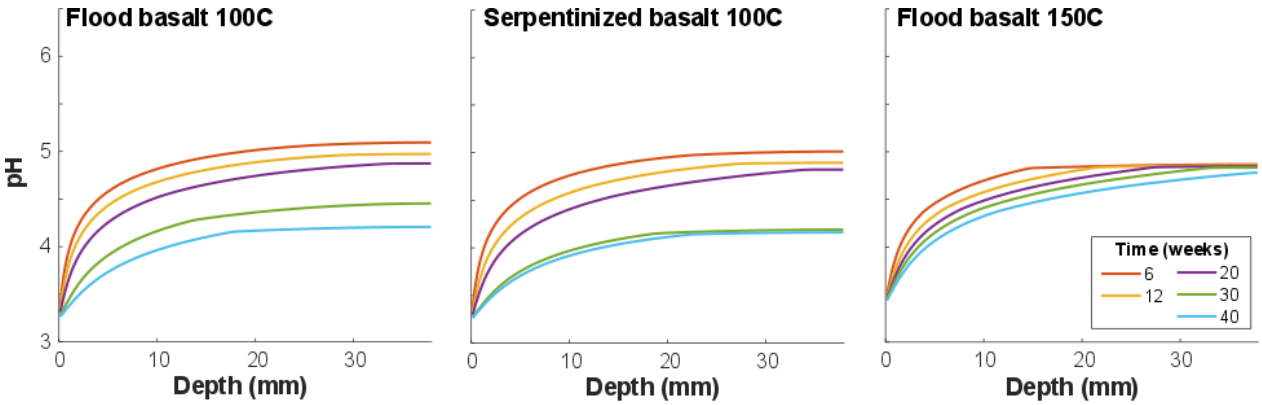

Figure S4.8 Calculated pH profiles in the fractures of the cores. Depth is the distance from the fracture inlet.

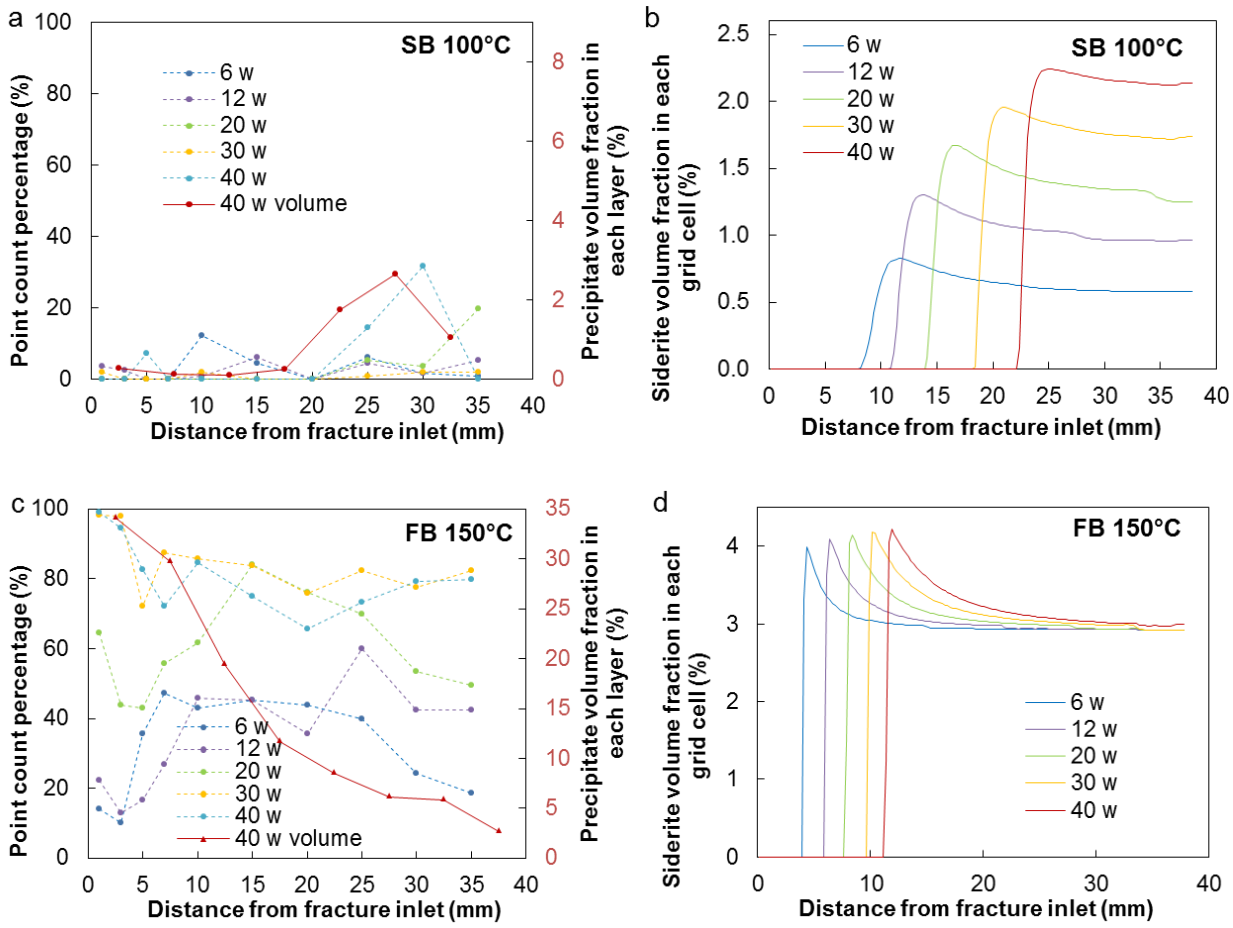

Figure S4.9 a) CT segmentation of precipitate volume in the 40-week samples and precipitate point count percentage on the groove and b) predicted siderite volume fraction inside the fracture domain of serpentinized basalt reacted at 100˚C. c) CT segmentation of precipitate volume in the 40-week samples and precipitate point count percentage on the groove and d) predicted siderite volume fraction inside the fracture domain of flood basalt reacted at 150˚C. The point in the Point count represents the percentage of precipitation occurrence on a horizontal line. The point in the Percentage volume represents the CT segmented precipitate volume in a 5 mm layer.

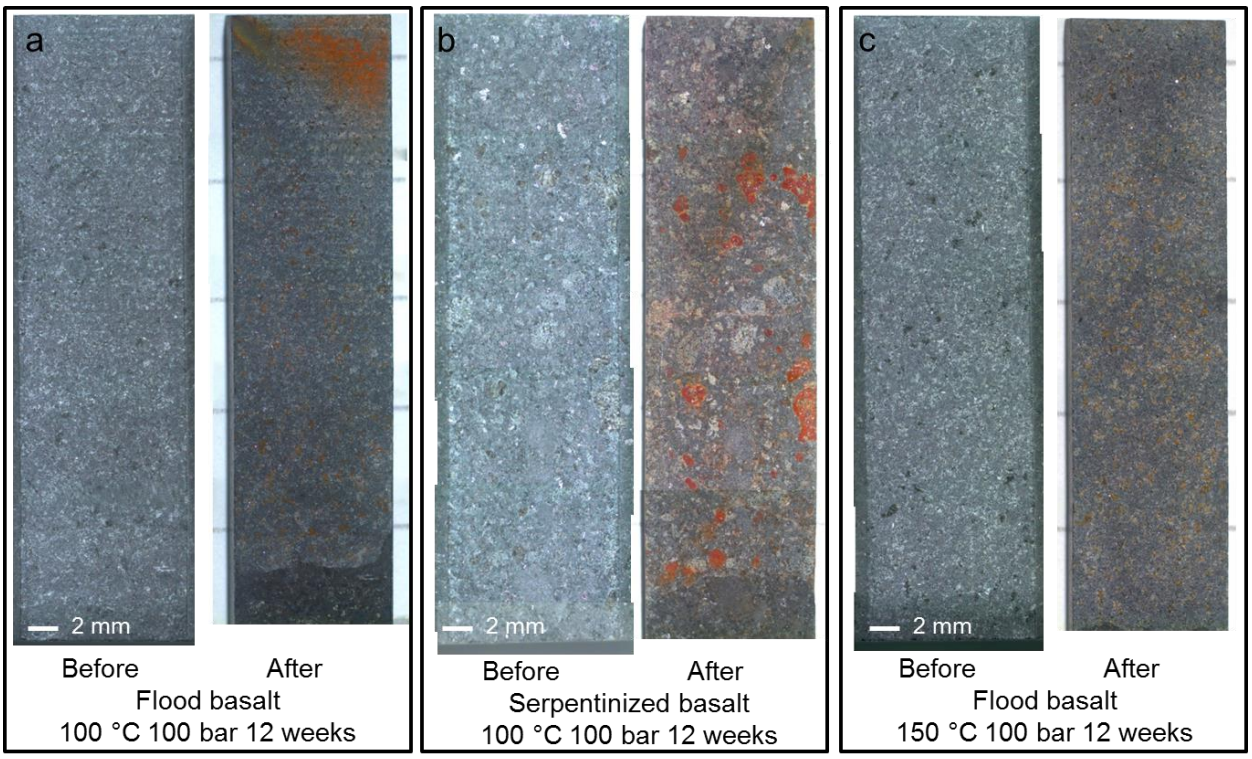

Figure S4.10 Optical micrographs of basalt fracture surfaces before and after reaction.

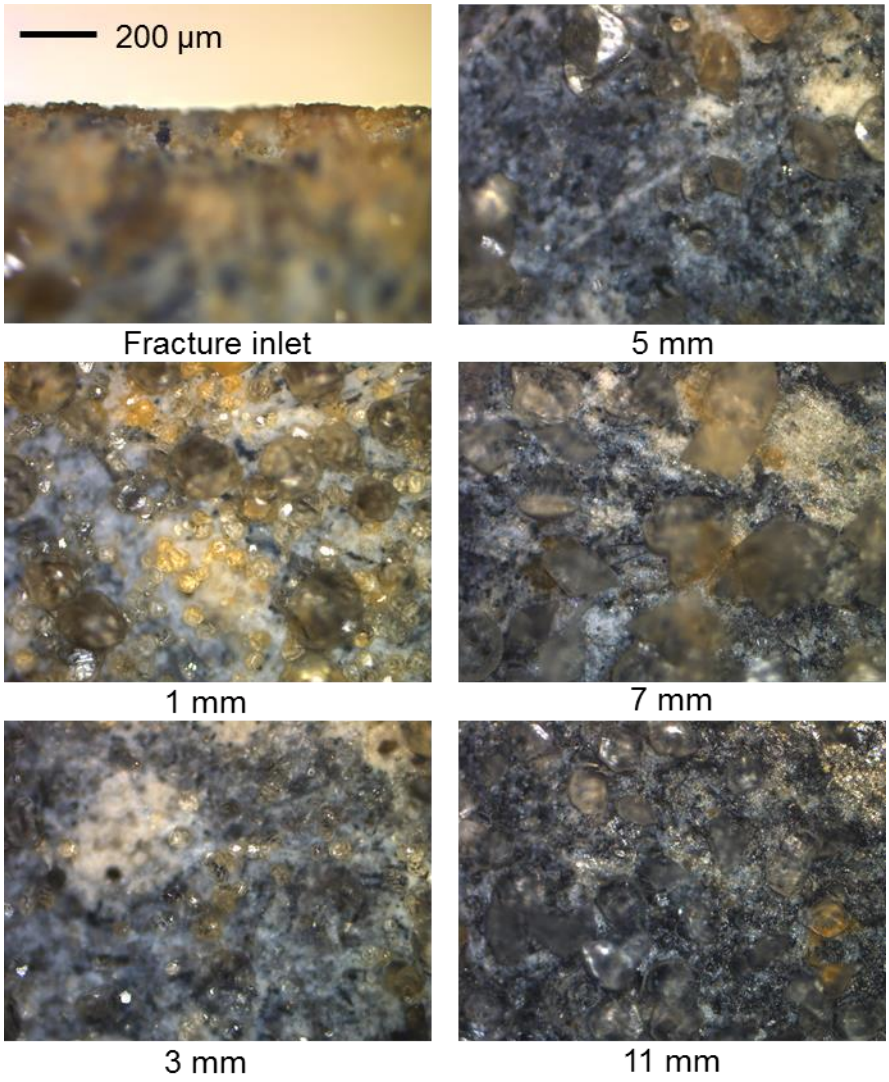

Figure S4.11 Optical micrographs of the groove surface of the fracture in the flood basalt reacted at 150˚C for 30 weeks.

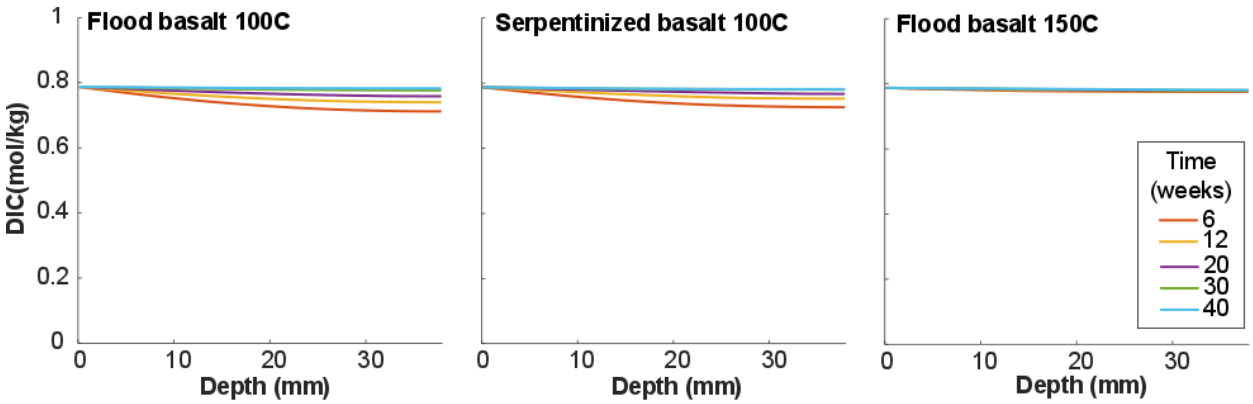

Figure S4.12 Dissolved inorganic carbon along the fracture. Depth is the distance from the fracture inlet.

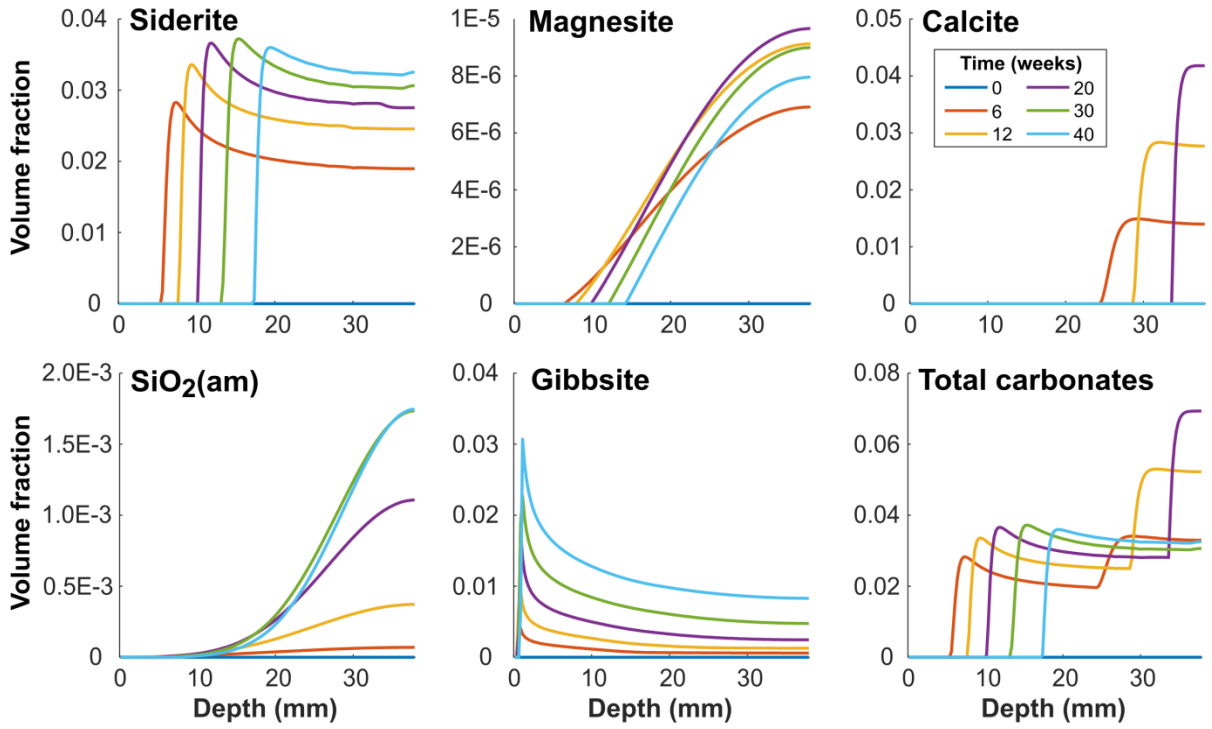

Figure S4.13 Predicted volume fractions of precipitates for flood basalt reacted at 100˚C in water equilibrated with 100 bar CO_2. Depth is the distance from the fracture inlet.

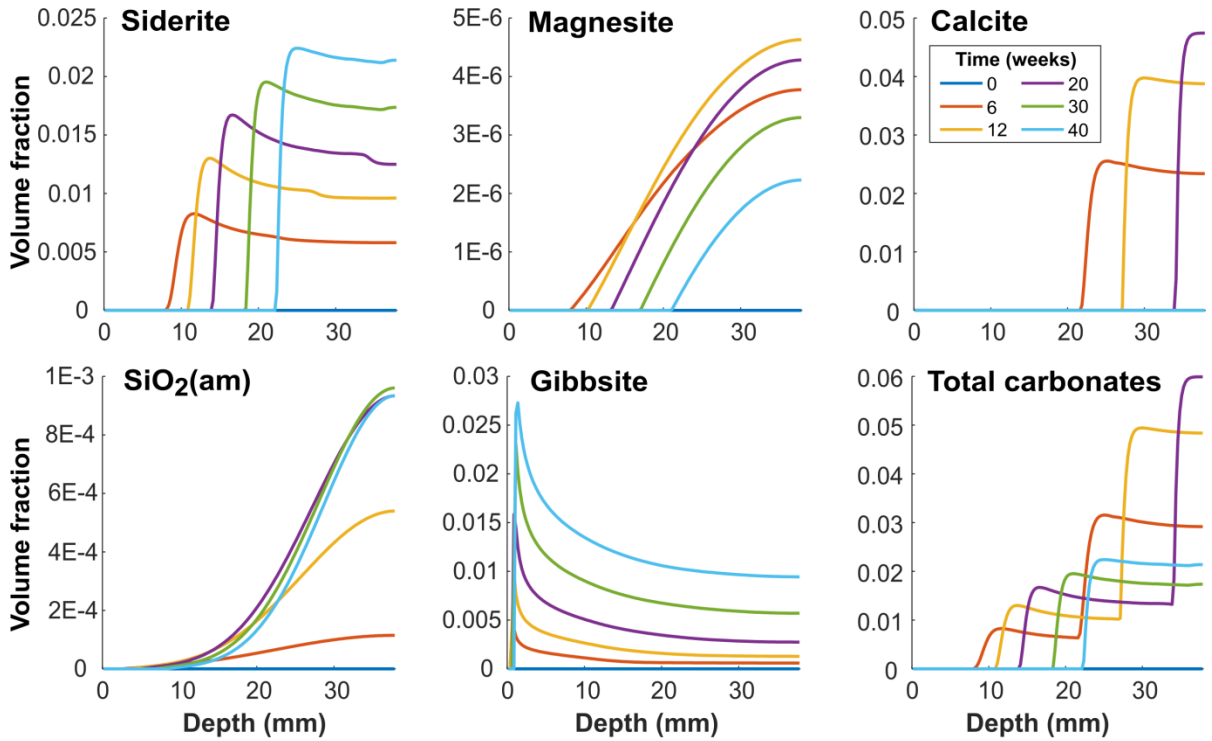

Figure S4.14 Predicted volume fractions of precipitates for serpentinized basalt reacted at 100˚C in water equilibrated with 100 bar CO_2. Depth is the distance from the fracture inlet.

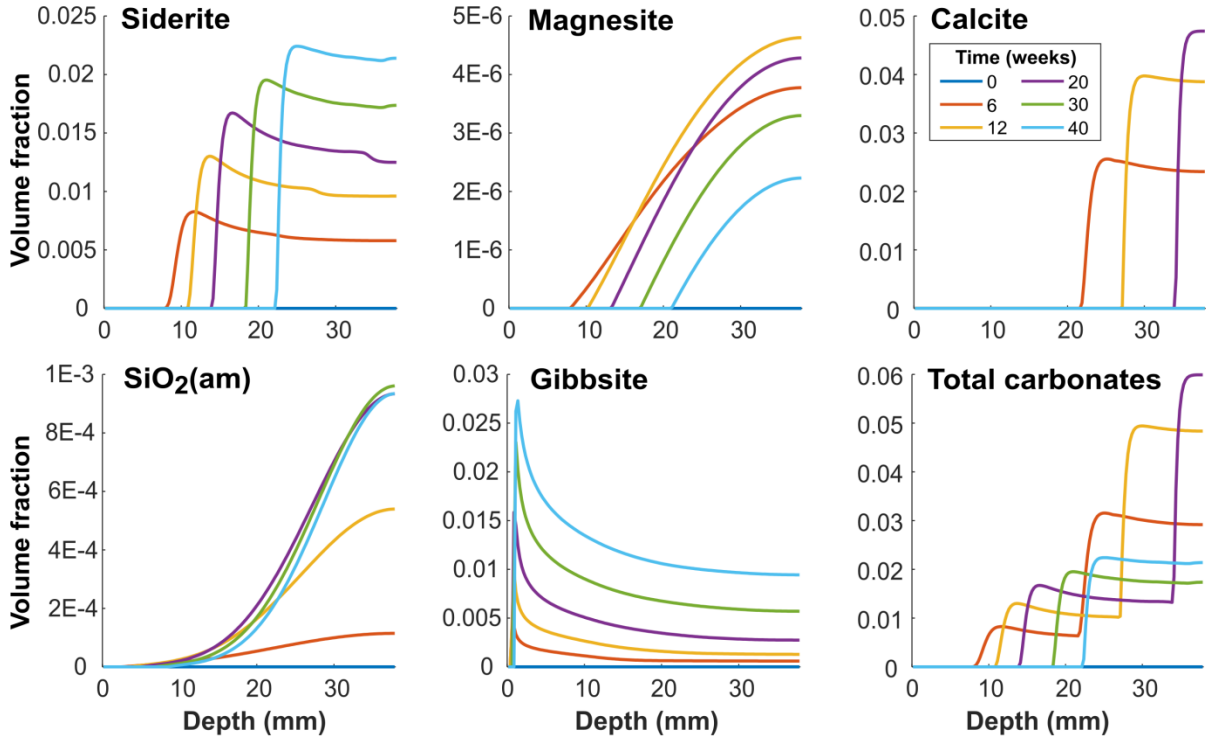

Figure S4.15 Predicted volume fractions of precipitates for flood basalt reacted at 150˚C in water equilibrated with 100 bar CO_2. Depth is the distance from the fracture inlet.

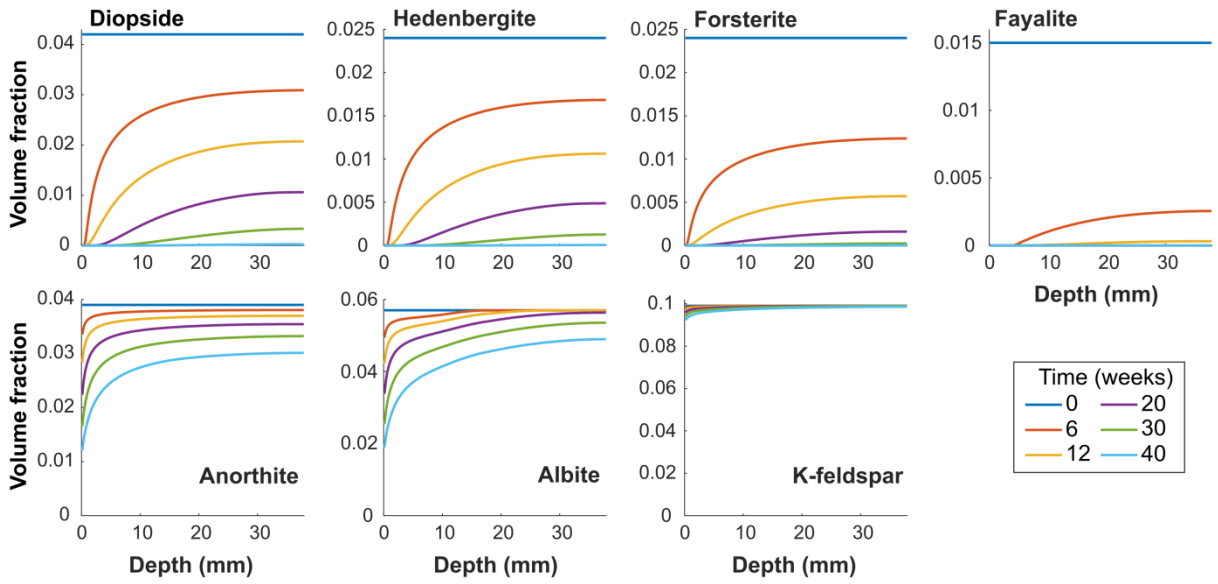

Figure S4.16 Predicted amounts of primary minerals in flood basalt during reaction at 100˚C. Amounts of the minerals decrease with time as they dissolve. Depth is the distance from the fracture inlet.

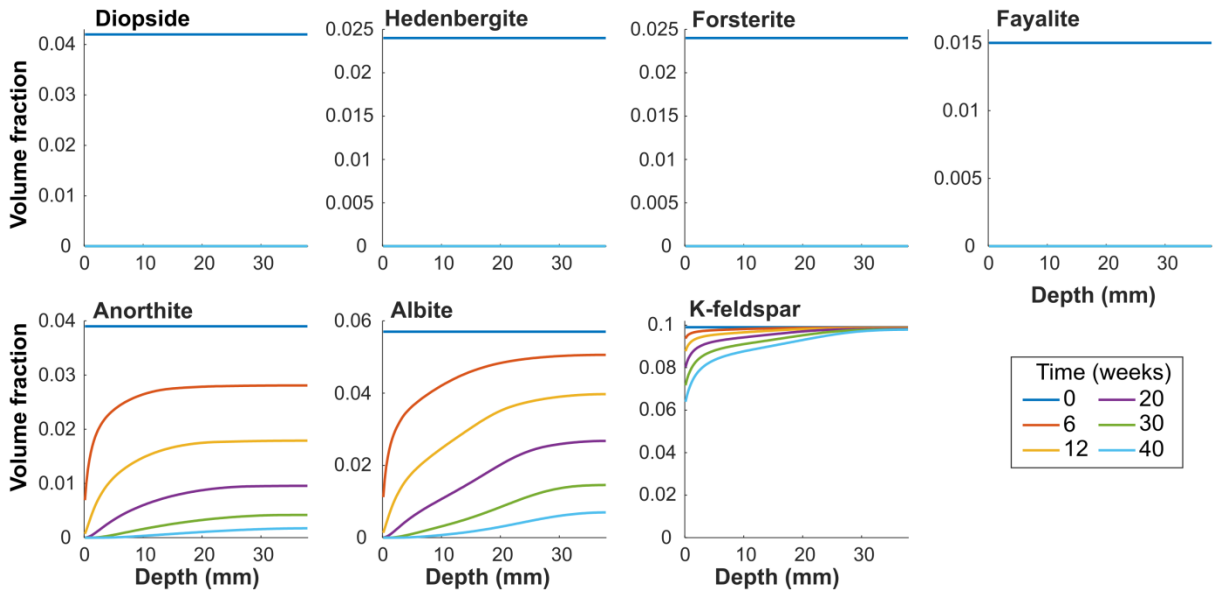

Figure S4.17 Predicted amounts of primary minerals in flood basalt during reaction at 150˚C. Amounts of the minerals decrease with time as they dissolve. Depth is the distance from the fracture inlet.

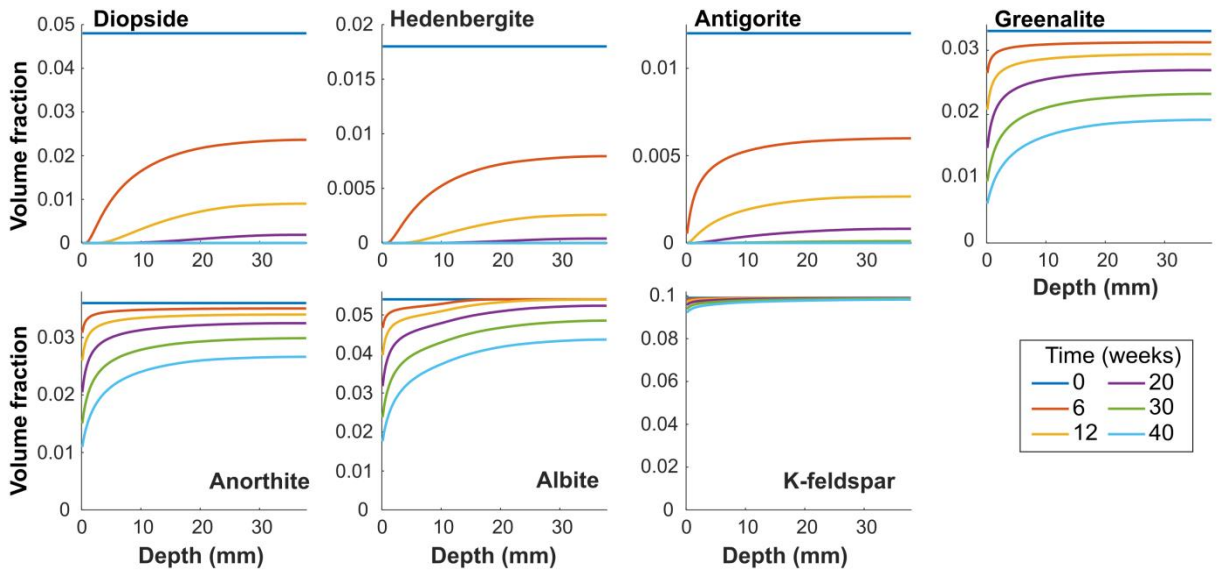

Figure S4.18 Predicted amounts of primary minerals in serpentinized basalt during reaction at 100˚C. Amounts of the minerals decrease with time as they dissolve. Depth is the distance from the fracture inlet.

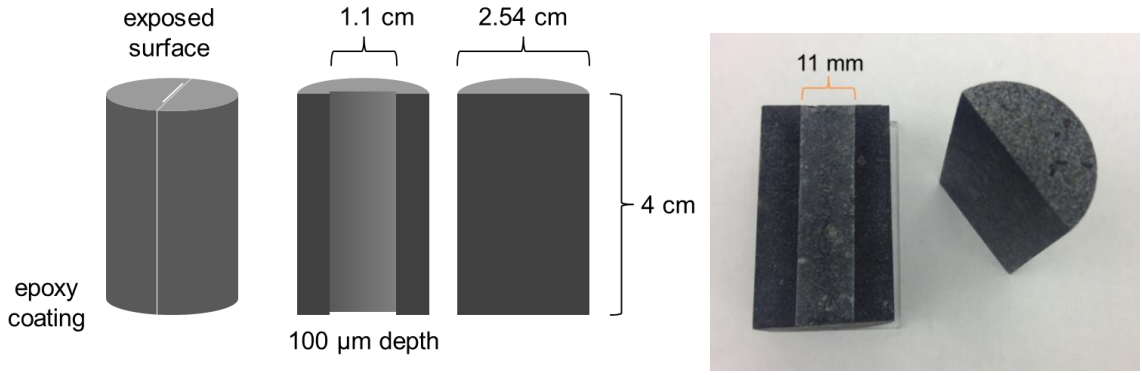

Figure S4.19 Milling pattern

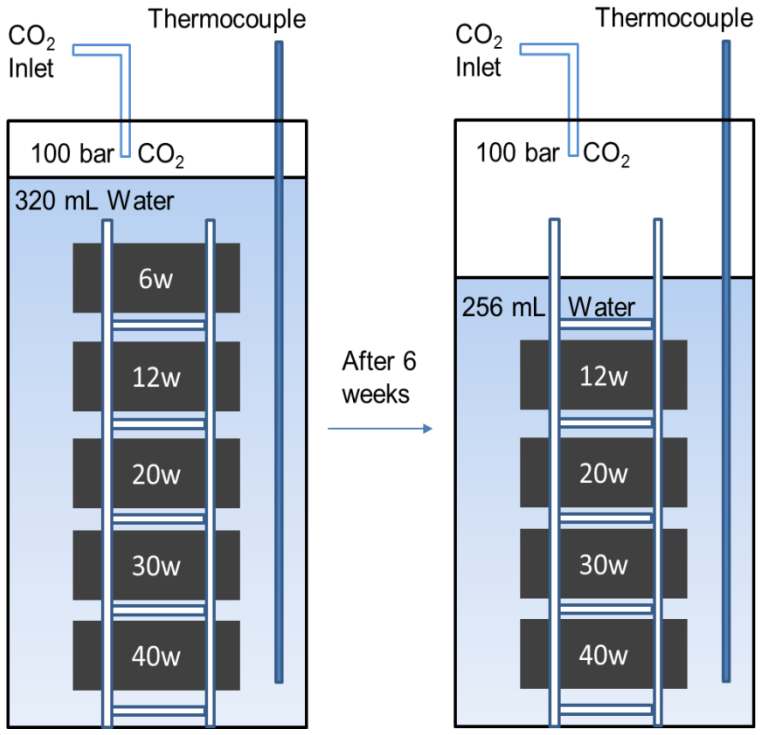

Figure S4.20 Schematic diagram of experiment set up

Precipitate segmentation

Precipitates observed in the 40-week cores from each set of batch experiments were segmented from post-reaction CT scans to estimate precipitate volumes in the milled fractures. The reconstructed cores were exported as stacks of image slices perpendicular to the fractures. As the cores were not perfectly vertical during the scans, fractures were first aligned in ImageJ [95] using the StackReg plugin [96]. The fractures were then isolated and the image stack resliced, resulting in a series of images parallel to the fracture from the milled surface to the smooth surface. Because each core had only 3-6 fracture images depending on the voxel resolution of the scan and the contrast often differed significantly between the fracture surfaces and interior, each image was segmented separately for optimal resolution. Images were pre-processed in ImageJ to remove regions of epoxy that were not considered as available fracture volume for precipitation. Thresholding was performed in Ilastik, an interactive software that uses specified feature sizes and descriptors (e.g. intensity or texture) to classify pixels and then segments classes by minimizing the cut between foreground and background seeds. Manual seeding trains the software to identify user-defined pixel classes, which are then segmented by optimizing the minimal cut between foreground and background seeds based on weighted combinations of intensity and edge filters [82]. Here, pixels were classified as precipitate or fracture, and resulting binary images were exported for quantification. Precipitate volumes and fractions relative to the total fracture volume were then calculated in Matlab for each core based on the voxel resolutions of the scans. To compare spatial distributions of the segmentations with the point counting results along the fracture surfaces, precipitate volumes were also calculated over 5-mm intervals from the fracture inlet to the sealed end. It should be noted that this approach failed to capture the precipitates at the base of the FB-150C core due to inconsistent contrast, but overall it

provides a reasonable estimate of precipitate volumes within the data quality and resolution of the CT images.

1D reactive transport modeling

To understand how geochemical gradients drive precipitation patterns observed inside the fractures, 1D reactive transport models were developed in CrunchTope.[83] The geochemical gradients are generated by the pH-dependent dissolution of minerals in the basalt and the diffusion of inorganic carbon into the fracture together with the diffusion of solutes out of the fracture. Because the code is designed for porous media, the system consisting of an open fracture surrounded by reactive mineral was modeled as an equivalent porous medium with dimensions and water:rock ratios calculated from the geometry in Figure S19. Based on observations from pre- and post-reaction CT scans of these core samples, it was assumed that the reactive fluid could penetrate, or interact with, the surrounding rock to a depth of 20 μm on all sides of the fracture over the 40-week experiments. This corresponded to an initial porosity of 30% (i.e. mineral fraction of 70%) and water:rock ratio of 2.5. Although transport is only considered in one dimension along the length of the fracture, which was discretized into 152 grid cells (0.25 mm in length), each cell was also assigned a width (11.04 mm) and height (0.14 mm) to capture the total volume of rock and fluid in the model domain illustrated in Figure S19.

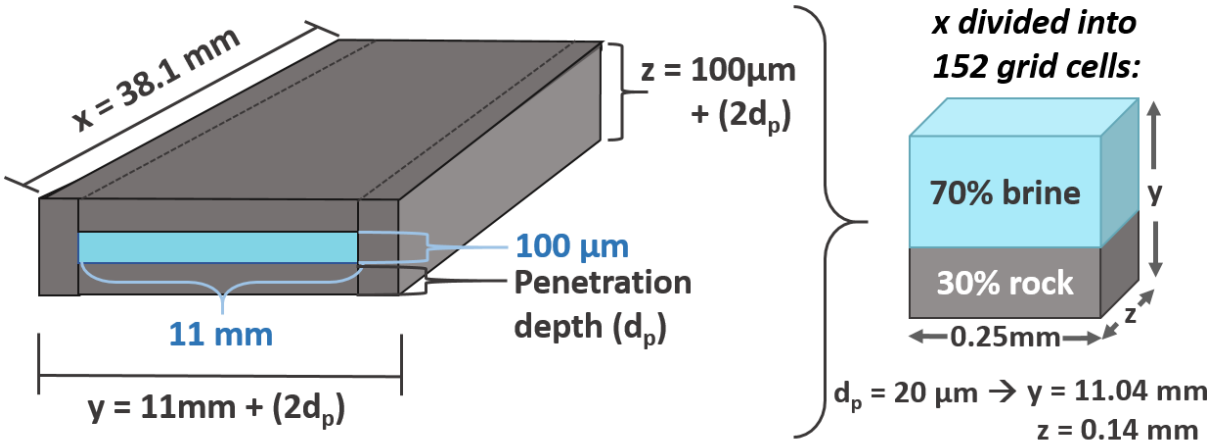

Figure S4.21 Conceptual schematic of modeled domain, where the open fracture surrounded by reactive basalt surfaces is converted to an equivalent volume of porous medium discretized into 152 0.25-mm grid cells along the x-dimension parallel to the fracture surface.

To match experimental conditions in the batch reactors, a constant flux (Dirichlet) boundary, consisting of pure water equilibrated with CO_2 at 100 bar and the experimental temperature (100˚C or 150˚C), was imposed at the inlet. CO_2 fugacity was calculated directly in the code.[54] While cations are allowed to diffuse back through the inlet as concentration gradients develop, the models do not allow for feedback between the fracture and bulk solution. Results for models where the inlet composition was set to that of the actual bulk solution measured at experimental sampling points differed negligibly from those where the inlet boundary was maintained as pure water, indicating the influence of the bulk solution was insignificant relative to cation accumulation within the fracture. A no-flux boundary was set at the bottom of the fracture to mimic the sealed end of the core. Diffusion was the only transport mechanism considered with fixed diffusion coefficients of $7.5*10^{-9}$ m^2/s (100˚C) or $12.33*10^{-9}$ m^2/s (150˚C) applied for all species.[84]

The primary mineralogy of the serpentinized and flood basalt samples was set based on previous calibrations, whereby effluent data from flow-through experiments using the same cores and experimental conditions were matched to model outputs by adjusting mineral volume fractions within a few percent of wavelength-dispersive spectroscopy (WDS)-derived compositions. Because the effluent chemistry data used as a benchmark in the previous calibration are sensitive to heterogeneities along fracture pathways and inter-sample variation, some mineral abundances were adjusted from the previously calibrated values to be more consistent with the WDS analysis. For the flood basalt, 36% of the pyroxene, which was all designated as diopside in prior models, was set to hedenbergite to account for the appreciable Fe content of the pyroxene ($Ca_{0.63}Fe_{0.48}Mg_{0.83}Ti_{0.03}Al_{0.09}Si_{1.92}O_6$). Additionally, a higher percentage of forsterite was included to match the Mg:Fe composition of the olivine ($Mg_{1.21}Fe_{0.78}Ca_{0.01}SiO_4$), and the 1% of serpentine present in the samples was neglected. For the serpentinized basalt, olivine (1%) was neglected while serpentine was modeled with an 11:4 ratio of greenalite:antigorite to match the Fe:Mg ratio in the serpentine of the actual samples ($Mg_{0.6}Al_{0.27}Ca_{0.11}Mn_{0.05}Fe_{1.82}Si_3O_9H_x$). Primary mineral specific surface area (SSA) values for each core sample were applied directly from the previous calibration, where primary mineral SSAs were fine-tuned to simulate experimental effluent data. The FB values, which had been calibrated to a flow-through experiment at 100˚C, were also used in the 150˚C model given the lack of an experimental benchmark for conducting a separate calibration.

Based on experimental observations, calcite, magnesite, siderite, amorphous silica, and gibbsite were included as potential precipitates. All secondary minerals are assigned an initial volume fraction of 0 and threshold mineral volume fraction of 10^{-6}. The bulk surface area of secondary minerals is calculated from this threshold volume fraction until it is exceeded, at

which point precipitation begins and the volume fraction is updated at each time step according to user-defined SSAs. Here, literature-reported BET specific surface areas were selected for all secondary minerals. Porosity is updated each time step in the code based on changes in primary and secondary mineral volume fractions. Initial primary and secondary mineral volume fractions and SSAs selected for each basalt core are summarized in Table S4.3.

Table S4.3 Mineral abundances and specific surface areas for reactive transport modeling.

Mineral	Flood basalt		Serpentinized basalt	
	Initial volume fraction (%)	Specific surface area (m^2/g)	Initial volume fraction	Specific surface area (m^2/g)
Primary minerals				
Diopside	16	0.0034	14	0.0017
Hedenbergite	6	0.0034	8	0.0017
Albite	18	0.0225	13	0.0225
Anorthite	12	0.0225	19	0.0225
Antigorite	4	0.18	0	0.18
Greenalite	11	0.18	0	0.18
Forsterite	0	--	8	0.009
Fayalite	0	--	5	0.0018
K-feldspar	33	0.019	33	0.019
Secondary Minerals				
Calcite	--	0.037[85]	--	0.037[85]
Magnesite	--	0.0662[85]	--	0.0662[85]
Siderite	--	0.105[86]	--	0.105[86]
SiO_2(am)	--	0.0225[87]	--	0.0225[87]
Gibbsite	--	19[88]	--	19[88]

Mineral dissolution and precipitation are assumed to proceed reversibly according to the transition state theory. In the absence of adequate precipitation kinetic data, literature-reported dissolution rates are applied to both processes. To maintain flexibility, reaction rates are calculated directly in the code for a given temperature using the Arrhenius relationship:

$$k = k_{25} \exp\left[\frac{-E_a}{R}\left(\frac{1}{T} - \frac{1}{298.15}\right)\right]$$

The reaction rate at 25˚C (k_{25}) and activation energy (E_a) for each mineral were taken from literature where available (Table S4). Parallel rate laws are used to account for reaction pH

dependence, where constants for the exponential dependence of a rate on H^+ (acid mechanism) or OH^- (basic mechanism) were also taken from literature. Due to a lack of data for Fe-rich serpentine, greenalite was assigned the same kinetic parameters as antigorite. Other than fayalite, where k_{25} was set to that of forsterite in our previous study to match effluent Fe data, reported reaction rates were applied directly.

Table S4.4 Mineral kinetic inputs for reactive transport modeling.

Mineral	Acid mechanism			Neutral mechanism		Basic mechanism		
	log k_{25} (mol/m^2/s)	**E_a (kcal/mol)**	**n^{H+}**	**log k_{25} (mol/m^2/s)**	**E_a (kcal/mol)**	**log k_{25} (mol/m^2/s)**	**E_a (kcal/mol)**	**n^{OH-}**
Diopside	-6.36[89]	22.97[89]	0.71[89]	-11.11[89]	9.70[89]	--	--	--
Hedenbergite	-6.36	22.97	0.71	-11.11	9.70	--	--	--
Albite	-8.86[89]	16.2[89]	0.50[89]	-12[89]	15.9[89]	--	--	--
Anorthite	-8.86[89]	16.2[89]	0.50[89]	-12[89]	15.9[89]	--	--	--
Antigorite	-10.01[90]	16.73[90]	0.45[90]	-12.08[91]	13.53[91]	--	--	--
Greenalite	-10.01	16.73	0.45	-12.08	13.53	--	--	--
Forsterite	-6.85[89]	16.06[89]	0.47[89]	-10.64[89]	18.88[89]	--	--	--
Fayalite	-6.85	22.56[89]	0.47[89]	-12.8[89]	22.56[89]	--	--	--
K-feldspar	-9.45[92]	12.36[89]	0.50[89]	-12.41[89]	9.08[89]	-21.2[89]	22.49[89]	-0.823[89]
Calcite	-0.3[89]	3.44[89]	1.0[89]	-5.81[89]	5.62[89]	--	--	--
Magnesite	-6.38[89]	3.44[89]	1.0[89]	-9.34[89]	5.62[89]	--	--	--
Siderite	-3.74[93]	13.38[93]	0.90[93]	-8.90[92]	15.0[92]	--	--	--
SiO_2(am)	--	--	--	-9.7[94]	18.88[94]	--	--	--
Gibbsite	-7.65[89]	11.35[89]	0.992[89]	-11.5[89]	14.63[89]	-16.65[89]	19.14[89]	-0.784[89]

Chapter 5. Carbon Sequestration in Grand Ronde Basalt

Abstract

Basalt is a promising host rock for geologic carbon sequestration due to its high mineral capacity. Pilot CO_2 injection into basalt reservoirs have been conducted in Wallula, Washington. In this study, we investigated carbonate mineral formation in fractured porous Grand Ronde basalt, which is similar to the formation into which the pilot-scale project injected CO_2. The experiment was done with artificial dead-end fractured basalt cores reacting in water equilibrated with 100 bar CO_2 at 100˚C for up to 40 weeks. Predominant aragonite and a few calcite precipitates with trace amounts of Mg, Fe and Mn were observed after 20 and 40 weeks of reaction. X-ray computed tomography showed that the calcium carbonate formed mainly along the deeper part of the microfracture from the fracture inlet connecting the bulk solution and in pores close to the fracture. Appreciable amounts of precipitates were also found in distant pores from the fracture in the inner core body. The carbonate minerals in the microfracture occupied 5.4 % and 12.6 % of the fracture space after 20 and 40 weeks of reaction, respectively. The formation of calcium carbonate did not block transport pathways and cease the reaction within the experimental time. The carbonation rate was 1.29 ± 0.08 kg CO_2/m^3 basalt·year based on experimental results. At this rate it would take 36.5 years to fill the initial available pores in Grand Ronde basalt with carbonate minerals, and at that time the basalt would have sequestered 47 kg CO_2 per cubic meter or 22.5 kg CO_2 per ton Grand Ronde basalt.

5.1 Introduction

Geologic carbon sequestration is an effective way to mitigate environmental problems brought by excessive anthropogenic CO_2 emissions to the atmosphere[3, 35]. It involves injecting supercritical CO_2 into deep geologic formations such as sandstone, saline aquifers and basalt. Fe- and Mg-rich (mafic) basalt has large mineral trapping capacity to convert CO_2 into solid carbonate minerals[12, 97]. CO_2 mineral trapping in basalt reservoirs can occur very rapidly in a few years as compared to hundreds or thousands of years in sandstone[79]. In the pilot-scale CO_2 injection into basalt in Iceland, 95 % CO_2 mineralized to calcite within 2 years[19]. In another pilot injection into basalt formation in Washington State, mineralization of injected CO_2 to ankerite nodules was observed in 2-year post-injection monitoring[22].

The dissolution of basalt provides divalent cations including Ca^{2+}, Mg^{2+} and Fe^{2+}, which react with dissolved CO_2 to form carbonate minerals. The divalent cation sources are silicate minerals in basalt such as olivine, pyroxene and plagioclase. The carbonation reaction with silicate minerals in basalt can be generalized in the following equations[14]:

$$Mg_2SiO_4 \text{ (olivine)} + 2CO_2 = 2MgCO_3 \text{ (magnesite)} + SiO_2 \qquad \text{Eq. 5.1}$$

$$CaAl_2Si_2O_8 \text{ (anorthite)} + CO_2 + 2H_2O = CaCO_3 \text{ (calcite)} + Al_2Si_2O_5(OH)_4 \text{ (kaolinite)} \qquad \text{Eq. 5.2}$$

Carbonation reactions mostly happen in pores and fractures where transport is controlled by diffusion [55, 63]. The diffusion-limited microfractures and pores allow cations to accumulate and reach supersaturation status with respect to carbonate minerals in CO_2-rich solution. Previous studies investigated carbonation on the surfaces of basalt grains in a bulk solution.[25, 26, 57, 59, 71] Experiments with basalt rock cores in flow-through system focus on dissolution [98] and permeability change [99]. Our previous work with fractured flood basalt cores and serpentinized

basalt cores in static batch system and flow-through system discussed siderite mineral formation as well as basalt dissolution and fracture evolution (see Chapter 4).

In this study, we investigated carbonate mineral formation in porous Grand Ronde basalt cores with an artificial dead-end microfracture reacted in water equilibrated with 100 bar CO_2 in 100˚C for up to 40 weeks. The objective of this work is to identify the carbonate formation type, determine the location of carbonate minerals and quantify precipitate volume in Grand Ronde basalt. Through the analysis, the effect of diffusive transport on carbonation was discussed.

5.2 Materials and Methods

5.2.1 Fractured Grand Ronde basalt cores

A large core sample from of the Grand Ronde Formation (1022.3~1022.6 m depth), which is similar to the formation into which CO_2 was injected near Wallula, WA was obtained from the DC-6 well in the Hanford archives at Pacific Northwest National Laboratory. The basalt core is porous and contains many mm- to cm-scale vesicles (Figure S5.1). The pores are residual air bubbles during basalt formation. Most pores are not connected. Mineral composition of the sample is listed in Table 5.1. More information can be found in a published report.[64]

Table 5.1 Grand Ronde basalt sample composition

Mineral	Composition	Formula
Plagioclase	58%	$Ca_{0.51}Na_{0.46}K_{0.03}Al_{1.47}Si_{2.49}O_8$
Pyroxene	14%	$Mg_{0.72}Fe_{0.59}Ca_{0.60}Si_{1.90}Al_{0.12}O_6$
Ilmenite	3%	$FeTiO_3$
Silica-rich matrix and glass	25 %	almost no divalent cations

The core was drilled and cut to make multiple smaller Grand Ronde basalt (GB) cores with 25.4 mm diameter and 40 mm length. Each core was cut to half cylinders. The surface of one cylinder was milled with a 100 μm deep and 11 mm wide straight groove pattern (Figure S5.2) using a milling machine (Roland Model MDX-40a) with a 0.5 mm diamond bur. The groove depth was determined by comparing the z-value of the spots on the groove and the spots on the closest polished surface in an optical microscope (ZEISS, Observer Z1). The two half cylinders were then attached together and coated with epoxy (MasterBond EP42HT-2) on the side and bottom surfaces, only exposing the top surface with the fracture inlet.

5.2.2 Static batch experiment

Three of the epoxy-coated fractured basalt cores were put in a PTFE sample shelf, which sat in a PTFE liner inside of a 600 mL stainless steel high pressure vessel (Parr Instrument) (Figure S5.3). A volume of 192 mL (64 mL per core) of deionized water was added to fully immerse the cores. The reactor was heated to 100˚C by heating tape with heat controller (Omega Benchtop Controller, CSi32 Series). The headspace was pressurized to 100 bar CO_2 and maintained during the experiment by a syringe pump (500D, Teledyne Isco). The cores were collected one by one after reacting for 6, 20 and 40 weeks. At each sampling time 64 mL solution was removed after each core was collected to maintain the same solid to water ratio in the reactor. Liquid samples were taken from the removed solution and filtered by 0.2 μm filters. The collected core samples were air-dried. The process of cooling and depressurizing for sample collection and restarting the batch was completed within 5 hours. Before being heated and pressurized, the vessel was flushed with 10 bar CO_2 for three times to remove residual O_2.

5.2.3 Analytical Methods

The three basalt cores were scanned by X-ray computed tomography before (Scanco uCT 40) and after reaction (Nikon Metrology XTH225, Zeiss Xradia Versa 520). The voxel resolution of the CT images was 22.5 μm for the 6-week and 20-week samples and 15.5 μm for the 40-week sample. The precipitate volume was assessed by CT segmentation using ORS Visual and ImageJ. Pore area percentage on each CT slice was calculated in ImageJ using Zen threshold. Then each core was cut open by the fracture sides. Optical microscopy (LEICA, DFC295) was used to detect precipitates along the groove surface. The precipitates were then scanned via Raman spectroscopy (HoloLab Series 5000 Laser Raman Microprobe, Kaiser Optical) with a 532 nm laser and a 50 power objective that probes a 2-3 μm diameter area. The Raman spectra were compared with different carbonate mineral standards from the RRUFF database. The precipitate morphology and elemental composition were examined by scanning electron microscopy and energy dispersive X-ray spectroscopy (SEM-EDS, FEI Nova 230). A thin section of the 20-week sample was prepared and the chemical composition of the precipitates was analyzed by an electron microprobe (JEOL JXA-8200) with wavelength-dispersive spectrometry (WDS). Aqueous samples were analyzed by inductively coupled plasma mass spectrometry (Perkin Elmer, Elan DRC II) and ion chromatography (Theromo Scientific, DIONEX ICS-1600).

5.3 Results and Discussion

5.3.1 Identification of precipitates

The precipitates are calcium carbonate. Most of the precipitates formed in the Grand Ronde basalt had a needle or star shape (Figure S5.4, Figure S5.5). The size of the precipitates was in the mm-scale. The precipitates were crystal clear. Raman spectra of the large needle and star shape precipitate crystals formed in the 20-week basalt and the 40-week basalt match well with an aragonite standard from the RRUFF database (Figure 5.1). The SEM-EDX spectra confirmed that the rod-shaped precipitates are calcium carbonate (Figure 5.2a). Some μm-scale hexagonal shape calcium carbonate minerals (Figure S5.6) with trace amounts of Fe, Mg and Mn were also observed (Figure 5.2b Figure S5.7). This diamond precipitate was identified as calcite by Raman spectroscopy (Figure 5.1). Some carbonate minerals were covered by Si-rich secondary precipitates, which might be amorphous silica (Figure S5.7). Precipitates looking like small round white balls were found on the part close to the fracture inlet of the 20-week sample, which might be amorphous silica (Figure S5.4d).

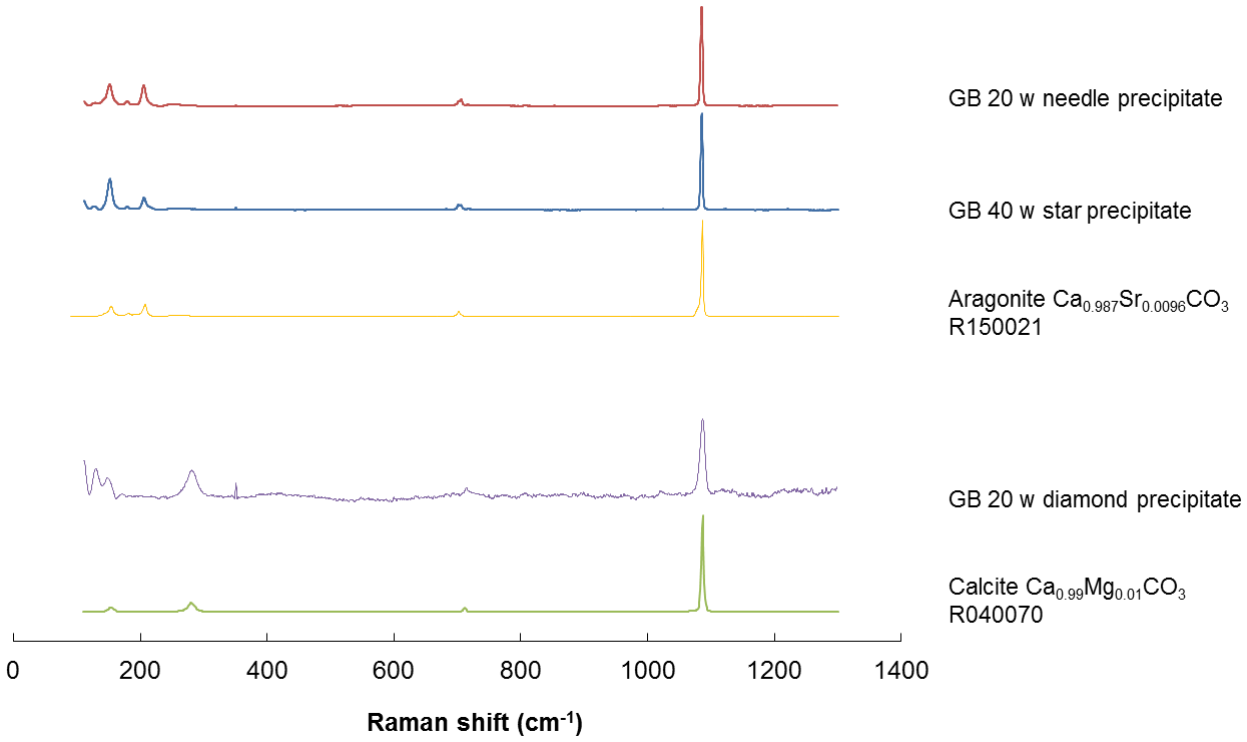

Figure 5.1 Raman spectra of the rod and star shape precipitates formed in Grand Ronde basalt with different carbonate mineral standards from the RRUFF database.

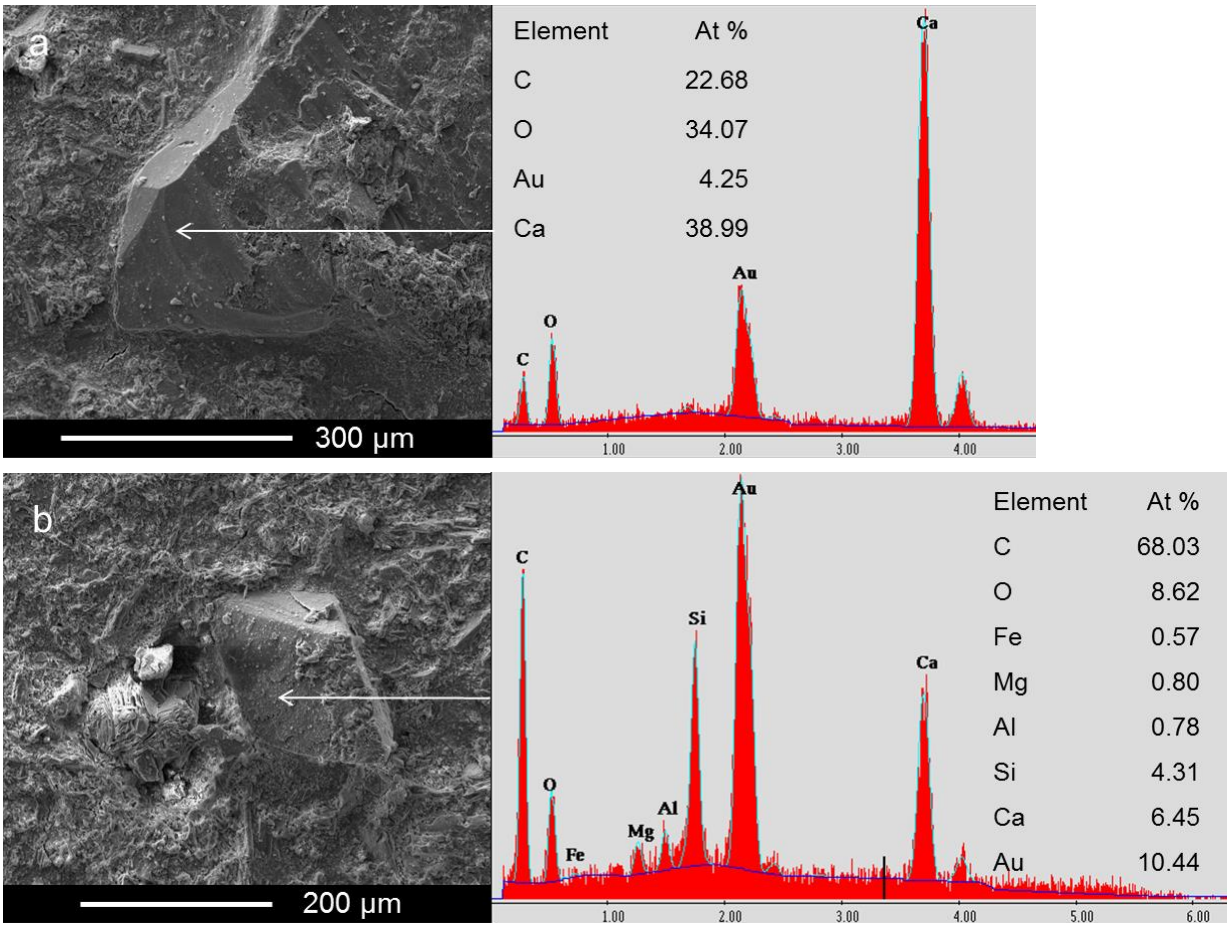

Figure 5.2 a) SEM-EDX on a rod-shape precipitate on the surface in 20-week core with gold coating b) SEM-EDX on diamond-shape precipitates in 20-week core with gold coating

Aragonite and calcite are polymorphs with the same chemical composition ($CaCO_3$) but different crystal structures. Aragonite has an orthorhombic structure, in which cations are in 9-fold coordination to carbonate oxygens [100]. Calcite has a hexagonal structure, in which the cation is in 6-fold coordination with oxygen [101] Cations such as Sr^{2+} and Ba^{2+} that are larger than Ca^{2+} are common substitutes in aragonite, while smaller cations such as Mg^{2+} are found more frequently in calcite [102]. This explains why the aragonite was almost pure calcium carbonate (Figure S5.6) while the calcite contains trace amounts of Fe and Mg (Figure 5.2).

The majority of the precipitates were aragonite and there were a few calcite precipitates. The formation preference of aragonite and calcite is affected by both temperature and the Mg/Ca ratio in the solution [102]. Natural observations indicate that calcite is more likely to form in cold water than aragonite [103]. Previous study shows calcite tends to form in lower Mg:Ca ratio than aragonite [103]. At 10˚C, Mg:Ca ratio in the solution needs to exceed 4 in order to form aragonite [103]. However, when temperature is above 30˚C, aragonite can precipitate at much lower Mg:Ca ratio (~0.5). In some experiments, calcite formed initially and then aragonite began to nucleate and grow because the solution Mg:Ca ratio increased as precipitation proceeded [102].

Alhough the Grand Ronde basalt is similar to the formation into which CO_2 is injected in the pilot-scale project in Wallula, WA, the carbonation products are calcium carbonate with predominant aragonite in our study, while ankerite $Ca(Fe,Mg,Mn)(CO_3)_2$ was observed in the pilot-scale field study[22]. In the field injection, the temperature was about 36~44˚C and pressure was ~77 bar, which were different with this study[22]. Detected Ca^{2+} and Mg^{2+} concentrations are several times higher after equilibrium[22]. Other studies also showed that different carbonate products could form in different conditions in basalt. Experiments using basaltic glass showed that Ca-Mg-Fe carbonates formed at < 100˚C but at > 150˚C calcite became the dominant carbonate type [26]. Our previous study with flood basalt cores also showed that siderite formed at 100˚C and Fe-Mg-Ca carbonate formed at 150˚C (Chapter 4).

Bulk solution chemistry provides information on basalt dissolution. The Grand Ronde basalt is rich in Ca, Mg and Fe. Ca^{2+} has the largest concentration in the bulk solution, followed by Mg^{2+}. Very limited Fe^{2+} and Mn^{2+} were detected (Figure S5.8). It is possible that some of the dissolved Fe^{2+} reacted with residual O_2 in the system to form iron oxides. The Mg:Ca ratio was 0.6, favorable for aragonite to form at 100˚C.. There was a lot of Na^+ (50-70 mmol/L) in the bulk

solution as well as appreciable amounts of Cl^- and SO_4^{2-}, which were probably from evaporated residual brine left inside the porous basalt. The calculated pH in the bulk solution was 5.1~5.3 (Figure S5.9), higher than the bulk solution pH of 4 in our previous batch experiments with flood basalt and serpentinized basalt cores. The pH and the saturation indices (Figure S5.10) based on the measured concentrations and calculated dissolved CO_2 [54] were calculated in SpecE8 in Geochemists' Workbench. Saturation indices changed over time. Multiple carbonate minerals including dolomite, rhodochronsite, calcite, magnesite, aragonite, siderite were supersaturated. However, the majority of the precipitates observed in the Grand Ronde basalt core were aragonite. The formation of carbonate minerals not only depends on supersaturation status but also on the kinetics of nucleating and growing a particular precipitate. For example, dolomite is often supersaturated in a simple reaction path calculations but it is rarely observed to precipitate in a variety of experimental and natural conditions [102].

5.3.2 Location of precipitates

Calcium carbonate minerals mostly formed along the fracture although the entire Grand basalt core was porous (Figure 5.3, Figure S 5.11). The fracture area was about 0.2 % of the core cross section on each CT image slice. The pore area percentage on each cross section slice along the fracture in the samples iss shown in Figure 5.4. Locations with several large pores have pore area percentage as high as 10 % (4~10 mm in GB 6 w core). The lowest pore area percentage was about 1 % (0~10 mm in GB 40 w core), indicating that the artificial fracture size had very little contribution to the overall basalt core porosity. However, the fracture was the main channel that was connected to the bulk solution. Diffusive transport and chemical reactions of divalent cations and dissolved CO_2 primarily took place along the fracture. Most visible pores in the

basalt were not connected. The lack of transport pathways largely inhibited the transport of solutes from the fracture into the inner basalt body. Some aragonite minerals were observed in the pores that were directly connected to the fracture (Figures S5.4b, S5.5b, S5.5d, S5.11, and S5.12). After long reaction times, carbonate precipitates were also found in distant pores that had no obvious connection with the fracture (Figure 5.3, Figure S5.13). This observation indicates that dissolved CO_2 can migrate into the inner porous Grand Ronde basalt body and that carbonation reactions can happen there if enough time is given.

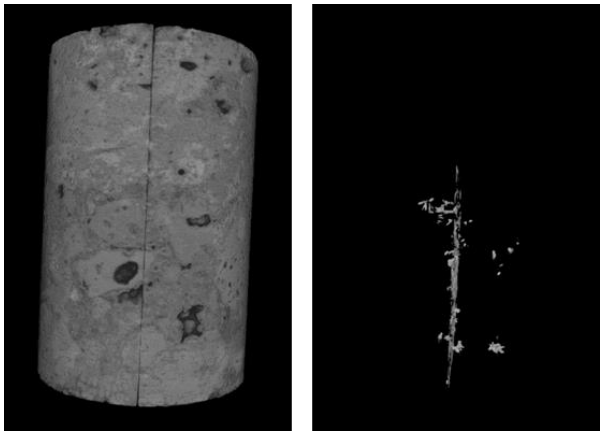

Figure 5.3 3D view of the 40-week core sample and segmented precipitates

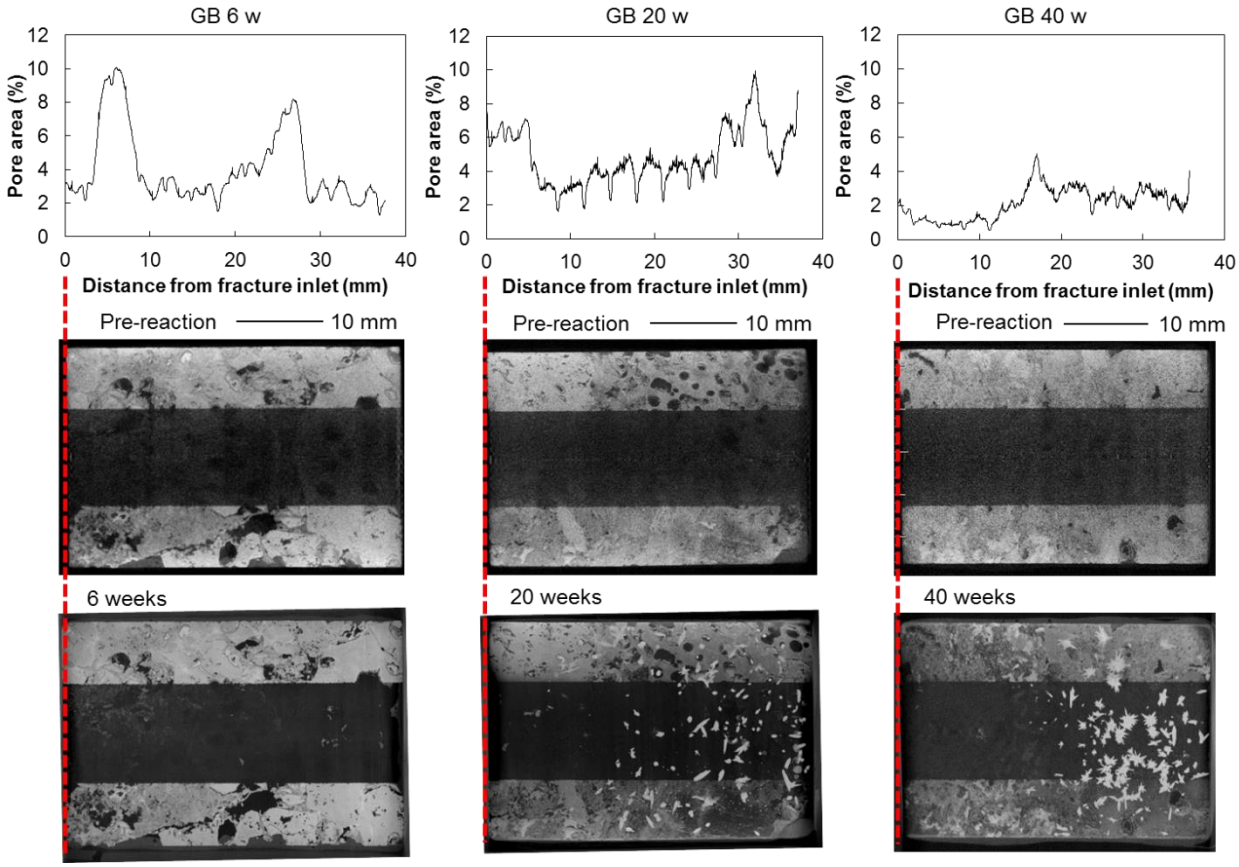

Figure 5.4 Pore area percentages on the core cross section and pre- and post-reaction CT images. The entire core porosity based on CT segmentation was 4.04 %, 4.83 % and 2.09 % for the pre-reaction 6-week, 20-week and 40-week core, respectively.

Although the basalt cores were porous, the presence of carbonate minerals depends more on the distance from the bulk solution than on the porosity of the surrounding rock (Figure 5.4). Very limited precipitates were observed after 6-week reaction. Lots of rod-like precipitates formed below 15 mm from the fracture inlet after 20 weeks of reaction. After 40 weeks of reaction, massive star-shape precipitates formed below similar depth (15 mm) along the fracture. The star-shape aragonite could be a result of multiple aragonite needles growing in different directions. The precipitates were large enough to fill across the 100 μm groove.

The spatially localized formation of calcium carbonate within the fracture was a result of opposing chemical gradients from the fracture inlet to the dead-end [27, 55, 63]. The bulk solution was rich in dissolved CO_2 but contained very limited cations for carbonation reaction. The fractured porous basalt core had no CO_2 inside initially. Dissolved CO_2 diffuses into the core mainly through the microfracture. As the reaction went on, dissolved cations were released out to the solution in the fracture and pores. Cations diffused out mainly from the fracture to the bulk solution. Localized cation concentrations along the fracture were determined by both diffusive transport and dissolution/precipitation reactions. Cation concentrations were lower near the fracture inlet which contacted the bulk solution. Regions away from the fracture inlet contained higher cation concentration and were more favorable for carbonate minerals to precipitate. Carbonate minerals were also found in further pores away from the fracture at bottom part of the core, indicating that dissolved CO_2 could diffuse from the fracture into the basalt body and could react with dissolved cations there. This observation also revealed that carbonation reactions not only happen on the fracture surface but also can occur in larger region of the porous basalt body.

5.3.3 Quantification of precipitates

The amounts of secondary precipitates were quantified by CT segmentation. The precipitate area per CT slice as a function of distance from the fracture inlet shows a clear spatial distribution trend (Figure 5.5a, Figure S5.14). The total precipitate volume can be calculated by multiplying the precipitate area in each slice with the voxel resolution and summing the numbers together (Figure 5.5b). The carbonate minerals that formed in the 100 μm fracture made up 32% and 39% of the total carbonate precipitate in the entire basalt core reacted for 20 weeks and 40 weeks, respectively. More than half carbonate minerals were also located in both sides of the

milled 100 µm groove and in adjacent pores. Not much precipitates were found in the side of the milled fracture in our previous study with flood basalt and serpentinized basalt cores. The flood basalt and serpentinized basalt had very little porosity beyond that of the milled fracture. The higher porosity of the Grand Ronde basalt probably facilitated further diffusion into the narrow zone and rock body, which led to carbonation reactions in these regions.

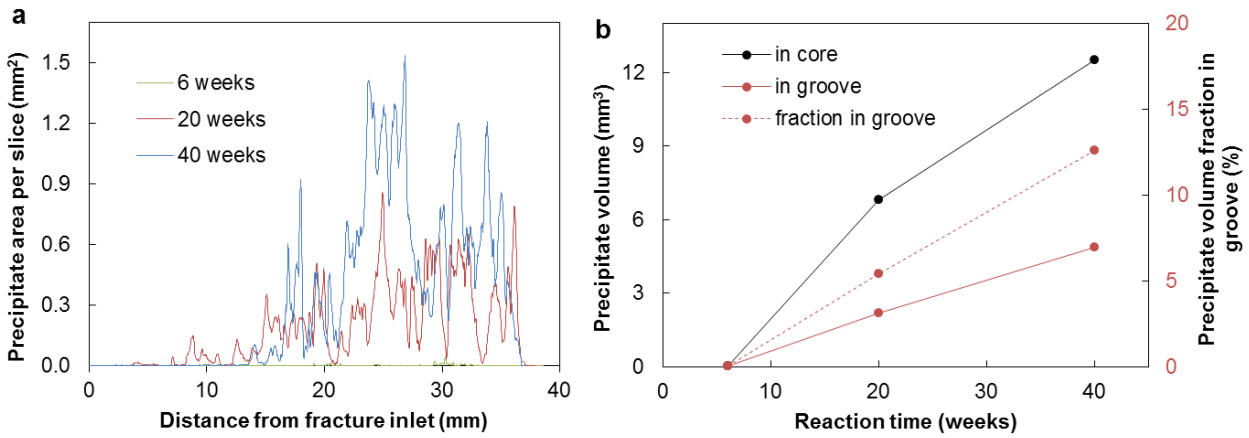

Figure 5.5 a) Precipitate area in each round cross section CT slice from segmentation. b) Total precipitate volume in the entire core, in the 100 µm fracture and precipitate volume fraction in the fracture.

Overall the carbonation products increased over time. The formation of calcium carbonate minerals did not block the transport pathways into deeper zone within the reaction time in this study. It was estimated that about 12.6 % of the 100 µm fracture volume was occupied with secondary precipitates (Figure 5.5b). There was still plenty of space for future reactions. As the reaction goes on, it is also expected that more carbonate minerals would form in distant pores far away from the microfracture.

The carbonation rate is almost constant during 6-40 weeks of reaction (Figure 5.5b). The first 6 weeks in which carbonates did not form may have been needed for the solution to become

sufficiently supersaturated to overcome the nucleation barrier. After nucleation occurred, carbonate growth was almost linear. The carbonation rate calculated using the 20-week and 40-week point is 1.29 ± 0.08 kg CO_2/m^3 basalt·year or 1001 ± 60 cm^3 $CaCO_3/m^3$ basalt·year, assuming that all precipitates are aragonite (2.93 g/cm^3). Each core had a mass of 35-36 g. The average volume was 17 cm^3. The average porosity of the three cores was 3.65 %. Assuming that in the Grand Ronde basalt that aragonite only precipitates in available pore space (i.e., an initial pore volume of 36526 cm^3/m^3 basalt) and that the carbonation rate remains constant, it would take 36.5 years to completely fill the pore space at 100˚C. It would take longer in lower reaction temperature. The mineral trapping capacity of the Grand Ronde basalt under this condition is 47 kg CO_2/m^3 basalt. Natural analogs have shown that up to 70 kg of CO_2 can be stored in a cubic meter of basaltic rock [104], suggesting that our estimation is reasonable. For the glauconitic sandstone aquifer, the total amount of CO_2 trapped in mineral phases after 100,000 years is about 17 kg/ m3 medium by simulation study[105]. For the Gulf Coast sediments, the mineral trapping could reach 90 kg CO_2/ m^3 medium after 100,000 years[105]. CO_2 mineral trapping is much more rapid in basalt and in sandstone reservoirs. In the Big Sky project, 1000 metric tons of CO_2 was injected into a 59 m Grand Ronde basalt formation layer (828-887 m depth)[22]. A volume of 21236 m^3 basalt would be required to mineralize all of the injected CO_2, which means that CO_2 needs to spread out to 11-m radius circle from the injection well into surrounding 59 m-thick basalt layer. The diffusion transport into basalt body may increase overall mineral trapping time.

5.3.4 Implications for carbon sequestration

Carbonate minerals can form very rapidly within weeks in basalt reservoirs. The formation of carbonate minerals is spatially distributed in zones of which the transport is

controlled by diffusion. In the porous Grand Ronde basalt, the formation of carbonate would not block the transport pathways and inhibit reactions into deeper zones within the 40 week experimental time of this study. The carbonation products were calcium carbonate, which is different from the field study. Laboratory studies such as this one often increase the temperature to accelerate the reaction rate in order to observe precipitates at shorter times. While in the field, the temperature can be much lower (36-44˚C for the Big Sky project in Wallula). Future experiments could be performed at temperature and pressure conditions that are more directly comparable to those of the field study.

Acknowledgements

We thank professor Jill Pasteris for her help in Raman spectroscopy. We thank Dr. Hélène Couvy for helping to prepare core samples. We thank Daniel Leib and Professor James Fitzpatrick for their help in X-ray Computed Tomography. This work was funded by the U.S. Department of Energy (DE-FE0023382).

Supporting Information

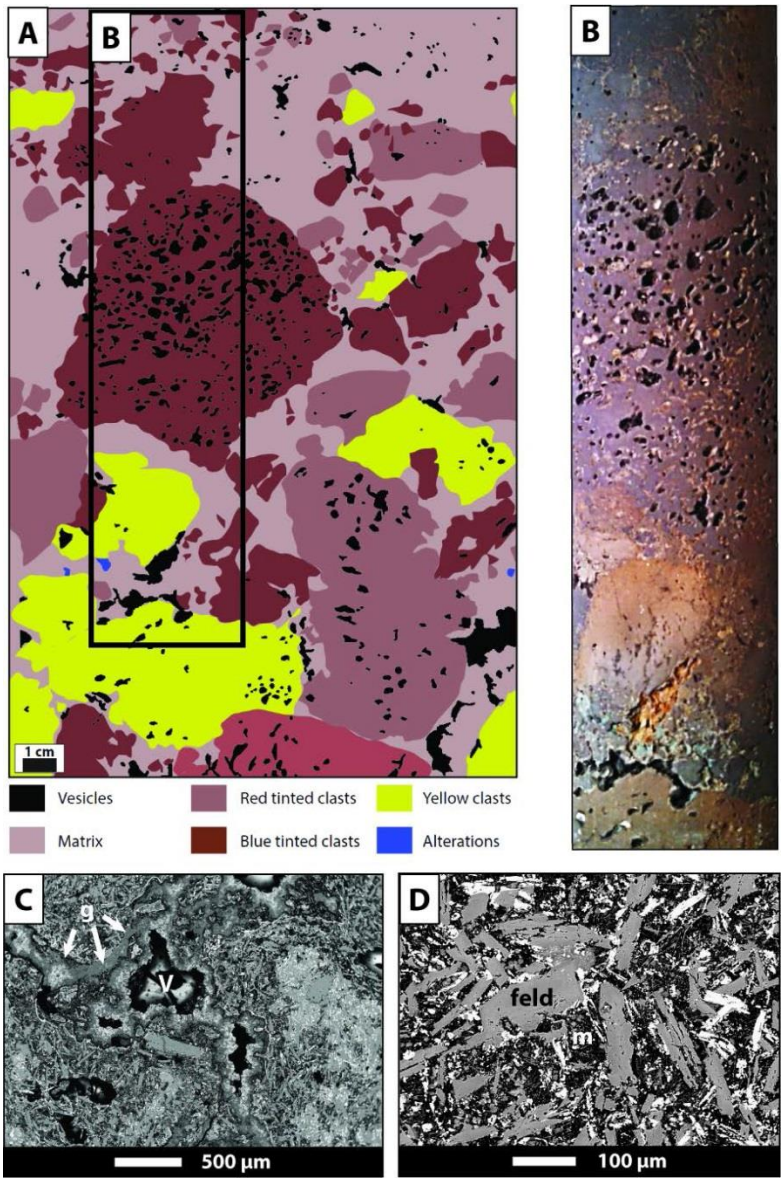

Figure S5.1 Grand Ronde Flood Basalt[64]. (A) Illustration of Grand Ronde basalt highlights the variability of the size and composition of clasts and distribution of vesicles. (B)Porosity varies between clasts. Optical image.(C) Vesicles (black space) are coated with glass (arrow). BSE image. (D) Plagioclase (feld) grains surrounded by a silica-rich matrix (m). Small pyroxene grains are commonly adjacent to ilmenite grains (arrow). BSE image.

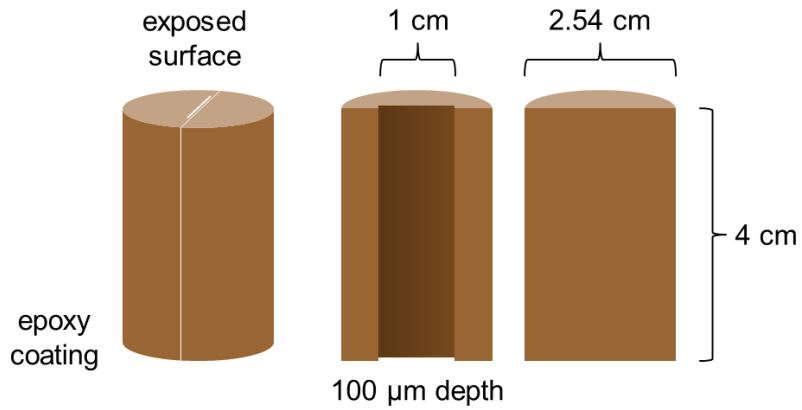

Figure S5.2 Schematic of artificial dead-end fractured basalt core.

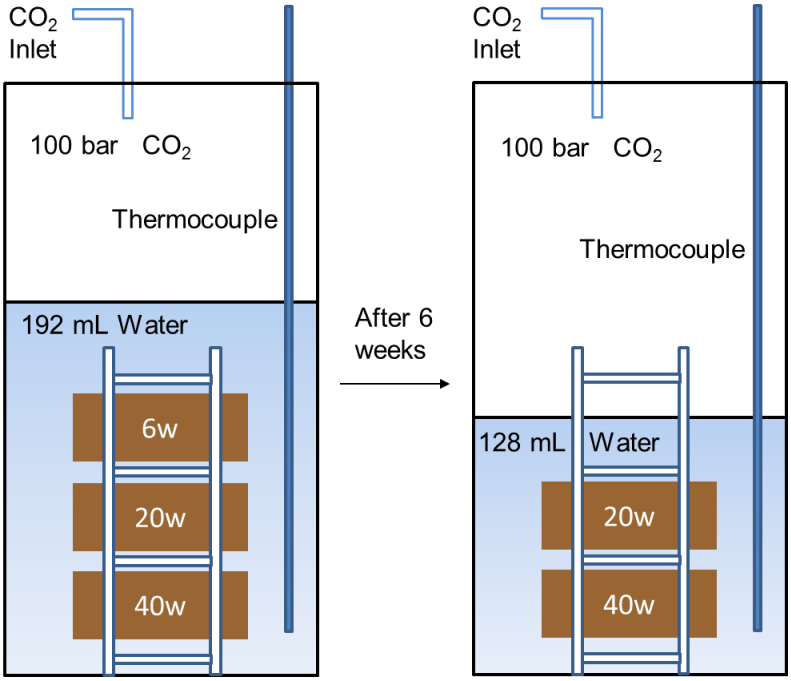

Figure S5.3 Schematic of static batch experiment

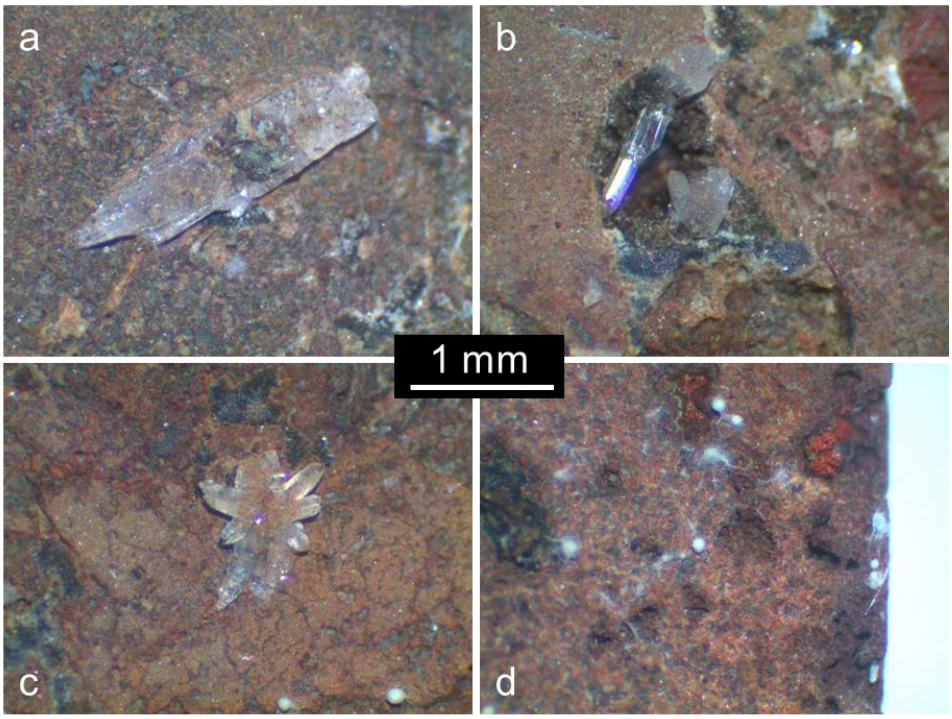

Figure S5.4 Optical microscopic images of secondary precipitates found on the fracture surface of the 20-week basalt core sample.

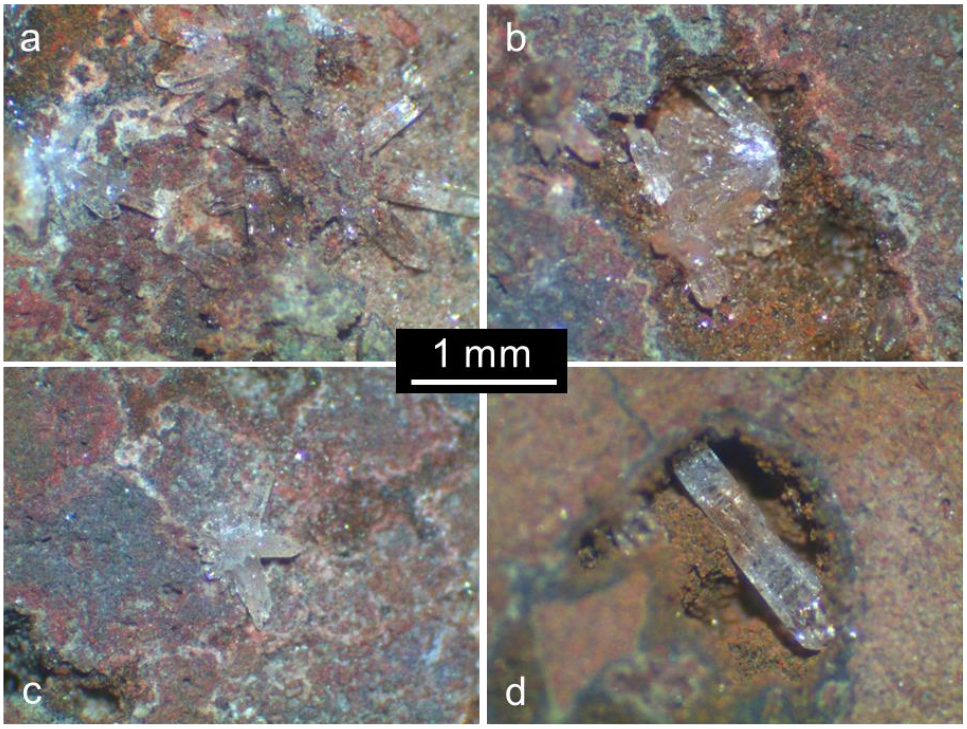

Figure S5.5 Optical microscopic images of secondary precipitates found on the fracture surface of the 40-week basalt core sample.

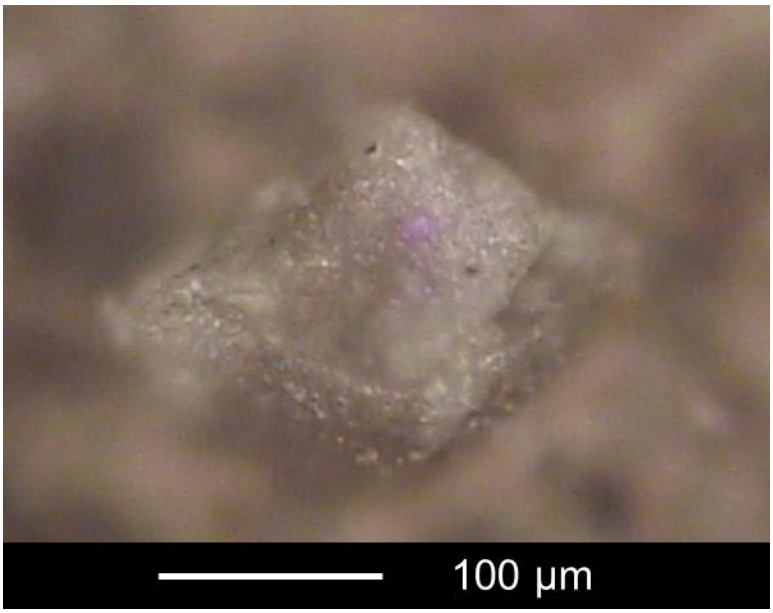

Figure S5.6 Optical microscopic image of a diamond precipitate in the 20-week Grand Ronde basalt core

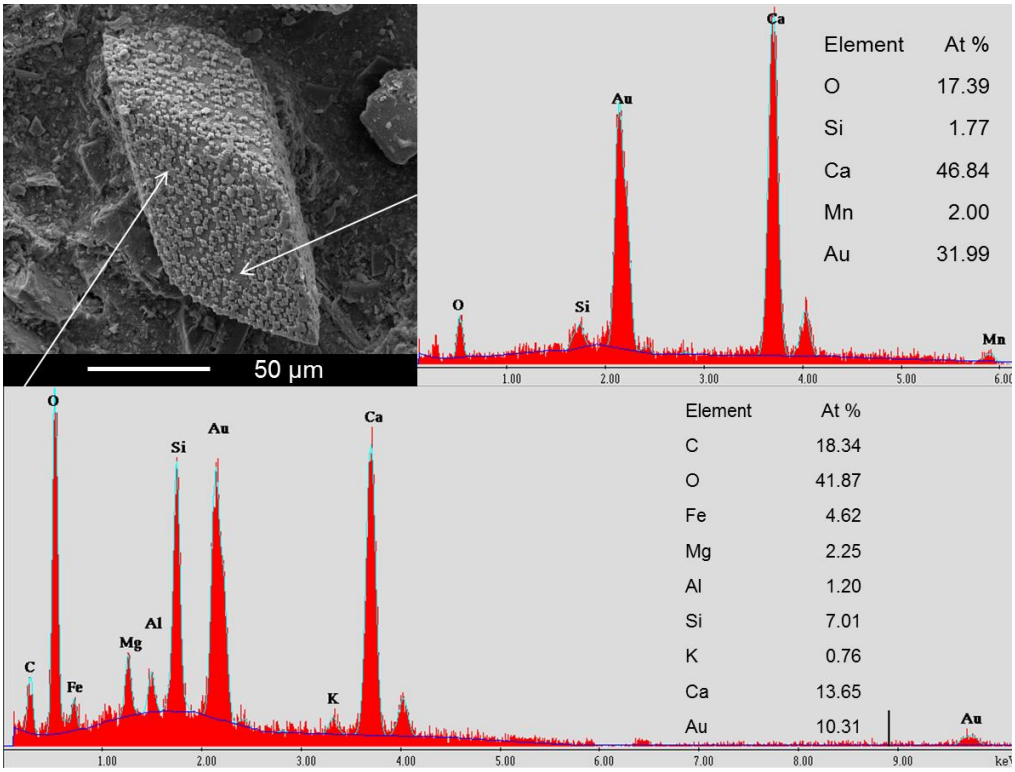

Figure S5.7 SEM-EDX on a precipitate with Si-rich secondary precipitates on the surface in 20-week core with gold coating

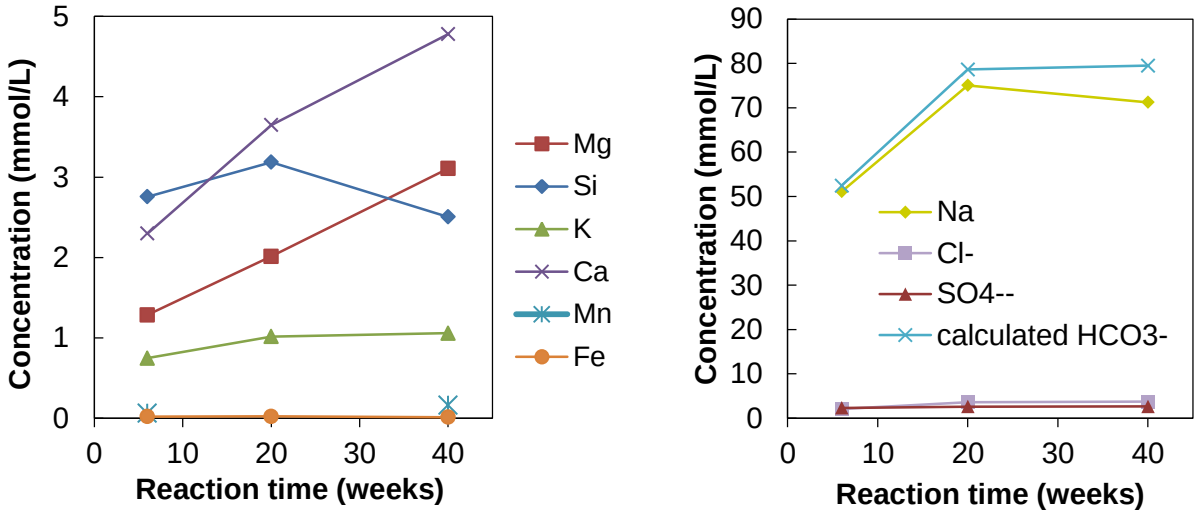

Figure S5.8 Dissolved ions in the bulk solution

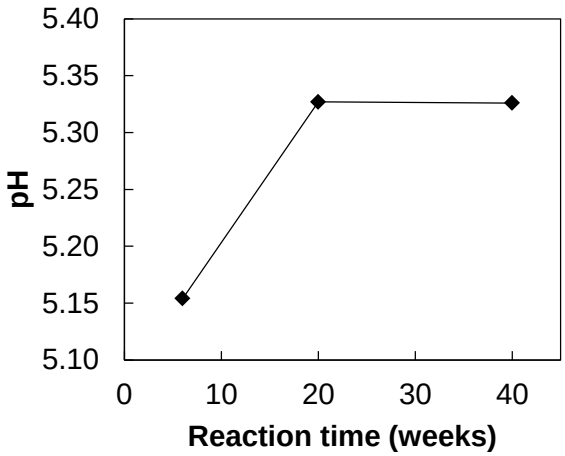

Figure S5.9 Calculated pH in the bulk solution at 100˚C 100 bar.

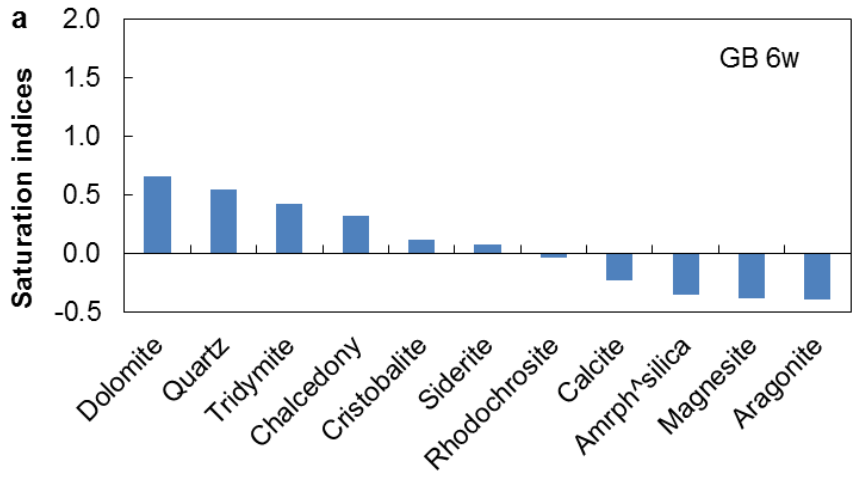
a
Saturation indices
2.0
1.5
1.0
0.5
0.0
-0.5
GB 6w
Dolomite
Quartz
Tridymite
Chalcedony
Cristobalite
Siderite
Rhodochrosite
Calcite
Amrph^silica
Magnesite
Aragonite

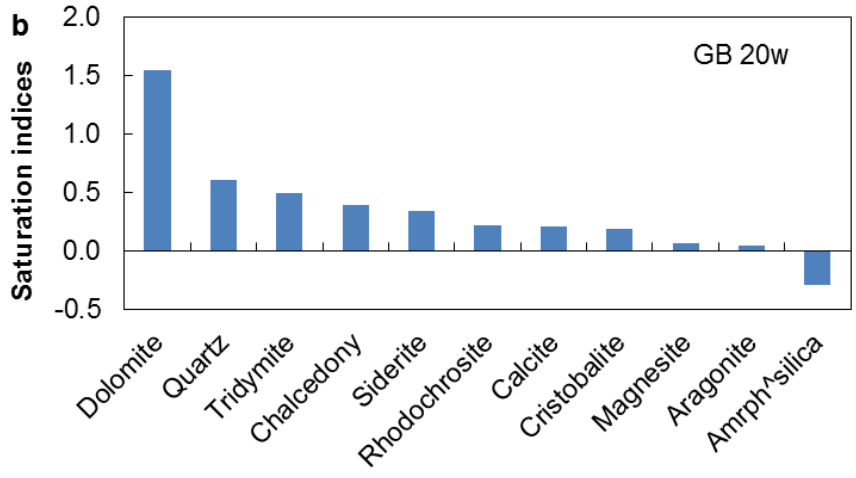
b
Saturation indices
2.0
1.5
1.0
0.5
0.0
-0.5
GB 20w
Dolomite
Quartz
Tridymite
Chalcedony
Siderite
Rhodochrosite
Calcite
Cristobalite
Magnesite
Aragonite
Amrph^silica

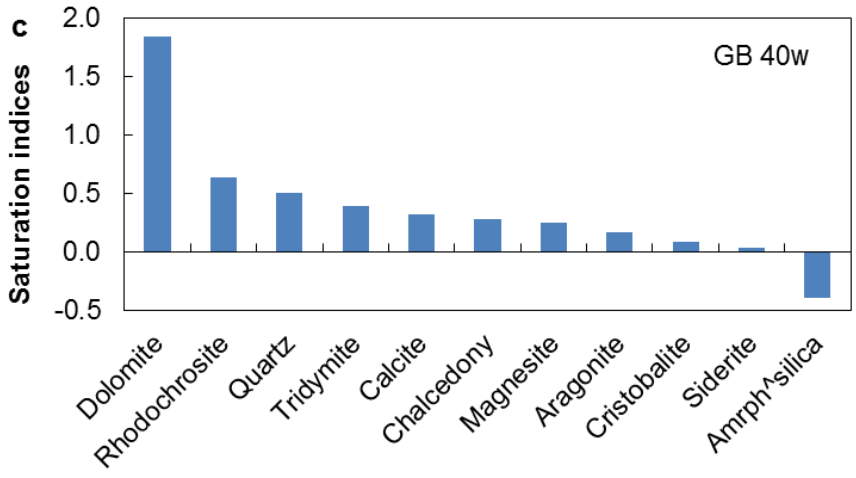
c
Saturation indices
2.0
1.5
1.0
0.5
0.0
-0.5
GB 40w
Dolomite
Rhodochrosite
Quartz
Tridymite
Calcite
Chalcedony
Magnesite
Aragonite
Cristobalite
Siderite
Amrph^silica

Figure S5.10 Saturation indices of selected secondary precipitates in the bulk solution after 40 weeks of reaction. Calculated using SpecE8 in Geochemists' Workbench.

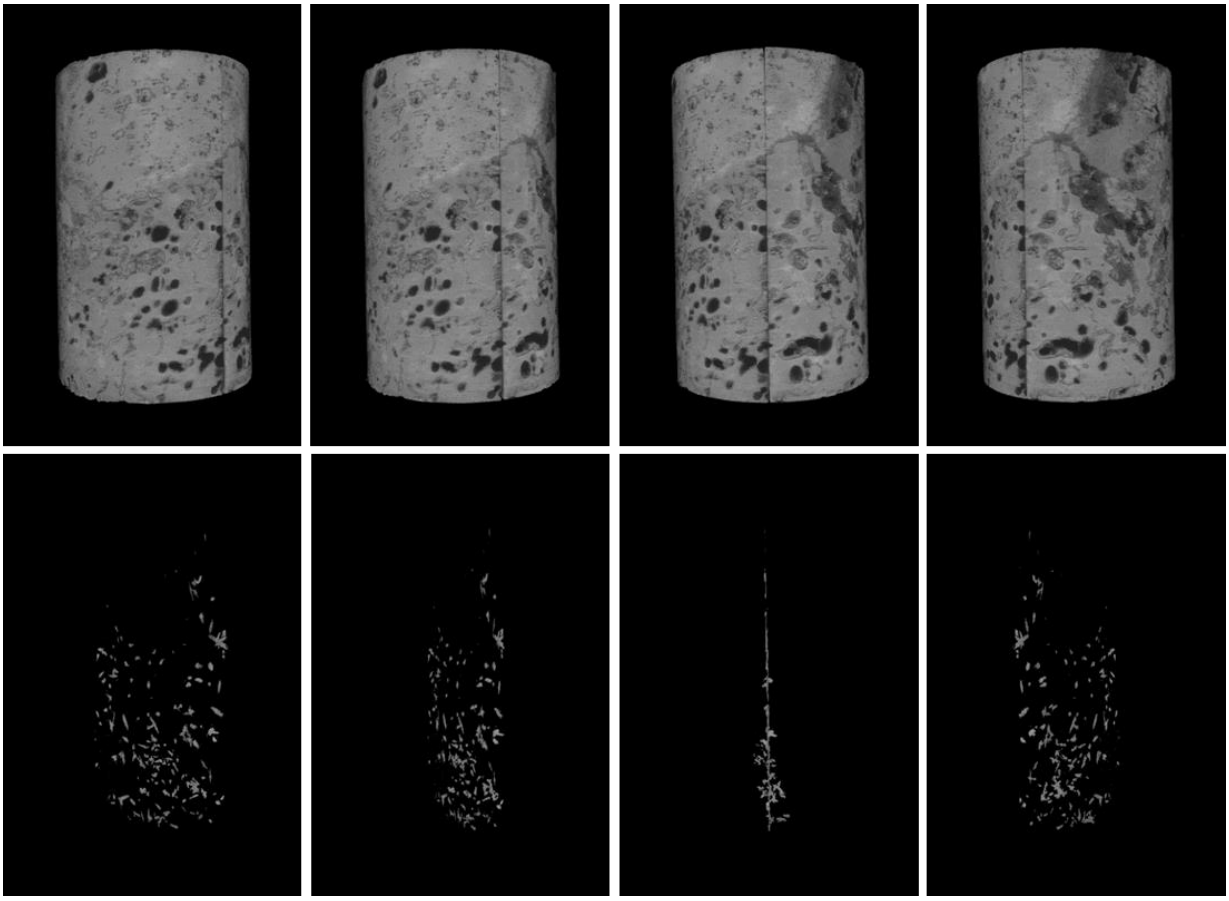

Figure S5.11 3D segmentation of 20-week Grand Ronde basalt core

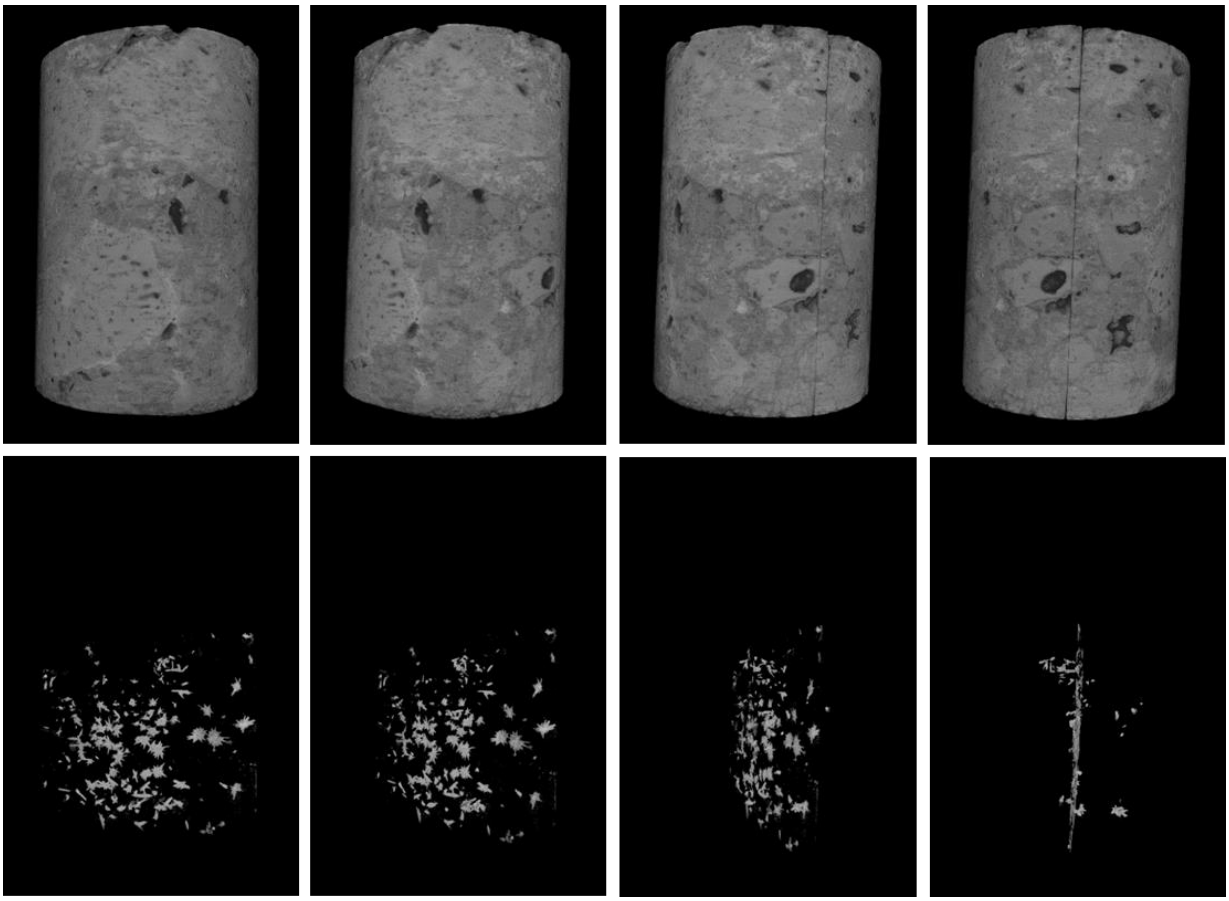

Figure S5.12 3D segmentation of 40-week Grand Ronde basalt core

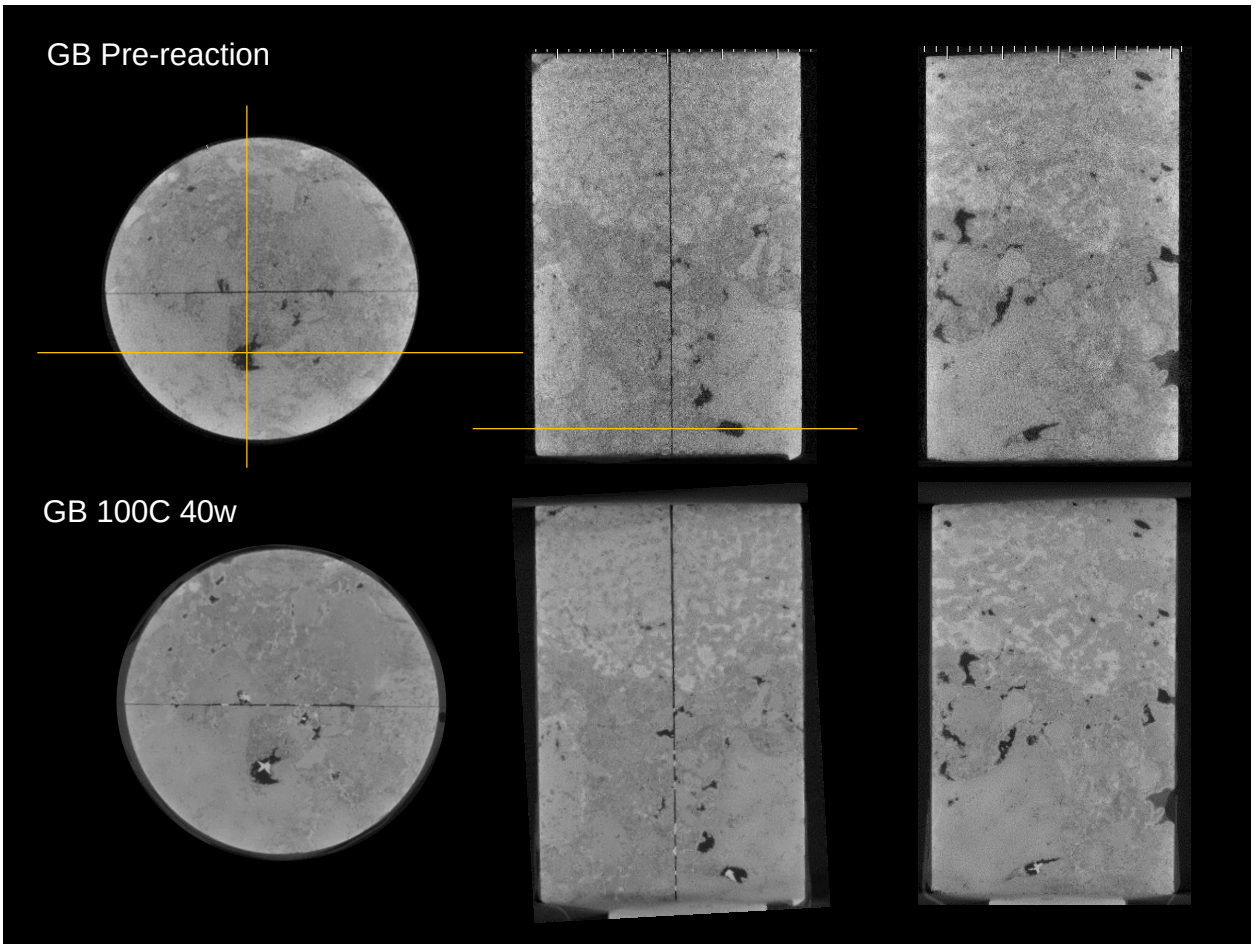

Figure S5.13 Orthographic views of precipitates in a pore not connecting the fracture in Grand Ronde basalt core reacted for 40 weeks.

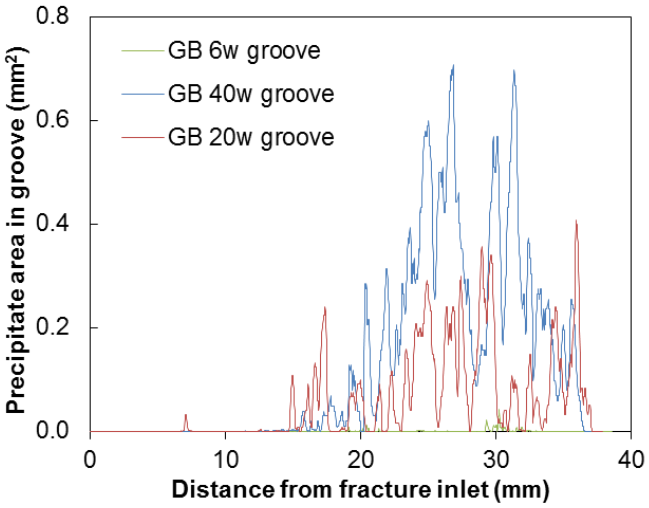

Figure S5.14 Precipitate area in the 100 μm fracture in each round cross section CT slice from segmentation.

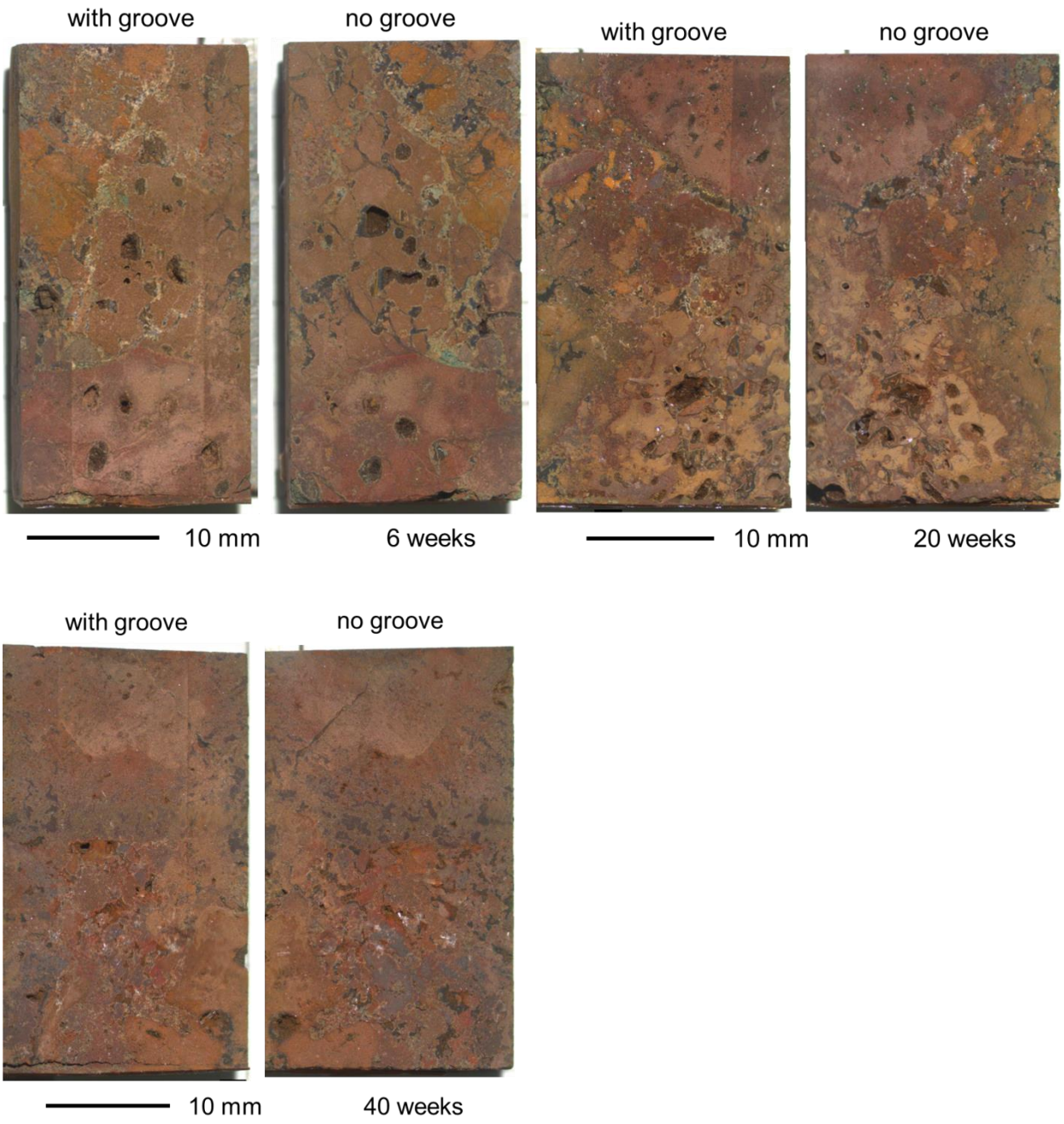

Figure S5.15 Optical microscopic images of the fracture surfaces of the three basalt cores reacted for 6, 20 and 40 weeks.

Chapter 6. Conclusions and Recommendations for Future Work

6.1 Conclusions

This research provides information regarding the timing, type and location of carbonate mineral formation in zones controlled by diffusion based on experimental results and analysis. The findings of this research could help better understanding carbonate formation in fractures and porous media and contribute to more accurate estimation of basalt reservoir capacity and safety.

6.1.1 Carbonation in porous powder packed beds

Carbonate mineral formation in porous media is influenced by the coupling of solute transport and geochemical reactions. The transport in the porous powder packed beds is controlled by diffusion. In the dead-end porous beds packed with reactive forsterite powders, carbonate minerals are unevenly distributed along the packed bed as a result of opposing chemical gradients driven by concentration differences in the bed and in the outside bulk solution. This spatial distribution of chemical gradients leads to massive carbonate mineral formation in certain locations that are most favorable for precipitation. Hydromagnesite occurred in early reactions and disappeared after a few days of reaction. Magnesite became the only thermostable carbonation product after long time of reaction. The carbonation of forsterite packed beds did not shut itself down during the 60 days of reaction, but it did slow down after 30 days.

Olivine power packed beds with smaller powders can provide more reactive surface area and sequester more CO_2 than larger powder packed beds. More carbonate precipitates formed in

packed beds with Fe-containing olivine powders than that with the pure magnesium end-member forsterite. CO_2 mineralized to magnesite in olivine powder packed beds. In porous packed beds with flood basalt powders, siderite was observed as the carbonation product. Different basalt types have different carbon mineral trapping capacity.

6.1.2 Carbonation in fractured basalt rocks

Carbonate mineral formation in basalt happens rapidly, making basalt an effective host rock for CO_2 mineral trapping. Carbonate minerals precipitation in basalt is orders of magnitude faster than in sandstone. Carbonate minerals primarily form in fractures and pores where the transport is controlled by diffusion. The precipitates in the fracture are spatially distributed. Certain locations are more favorable for carbonate minerals to precipitate. The precipitation did not block the transport pathways. Unaltered flood basalt has higher CO_2 mineral trapping capacity than the serpentinized basalt. Higher temperature can accelerate the carbonation reactions. Siderite formed in the flood basalt and serpentinized basalt which are Fe- and Mg-rich. In Ca-rich Grand Ronde basalt, calcium carbonate with predominant aragonite was the carbonation product.

The presence of fractures and pores in basalt is important to successful mineral trapping of CO_2. Fractures and pores provide substantial surface area for dissolution and precipitation reactions. The diffusion-controlled transport allows cations to accumulate and for the solution to achieve supersaturation with respect to carbonate minerals. The type of basalt is another important aspect to consider when choosing injection reservoir. Mineral trapping capacity can be different in basalt with different mineral compositions.

6.2 Recommendations for Future Work

Based on the results and analysis in this thesis, there are several directions that future work could explore:

(1) Fracture evolution in basalt after longer times of reaction. Within the reaction time in this study, the fractures in basalt were not blocked and the precipitation did not shut down. In a reaction that is longer, the precipitation extent can be large enough to crack and expand the fracture to create more surface area. It is also possible that the fracture will be totally blocked by carbonate minerals and end the reaction progress. Fracture evolution study in long time reaction would help to determine whether the process is self-passivating or self-accelerating.

(2) Carbonation in basalt in sea water. Most of the flood basalt on earth is located in the oceanic crust. This study used only deionized water for simplification. The higher salinity in seawater may influence the carbonation rate and products.

(3) Influence of bulk solution changes on carbonation reactions. In this study, the batch reactors have a confined volume in a constant 100 bar CO_2 environment. The bulk solution in the reactor could become equilibrium in a relatively short period compared to geologic time scale. In real situations, the underground aquifer contains huge body of advective water with small amount of stagnant water in dead-end fractures and individual pores. Chemical gradients may change due to the change of the bulk solution, leading to re-dissolution of carbonate minerals. The change of bulk solution may affect carbonate minerals formation in a large system.

Appendix 1. Carbonation of Olivine Sinters

This appendix contains paragraphs from Wells, R. K.; Xiong, W.; Sesti, E.; Cui, J.; Giammar, D.; Skemer, P.; Hayes, S. E.; Conradi, M. S., Spatially-variable carbonation reactions in polycrystalline olivine. Geochim Cosmochim Ac 2017, 204, 252-266.[81]

A1.1 Introduction

Basalt has aroused attention as a promising host rock for CO_2 in geologic carbon sequestration. Olivine is one of the basalt-forming minerals with the highest dissolution rate and CO_2 mineral trapping capacity. Olivine dissolution and carbonation can be summarized in the following equations using Mg-olivine as an example:

$$Mg_2SiO_{4(s)} + 4H^+ \rightleftharpoons 2Mg^{2+} + SiO_{2(aq)} + 2H_2O \quad \text{Eq. A1.1}$$

$$Mg_2SiO_4\,(\text{Olivine}) + 2CO_2 = 2MgCO_3\,(\text{Magnesite}) + SiO_2 \quad \text{Eq. A1.2}$$

Olivine sinters are artificial polycrystalline aggregates made from fine olivine powders. Previous study in porous olivine powder packed beds showed spatial distribution of carbonate mineral formation in zones controlled by diffusive transport[27]. The porosity of the powder packed beds was about 0.5. In real GCS reservoirs, the porosity of the rock formations is often much lower. CO_2 mineral trapping in low porosity diffusion-limited zones is not well understood.

The objective of this study is to observe the timing of precipitation, characterize the composition of the precipitates and determine the location of the precipitates in olivine sinters reated in GCS-relevant conditions. This study has been published in Geochimica et Cosmochimica Acta by Dr. Rachel Wells as the first author[81]. The part I contributed was the olivine (Fo_{90}) sinter static batch experiments and the reacted sample analysis including SEM, Raman Spectroscopy and optical microscopy. The sinters used in the static batch experiments

were provided by Dr. Rolf Bruijn. The contexts below are parts from the paper showing the static batch experiments.

A1.2 Part of Materials and Methods

A1.2.1 Synthesis of starting materials

All experimental samples were synthesized from olivine powders. One set of samples was synthesized from pure synthetic forsterite powder (Fo_{100}) (Mg_2SiO_4; 99% purity; Alfa Aesar), which was sieved to yield particles smaller than 44 μm. The Mg-endmember of olivine was required for the NMR experiments as large concentrations of iron might interfere with the collection of NMR spectra. A second set of samples was synthesized from natural, iron-bearing San Carlos olivine (Fo_{90}) ($Mg_{0.9}Fe_{0.1}SiO_4$). In this case, single crystals of optically clear olivine were separated from ultramafic xenoliths from the San Carlos volcanic field. Olivine grains were crushed in an agate mortar and pestle under water, mechanically milled using an agate ball mill, and sieved to a final grain size of less than 53 μm. Forsterite and olivine powders were used without any further processing.

The powders were pressed and vacuum-sintered following established procedures [106]. Cylindrical pellets were made with 6 mm and 13 mm diameter die molds. The initial porosity of the cold pressed pellets was greater than 0.30, which was calculated by comparing the starting density of the pellet to the theoretical density of olivine. Each pellet was then vacuum-sintered at 1300˚C for 48 hrs at a vacuum of less than 10^{-5} Torr. At these conditions, no evidence of grain growth was observed. This process results in sintered grain contacts and a decrease in porosity to

approximately 0.25. While many of the grain boundaries are sintered, the some of the remaining pores may still be interconnected.

We used two geometries to observe carbonation, one with solid (s) cylinders and one with saw-cut (f) cylinders (Figure 1; Table 1). Solid sample geometries (Fo90_s1, Fo90_s2, and Fo100_s) were left unaltered following vacuum-sintering. Two cylinders (Fo90_f and Fo100_f) were cut in half using a diamond blade rotary saw to simulate a fracture. The fracture orientation for the Fo_{90} sample was made perpendicular to the length of the cylinder, while the Fo_{100} sample was oriented vertically. Each fracture opening is approximately 1 mm as measured using optical microscopy.

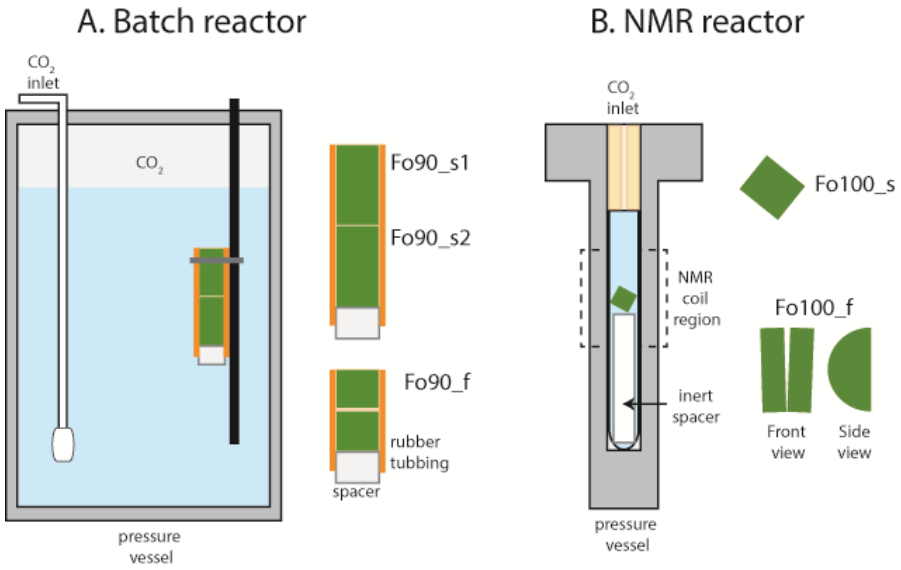

Figure A1.1 Cross-section of high pressure reactors (A) 300-mL batch reactor and (B) a 2-mL in-situ ^{13}C NMR reactor, and the corresponding vacuum-sintered samples.

Table A1.1 Batch and in-situ NMR experiments

Experiment	Sample ID	Geometry	Radius, Length (mm)	Mass (g)	Porosity (%)	Temperature (˚C)	Starting pressure (bar)	Final pressure (bar)	H_2O volume (mL)	Reaction time (days)
1	Fo90_s1	cylinder	3.0, 10.4	0.8	25.1	100	100	100	200	15
	Fo90_s2	cylinder	3.0, 10.1	0.7	26.6					
2	Fo90_f	cylinder with saw cut	3.0, 6.7	0.5	24.7	100	100	100	200	15
3	Fo100_s	cylinder	3.0, 6.5	0.5	17.8	100	100	45	2	102
4	Fo100_f	cylinder with saw cut	6.5, 3.7	0.9	26.9	100	100	100	2	53

A1.2.2 Fo90 experiments

Two different geometries were tested using a high pressure vessel (Parr Instrument, 300 mL stainless steel vessel) (Figure 1; Table 1). One experiment included two single cylindrical samples (each 1 cm in length) (Fo90_s1 and Fo90_s2) stacked end to end. The two samples were joined together with rubber tubing, with the top exposed and the bottom blocked by a short glass rod with the same diameter as the sintered cores (Figure 1A). This setup creates fracture-like openings between the first and second sample and between the outside of the samples and the rubber tubing. We devised another setup that included a single sintered olivine pellet (1 cm in length) (Fo90_f) with a saw cut oriented perpendicular to the vertical axis of the cylinder in the center of the sample. Unlike the fracture-like opening in the stacked experiment, the simulated fracture has a different roughness than that of the end sections and cylindrical sides. This sample was also assembled in rubber tubing with a glass stopper on the end and the top exposed to limit the pathways for fluid transport (Figure 1a).

Each assembly was vertically fixed to tubing that is attached to the reactor head, and then placed in a 300-mL pressure vessel with a PTFE liner. Ultrapure water (200 mL) (resistivity >

18.2 MΩ-cm) was added so that the samples were entirely immersed. After the vessel head was assembled, the sample was heated and then a syringe pump (500D, Teledyne Isco) provided a constant CO_2 pressure (100 bar) on the headspace, with 1% air remaining. The pressure stabilized within 1 hour, indicating the water was at equilibrium with the CO_2. The entire vessel was maintained at 100˚C by a heating mantle, and the stirring speed was set at 60 rpm. These Fo_{90} samples were reacted for 15 days. At the end each experiment, the heating mantle was removed and the vessel was allowed to cool to room temperature. The remaining pressure was allowed to bleed off over several hours. Samples were removed from the vessel and allowed to air-dry at room temperature. Precipitates were observed on the surface of the sample before drying.

A1.2.3 Post-reaction analysis

Fo_{90} samples (Fo90_s1, Fo90_s2, and Fo90_f) were dissected into five slices from the top in 1 mm increments. The outer surface was analyzed using Raman spectroscopy (HoloLab Series 5000 Laser Raman Microprobe, Kaiser Optical), with a 532 nm laser and a 20x power objective that probes a 5 μm area. The pH of the starting solution was calculated using charge balance for a water and CO_2 system at 100˚C and 100 bar. Equilibrium constants were determined with the program SUPCRT92, and CO_2 solubility was calculated using the model[54]. Analysis of precipitates on the outer surface of the Fo_{90} samples was made using optical and electron microscopy (JEOL 7001LVF FE-SEM; FEI Nova 230).

A1.3 Part of Results

A1.3.1 Single cylinder experiments (Fo90_s1 and Fo90_s2)

After 15 days of reaction, we observed precipitates on the outer surface of each sample using both optical and electron microscopy (Figure 2a). These precipitates occurred between the sample and the rubber tubing ~2-3 mm below the top of the sample that was open to the CO_2-rich aqueous solution. We also observed precipitates between the bottom of Fo90_s1 and the top of Fo90_s2 (Figure 2b). No precipitates were observed on the top surface of Fo90_s1 or within either sample. Mg concentrations are too low for nucleation on the top surface of the sample that is exposed to the bulk solution because Mg can diffuse away from the surface into the 200 mL of solution, and the pH is also at its lowest here. The precipitates grew to a size of 5-40 μm on the surface of the samples, and are at their maximum concentration approximately 1 cm down from the top of the uppermost cylinder (Fo90_s1). Raman spectroscopy of the precipitates on the surface shows strong peaks at 1094 cm^{-1} and 330 cm^{-1}, which correspond to the CO_3^{2-} symmetric stretching external mode (V_1) in magnesite (Fig. 2c) [46, 67]. We also analyzed the surface of the sample that had no visible precipitates. The peaks at 824, 855, and 964 cm^{-1} correspond to the stretching modes of the three types of Si−O bonds in olivine [45]. The three olivine peaks are also observed in the magnesite spectra because the beam, which was bigger than the magnesite grain, detected both the precipitate and the host Fo_{90}. No other precipitates were observed on the surface of the samples.

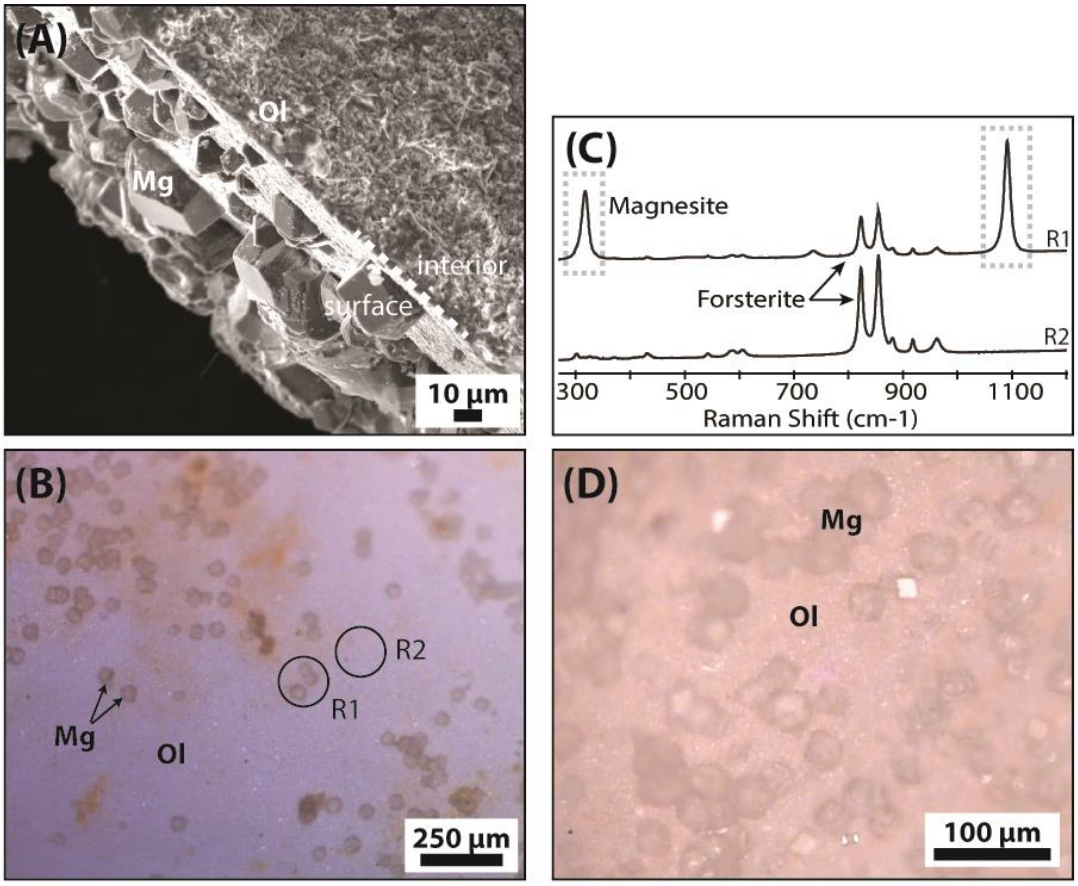

Figure A1.2 San Carlos Olivine (Fo_{90}) experimental microscopy and spectroscopy results with (A) SE image of magnesite (Mg) crystals on the side of one Fo90 (Ol) cylinder (Fo90_s1), (B) optical photomicrograph of the bottom surface of Fo90_s1, which contains ~50 µm magnesite grains, (C) Raman spectra of two surface sites (R1, R2) indicating Fo_{90} (arrows) and magnesite (dashed box), and (D) optical photomicrograph of magnesite grains on the surface of the fracture (OL3_f).

A1.3.2 Fractured cylinder experiment (Fo90_f)

The fractured Fo_{90} sample (Fo90_f) was also reacted for 15 days, and contains precipitates on the vertical walls of the cylinder, between the sample and the rubber tubbing,

which is where we observed precipitates in the single cylinder (Fo90_s1 and Fo90_s2). Precipitates are also observed on the fracture surface (Figure 2d). Within the horizontal fracture, the grains are 10-50 μm and do not seal the fracture opening. Raman spectroscopy confirmed that these precipitates are also magnesite. These findings are similar to what we observed in the stacked single cylinder experiments, which suggests that these results are consistent and reproducible.

A1.4 Part of Discussion

A1.4.1 Precipitate composition and morphology

Magnesite is observed as precipitates on the surface of the Fo_{90} and Fo_{100} reacted samples despite the different geometries, reaction times, pressure conditions, and solid-to-water ratios. Single grains formed on all of the Fo_{90} samples. The euhedral grains on the surface of every reacted sample are likely the result of crystal growth following heterogeneous nucleation.

Magnesite was the only magnesium-rich carbonate mineral observed, and no hydroxylated or hydrated magnesium carbonate minerals (i.e., nesquehonite, hydromagnesite) were observed. The reaction of Fo_{90} and Fo_{100} samples with aqueous CO_2 results in magnesite only, rather than a mixture of such species, as found previously with powdered Mg_2SiO_4 at lower temperatures[107]. At lower temperatures (< 100˚C) and pressures, nesquehonite and hydromagnesite are more likely to precipitate than magnesite[108-111]. Xiong and Giammar[27] documented the occurrence of hydromagnesite within 5 days of reaction using packed forsterite powder beds at 100˚C, but hydromagnesite was not observed in samples reacted for longer time periods. These observations suggest that there might also be a time component to the formation

of magnesite or dehydration from hydromagnesite to magnesite. All samples within this study were reacted at 100˚C, which is more likely for magnesite precipitation, and were reacted for 15-102 days, which may have offered time for magnesite to precipitate as opposed to other kinetically slow phases.

Amorphous silica is also observed in all experiments. Amorphous silica occurred as a minor precipitate on the surface of a Fo_{90} sample (Figure 2A). In previous short term experiments, layers of amorphous silica observed on the surface of individual forsterite grains are thought to be the result of hydrolysis reaction with nearby silica following the dissolution of Mg^{2+} and $SiO_{2(aq)}$ from the surface of individual forsterite grains [17, 112-116]. The formation of these grain-like structures has only been documented in a few experimental studies that reacted natural peridotite in aqueous CO_2 [42, 43] and olivine in a strongly acidic H_2SO_4 solution [117]. The tendency for the amorphous silica to preserve the approximate shape of the host forsterite grain indicates that dissolution of the forsterite and precipitation of the amorphous silica occurred simultaneously and were tightly coupled at the reaction interface [117, 118].

A1.4.2 Analysis of post-reaction texture

This study observes similar spatial trends documented in previous study[27] on the vertical surface of the reacted Fo_{90} samples. The highest concentration of magnesite crystals in the zone between the surface of the Fo_{90} samples and the rubber tubing occurred approximately 1 cm below the top surface of the cylinder.

A1.4.3 Implications for Geologic Carbon Sequestration

An enticing prospect of carbon storage in fractured basalt is the possibility of mineral trapping as a permeant storage solution. In other lithologies (e.g., sandstones, carbonates, shale, coal), mineral trapping is thought to occur over thousands of years[3]. Based on the experiments presented in this study, the timing of carbonation of olivine-rich lithologies (e.g., peridotites) is expected to begin much earlier, particularly at higher temperatures (e.g., ≥100˚C). Even at lower temperatures more realistic to carbon storage (<50˚C), the mineralization of the injected CO_2 is expected to occur at faster rate compared to other reservoir types.

The spatial relationships of precipitates in our sintered forsterite experiments suggest that the reaction between olivine-rich lithologies and injected supercritical CO_2 may also be more complicated than in previous studies using unconsolidated particles or single grains. Despite the homogeneous mineralogy, pre-existing structural features influence the spatial progression of the reaction. Fractures will act as diffusion-limited zones, and carbonate minerals will precipitate within and into the surrounding fracture wall, guided by the intragranular porosity, while the overall shape of the fracture remains constant. While earlier studies[17, 38, 39, 113] suggest that amorphous silica may block reactive mineral surfaces and slow down subsequent reactions, the dissolution of silicate minerals may not be impeded by the formation of an amorphous silica layer. Our study indicates that this does not occur in individual grains or as a lithic unit, but rather contributes to the overall texture of the post-reaction sample. The concurrent dissolution of olivine grains and precipitation of amorphous silica results in a post-reaction sample that is not noticeably different from the starting geometry. As carbonation progresses, amorphous silica and magnesite that are already precipitated will influence the location of subsequent precipitation.

Current basalt carbon storage test sites indicate the mineralization of injected CO_2 occurs within 2 years[19, 22]. While the carbonation is promising, the resulting precipitate structure may influence additional CO_2 injections or any reaction-driven fracture propagation. A heterogeneous mineralogy with different dissolution rates and more diverse carbonation reactions will influence any progressive reaction structures (e.g., the amorphous silica layer) and overall geometry of the reaction products, which may not be observed in studies of homogeneous materials. Additional studies are needed to address the influence heterogeneous compositions exert on the final reaction in natural reservoirs.

Appendix 2. Flood basalt core reacted in wet-scCO_2

A2.1 Introduction

Global warming is regarded as an environmental issue caused by excessive anthropogenic CO_2 emissions. Geologic carbon sequestration is a method to mitigate CO_2 emission to atmosphere by injecting supercritical CO_2 into deep geologic formations[3]. CO_2 can ultimately be trapped as stable carbonate minerals. Basalt was proposed as an efficient host rock with high mineral trapping capacity of CO_2.[20] Two pilot-scale CO_2 injections into basalt have been conducted in Iceland[19] and in Washington State, USA[22]. The Big Sky project in Washington directly injected supercritical CO_2 as a separate buoyant phase into deep a porous basaltic layer at more than 800-m depth.[20]

The injected CO_2 is buoyant in contact with the host formation and caprock, becoming a water-bearing scCO_2 phase.[119] Most studies on geologic carbon sequestration considered traditional aqueous systems with dissolved CO_2 in the water phase. However, a water-bearing scCO_2 (wet-scCO_2) system in which nonaqueous-dominanted types of mineral dissolution and precipitation reactions take place should also be considered.[120] According to a model of mutual solubility of CO_2-H_2O mixture, H_2O mole fraction in CO_2-rich phase is only 0.017 at 100˚C and 100 bar.[121] The water content in the scCO_2 phase is crucial for successful carbonation. Previous study used *in situ* infrared spectroscopy to examine carbonation of synthetic forsterite in dry and wet scCO_2 and found no reaction products under dry conditions[122]. Only when a thin water film on forsterite grains appeared could carbonation occur as water in scCO_2 reached 55% of the saturation level[122]. Another study also observed hydrated Mg-carbonates on the surface of

forsterite grains when $scCO_2$ was undersaturated with 74% water.[123] Water in the $scCO_2$ phase should be enough to maintain a thin water film in order for carbonation reactions to occur.[124]

In water-saturated wet-$scCO_2$ carbonation should be able to happen. However, in basalt reservoirs with a lot of fractures and pores, carbonation in wet-$scCO_2$ may be greatly inhibited by diffusive transport limitations. The majority of research on wet-$scCO_2$ focused on carbonation on highly reactive olivine mineral surfaces that were entirely exposed to the bulk wet-$scCO_2$ environment. In this study, we investigated secondary mineral formation in an artificial dead-end fracture in flood basalt in water-saturated wet-CO_2 in 100 bar 100˚C for up to 40 weeks.

A2.2 Materials and Methods

A2.2.1 Fractured basalt cores

Columbia River Flood basalt (FB) from Pullman, Washington was purchased from Ward's Science. Multiple cylindrical cores with 25.4 mm diameter and ~43 mm length were made from the bulk rock. Each core was cut to half cylinders. The surface of one cylinder was polished with sandpaper. The other half surface was milled with a straight 11 mm wide groove using a milling machine (Roland Model MDX-40a) with a 0.5 mm diamond bur. The grooved half was polished until the groove was 100 μm deep. The groove depth was determined by comparing the z-value of the spots on the groove and the spots on the closest polished surface in an optical microscope (ZEISS, Observer Z1). The two half cylinders were attached together to form one cylinder with the 100 μm groove in the middle as a dead-end microfracture. The bottom and the side surfaces of the core were coated with epoxy (MasterBond EP42HT-2), only exposing the top surface with the fracture opening. The flood basalt is composed of 31% feldspar,

22% pyroxene, 1% orthopyroxene, 9% olivine, 1% serpentine, 33% potassium-rich matrix and 3% ilmenite[64].

A2.2.2 Static batch experiments

Three fractured flood basalt cores were placed on a multilevel PTFE holder, which was put in a PTFE liner inside a 600 mL stainless steel high pressure vessel (Parr Instrument). A small amount of deionized water (50 mL) was added to the reactor. All three cores were above the water. The batch was heated to 100˚C by heating tapes with heat controller (Omega, CSi32 Series). A headspace of 100 bar CO_2 was maintained in the reactors by a syringe pump (500D, Teledyne Isco). At 100˚C and 100 bar, 50 mL water was enough for the CO_2 phase to be saturated with H_2O [121]. Core samples were collected one by one after reacting for 6, 20, 40 weeks. Before starting each experiment, the reactor was flushed with 10 bar CO_2 for three times to minimize residual O_2. The process of cooling and depressurizing for sample collection and restarting the reactor was ~5 hours.

A2.2.3 Analytical methods

The 40-week core was scanned by X-ray computed tomography (CT) after reaction (Nikon Metrology XTH225). The voxel resolution of the CT images was 24.3 μm. The core was cut open after CT scanning. Optical microscopy (LEICA, DFC295) was used to examine the fracture surface. Raman spectra on observable secondary precipitates were collected (HoloLab Series 5000 Laser Raman Microprobe, Kaiser Optical) with a 532 nm laser. The Raman spectra were compared with Raman standards from the RRUFF database.

A2.3 Results and Discussion

For the cores after reaction, there were plenty of noticeable red dots on the fracture surface (Figure A2.1), which might be iron oxides. Especially in the 40-week sample, the top 3-13 mm region near the fracture inlet was covered with red spots. A lot of pores resulting from basalt mineral dissolution were observed in this region. It was possible that a thin film of water was stuck in this region due to capillary force and accelerated dissolution here. This mechanism is similar to the residual trapping of CO_2 during geologic carbon sequestration.

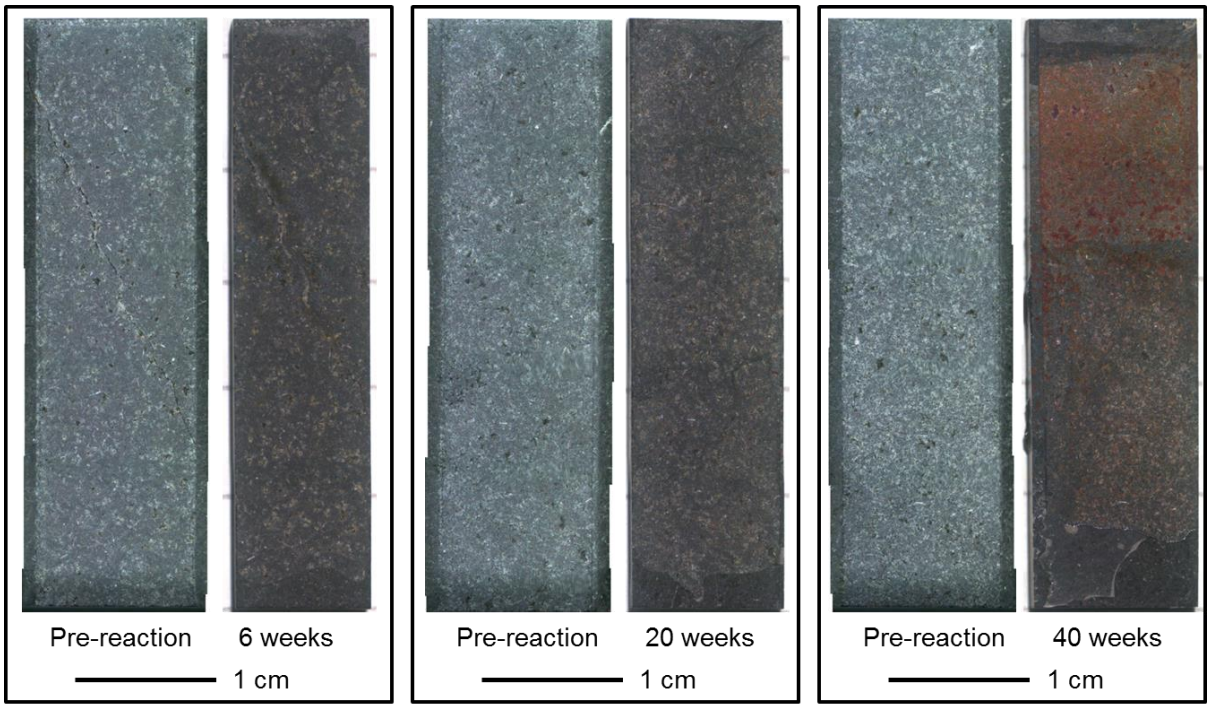

Figure A2.1 Groove surfaces before and after reaction in wet-CO_2.

A very limited amount of secondary precipitates was observed on the fracture surface of basalt cores reacted in wet-CO_2. In the post-reaction CT scan, one potential carbonate mineral was about 28 mm away from the fracture inlet (Figure A2.2). The precipitate was lighter than the background in CT. The cross section image showing the 100 μm fracture revealed that the

precipitate was on the groove side surface and was about 50 µm. This precipitate was also located in optical microscopy and then examined by Raman spectroscopy. A 12 µm long needle-like carbonate precipitate formed on top of a 50 µm mineral cluster. The needle precipitate was identified as aragonite.

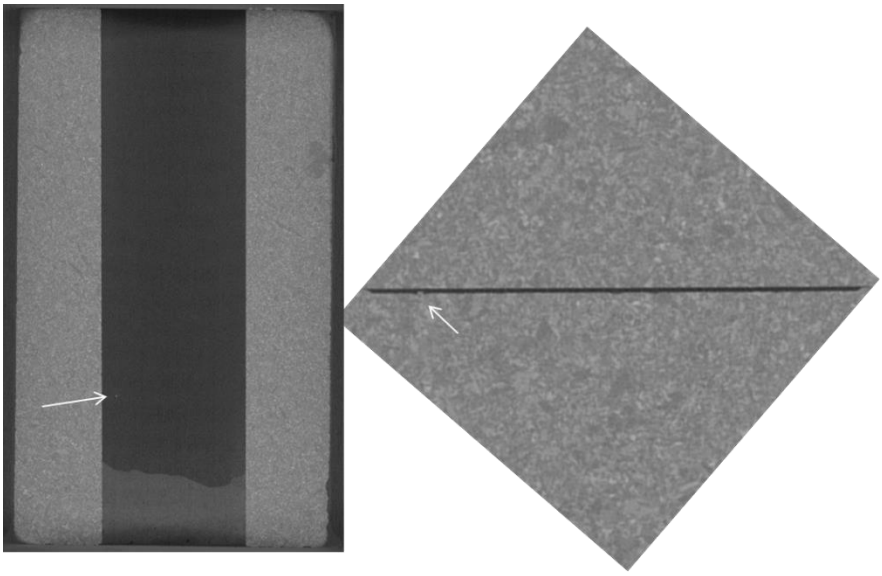

Figure A2.2 Post-reaction CT image of the flood basalt core reacted for 40 weeks in 100˚C and 100 bar wet-CO_2. The arrow points to a carbonate precipitate shown in Figure A2.3.

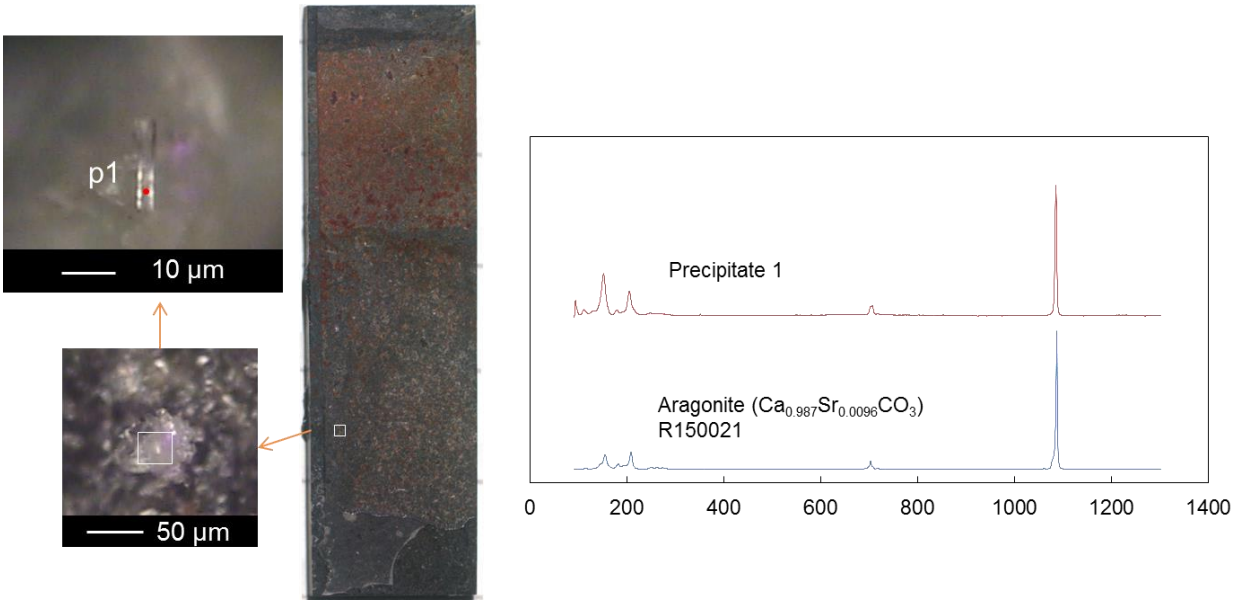

Figure A2.3 Needle precipitate identified as aragonite in Raman spectroscopy

Carbonation reactions are much slower in wet-CO_2 than in CO_2-rich water. In previous experiments with fractured flood basalt reacted in CO_2-rich water, large amounts of carbonate minerals covered the fracture surface in the same pressure and temperature reacting for the same time.

Other secondary precipitates containing sulfur were observed. A few other secondary precipitates were identified as anhydrite at the fracture end (Figure A2.4). In experiments with multiple 2.0-0.42 mm basalt chips from a variety of places in the CO_2-SO_2-O_2 water system at 90˚C, 88~114 bar for 98 days, secondary precipitates containing sulfur such as gypsum were observed on the basalt surface.[59] The CO_2 used in this study was pure and no SO_2 was present. The sulfur might come from the dissolution of basalt. In our previous study with the same flood basalt, an appreciable amount of dissolved SO_4^{2-} was measured in the bulk solution.

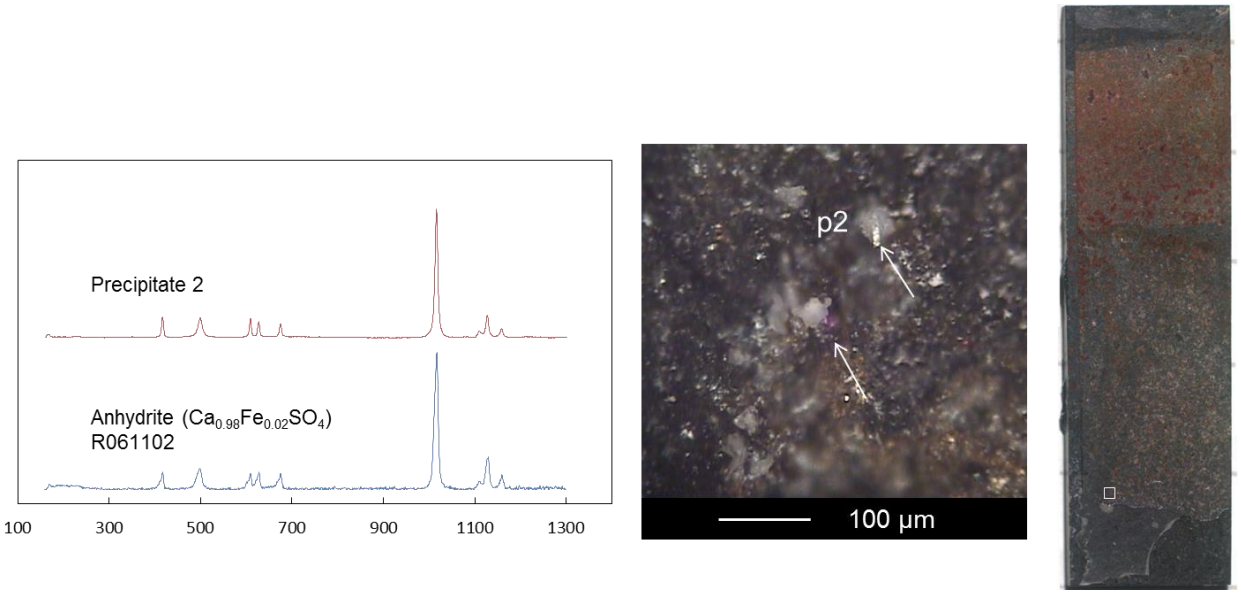

Figure A2.4 Anhydrite found at the bottom of the fracture.

Overall, the fractured basalt reacted in wet-scCO_2 did not sequester much CO_2 in carbonate minerals. Pre-injection treatment of dissolving supercritical CO_2 into large volume of water can be a good way to improve CO_2 mineral trapping. In the CarbFix project in Iceland, CO_2 is released as small bubbles at 350-m depth into down-flowing water within the injection well, allowing CO_2 to dissolve in water.[20] This would greatly reduce the time needed for mineral trapping. 95 % of the injected CO_2 mineralized within 2 years.[19] However, this method would require huge amount of water and may not be economically favorable.

Reference

1. Albritton, D.; Meira Filho, L., Climate change: the scientific basis; contribution of working group I to the third assessment report of the Intergovernmental Panel on Climate Change—technical summary. *IPCC, Geneva* **2001**.

2. Pacala, S.; Socolow, R., Stabilization wedges: solving the climate problem for the next 50 years with current technologies. *Science* **2004,** *305*, (5686), 968-972.

3. *IPCC, IPCC Special Report on Carbon Dioxide Capture and Storage*. Cambridge University Press for the Intergovernmental Panel on Climate Change: Cambridge, 2005.

4. Bachu, S., Sequestration of CO_2 in geological media: criteria and approach for site selection in response to climate change. *Energy conversion and management* **2000,** *41*, (9), 953-970.

5. Bachu, S., Sequestration of CO_2 in geological media in response to climate change: road map for site selection using the transform of the geological space into the CO_2 phase space. *Energy conversion and management* **2002,** *43*, (1), 87-102.

6. Schrag, D. P., Storage of carbon dioxide in offshore sediments. *Science* **2009,** *325*, (5948), 1658-1659.

7. Haszeldine, R. S., Carbon capture and storage: how green can black be? *Science* **2009,** *325*, (5948), 1647-1652.

8. Stéphenne, K., Start-up of world's first commercial post-combustion coal fired CCS project: contribution of Shell Cansolv to SaskPower Boundary Dam ICCS Project. *Energy Procedia* **2014,** *63*, 6106-6110.

9. Jun, Y. S.; Giammar, D. E.; Werth, C. J., Impacts of Geochemical Reactions on Geologic Carbon Sequestration. *Environ Sci Technol* **2013,** *47*, (1), 3-8.

10. Middleton, R. S.; Keating, G. N.; Stauffer, P. H.; Jordan, A. B.; Viswanathan, H. S.; Kang, Q. J.; Carey, J. W.; Mulkey, M. L.; Sullivan, E. J.; Chu, S. P., The cross-scale science of CO_2 capture and storage: from pore scale to regional scale. *Energy & Environmental Science* **2012,** *5*, (6), 7328-7345.

11. Bourg, I. C.; Beckingham, L. E.; DePaolo, D. J., The Nanoscale Basis of CO_2 Trapping for Geologic Storage. *Environ Sci Technol* **2015,** *49*, (17), 10265-10284.

12. Matter, J. M.; Kelemen, P. B., Permanent storage of carbon dioxide in geological reservoirs by mineral carbonation. *Nature Geoscience* **2009,** *2*, (12), 837-841.

13. Gunter, W. D.; Perkins, E. H.; McCann, T. J., Aquifer disposal of CO_2-rich gases: reaction design for added capacity. *Energy conversion and management* **1993,** *34*, (9), 941-948.

14. Oelkers, E. H.; Gislason, S. R.; Matter, J., Mineral Carbonation of CO_2. *Elements* **2008,** *4*, (5), 333-337.

15. McGrail, B. P.; Schaef, H. T.; Ho, A. M.; Chien, Y. J.; Dooley, J. J.; Davidson, C. L., Potential for carbon dioxide sequestration in flood basalts. *Journal of Geophysical Research-Solid Earth* **2006,** *111*, (B12).

16. Goldberg, D. S.; Takahashi, T.; Slagle, A. L., Carbon dioxide sequestration in deep-sea basalt. *Proceedings of the National Academy of Sciences of the United States of America* **2008,** *105*, (29), 9920-9925.

17. Bearat, H.; McKelvy, M. J.; Chizmeshya, A. V. G.; Gormley, D.; Nunez, R.; Carpenter, R. W.; Squires, K.; Wolf, G. H., Carbon sequestration via aqueous olivine mineral carbonation: Role of passivating layer formation. *Environ Sci Technol* **2006,** *40*, (15), 4802-4808.

18. Kelemen, P. B.; Matter, J., In situ carbonation of peridotite for CO_2 storage. *Proceedings of the National Academy of Sciences of the United States of America* **2008,** *105*, (45), 17295-17300.

19. Matter, J. M.; Stute, M.; Snaebjornsdottir, S. O.; Oelkers, E. H.; Gislason, S. R.; Aradottir, E. S.; Sigfusson, B.; Gunnarsson, I.; Sigurdardottir, H.; Gunnlaugsson, E.; Axelsson, G.; Alfredsson, H. A.; Wolff-Boenisch, D.; Mesfin, K.; Taya, D. F. D.; Hall, J.; Dideriksen, K.; Broecker, W. S., Rapid carbon mineralization for permanent disposal of anthropogenic carbon dioxide emissions. *Science* **2016,** *352*, (6291), 1312-1314.

20. Gislason, S. R.; Oelkers, E. H., Carbon Storage in Basalt. *Science* **2014,** *344*, (6182), 373-374.

21. Alfredsson, H. A.; Oelkers, E. H.; Hardarsson, B. S.; Franzson, H.; Gunnlaugsson, E.; Gislason, S. R., The geology and water chemistry of the Hellisheidi, SW-Iceland carbon storage site. *Int J Greenh Gas Con* **2013,** *12*, 399-418.

22. McGrail, B. P.; Schaef, H. T.; Spane, F. A.; Cliff, J. B.; Qafoku, O.; Horner, J. A.; Thompson, C. J.; Owen, A. T.; Sullivan, C. E., Field Validation of Supercritical CO_2 Reactivity with Basalts. *Environmental Science & Technology Letters* **2017,** *4*, (1), 6-10.

23. Sissmann, O.; Brunet, F.; Martinez, I.; Guyot, F.; Verlaguet, A.; Pinquier, Y.; Daval, D., Enhanced Olivine Carbonation within a Basalt as Compared to Single-Phase Experiments: Reevaluating the Potential of CO_2 Mineral Sequestration. *Environ Sci Technol* **2014,** *48*, (10), 5512-5519.

24. Gislason, S. R.; Oelkers, E. H., Mechanism, rates, and consequences of basaltic glass dissolution: II. An experimental study of the dissolution rates of basaltic glass as a function of pH and temperature. *Geochim Cosmochim Ac* **2003,** *67*, (20), 3817-3832.

25. Gysi, A. P.; Stefansson, A., CO_2-water-basalt interaction. Low temperature experiments and implications for CO_2 sequestration into basalts. *Geochim Cosmochim Ac* **2012,** *81*, 129-152.

26. Gysi, A. P.; Stefansson, A., Mineralogical aspects of CO_2 sequestration during hydrothermal basalt alteration - An experimental study at 75 to 250 °C and elevated pCO_2. *Chemical Geology* **2012,** *306*, 146-159.

27. Xiong, W.; Giammar, D., Forsterite Carbonation in Zones with Transport Limited by Diffusion. *Environmental Science & Technology Letters* **2014,** *1*, (8), 333-338.

28. Kevitiyagala, N., Carbon sequestration. *Science* **2009,** *325*, (5948), 1644-1645.

29. Xu, T. F.; Apps, J. A.; Pruess, K., Mineral sequestration of carbon dioxide in a sandstone-shale system. *Chemical Geology* **2005,** *217*, (3-4), 295-318.

30. McGrail, B. P.; Schaef, H. T.; Ho, A. M.; Chien, Y. J.; Dooley, J. J.; Davidson, C. L., Potential for carbon dioxide sequestration in flood basalts. *Journal of Geophysical Research: Solid Earth* **2006,** *111*, (B12).

31. DOE, U. S., *Carbon Storage Technology Program Plan*. National Energy Technology Laboratory: 2013.

32. Gislason, S. R.; Oelkers, E. H., Carbon storage in basalt. *Science* **2014,** *344*, 373-374.

33. Chen, Y.; Brantley, S. L., Dissolution of forsteritic olivine at 65 °C and 2 < pH < 5. *Chemical Geology* **2000,** *165*, (3-4), 267-281.

34. Rosso, J. J.; Rimstidt, J. D., A high resolution study of forsterite dissolution rates. *Geochim Cosmochim Ac* **2000,** *64*, (5), 797-811.

35. Giammar, D. E.; Bruant, R. G.; Peters, C. A., Forsterite dissolution and magnesite precipitation at conditions relevant for deep saline aquifer storage and sequestration of carbon dioxide. *Chemical Geology* **2005,** *217*, (3-4), 257-276.

36. Hanchen, M.; Prigiobbe, V.; Storti, G.; Seward, T. M.; Mazzotti, M., Dissolution kinetics of fosteritic olivine at 90-150 degrees C including effects of the presence of CO_2. *Geochim. Cosmochim. Acta* **2006,** *70*, (17), 4403-4416.

37. Case, D. H.; Wang, F.; Giammar, D. E., Precipitation of Magnesium Carbonates as a Function of Temperature, Solution Composition, and Presence of a Silicate Mineral Substrate. *Environmental Engineering Science* **2011,** *28*, (12), 881-889.

38. Wang, F.; Giammar, D. E., Forsterite Dissolution in Saline Water at Elevated Temperature and High CO_2 Pressure. *Environ Sci Technol* **2013,** *47*, (1), 168-173.

39. Andreani, M.; Luquot, L.; Gouze, P.; Godard, M.; Hoise, E.; Gibert, B., Experimental Study of Carbon Sequestration Reactions Controlled by the Percolation of CO_2-Rich Brine through Peridotites. *Environ Sci Technol* **2009,** *43*, (4), 1226-1231.

40. Ellis, B.; Peters, C.; Fitts, J.; Bromhal, G.; Mclntyre, D.; Warzinski, R.; Rosenbaum, E., Deterioration of a fractured carbonate caprock exposed to CO_2-acidified brine flow. *Greenhouse Gases: Sci. Technol.* **2011,** *1*, (3), 248-260.

41. Gebrehiwet, T.; Guo, L.; Fox, D.; Huang, H.; Fujita, Y.; Smith, R.; Henriksen, J.; Redden, G., Precipitation of calcium carbonate and calcium phosphate under diffusion controlled mixing. *Appl. Geochem.* **2014,** *46*, 43-56.

42. Hovelmann, J.; Austrheim, H.; Jamtveit, B., Microstructure and porosity evolution during experimental carbonation of a natural peridotite. *Chemical Geology* **2012,** *334*, 254-265.

43. van Noort, R.; Spiers, C. J.; Drury, M. R.; Kandianis, M. T., Peridotite dissolution and carbonation rates at fracture surfaces under conditions relevant for in situ mineralization of CO_2. *Geochim Cosmochim Ac* **2013,** *106*, 1-24.

44. Hohmeyer, O.; Trittin, T., *The possible role and contribution of geothermal energy to the mitigation of climate change*. IPCC Scoping Meeting on Renewable Energy Sources: Luebeck, Germany, 2013; p 59-80.

45. Mohanan, K.; Sharma, S. K.; Bishop, F. C., A Raman Spectral Study of Forsterite-Monticellite Solid-Solutions. *American Mineralogist* **1993,** *78*, (1-2), 42-48.

46. Edwards, H. G. M.; Villar, S. E. J.; Jehlicka, J.; Munshi, T., FT-Raman spectroscopic study of calcium-rich and magnesium-rich carbonate minerals. *Spectrochimica Acta Part a-Molecular and Biomolecular Spectroscopy* **2005,** *61*, (10), 2273-2280.

47. Chopelas, A., Single-Crystal Raman-Spectra of Forsterite, Fayalite, and Monticellite. *American Mineralogist* **1991,** *76*, (7-8), 1101-1109.

48. Gillet, P.; Biellmann, C.; Reynard, B.; Mcmillan, P., Raman-Spectroscopic Studies of Carbonates .1. High-Pressure and High-Temperature Behavior of Calcite, Magnesite, Dolomite and Aragonite. *Phys. Chem. Miner.* **1993,** *20*, (1), 1-18.

49. Yang, L.; Steefel, C. I.; Bechtel, H., Microfluidic and Capillary Tube Experimental Study of Forsterite Carbonation by CO2 Bearing Fluids. *American Geophysical Union Fall Meeting* **2013,** *abstract #V41A-2773*.

50. Felmy, A. R.; Qafoku, O.; Arey, B. W.; Hu, J. Z.; Hu, M.; Schaef, H. T.; Ilton, E. S.; Hess, N. J.; Pearce, C. I.; Feng, J.; Rosso, K. M., Reaction of water-saturated supercritical CO_2 with forsterite: Evidence for magnesite formation at low temperatures. *Geochim. Cosmochim. Acta* **2012,** *91*, 271-282.

51. Kwak, J. H.; Hu, J. Z.; Hoyt, D. W.; Sears, J. A.; Wang, C. M.; Rosso, K. M.; Felmy, A. R., Metal carbonation of forsterite in supercritical CO_2 and H_2O using solid state Si^{29}, C^{13} NMR spectroscopy. *J. Phys. Chem. C* **2010,** *114*, (9), 4126-4134.

52. Jamtveit, B.; Malthe-Sorenssen, A.; Kostenko, O., Reaction enhanced permeability during retrogressive metamorphism. *Earth Planet. Sci. Lett.* **2008,** *267*, (3-4), 620-627.

53. Fletcher, R. C.; Buss, H. L.; Brantley, S. L., A spheroidal weathering model coupling porewater chemistry to soil thicknesses during steady-state denudation. *Earth Planet. Sci. Lett.* **2006,** *244*, (1-2), 444-457.

54. Duan, Z. H.; Sun, R., An improved model calculating CO_2 solubility in pure water and aqueous NaCl solutions from 273 to 533 K and from 0 to 2000 bar. *Chemical Geology* **2003,** *193*, (3-4), 257-271.

55. Xiong, W.; Wells, R. K.; Giammar, D. E., Carbon Sequestration in Olivine and Basalt Powder Packed Beds. *Environ Sci Technol* **2017,** *51*, (4), 2105-2112.

56. Gislason, S. R.; Wolff-Boenisch, D.; Stefansson, A.; Oelkers, E. H.; Gunnlaugsson, E.; Sigurdardottir, H.; Sigfusson, B.; Broecker, W. S.; Matter, J. M.; Stute, M.; Axelsson, G.; Fridriksson, T., Mineral sequestration of carbon dioxide in basalt: A pre-injection overview of the CarbFix project. *Int J Greenh Gas Con* **2010,** *4*, (3), 537-545.

57. Schaef, H. T.; McGrail, B. P.; Owen, A. T., Carbonate mineralization of volcanic province basalts. *Int J Greenh Gas Con* **2010,** *4*, (2), 249-261.

58. Garcia, B.; Beaumont, V.; Perfetti, E.; Rouchon, V.; Blanchet, D.; Oger, P.; Dromart, G.; Huc, A. Y.; Haeseler, F., Experiments and geochemical modelling of CO_2 sequestration by olivine: Potential, quantification. *Appl Geochem* **2010,** *25*, (9), 1383-1396.

59. Schaef, H. T.; Horner, J. A.; Owen, A. T.; Thompson, C. J.; Loring, J. S.; McGrail, B. P., Mineralization of Basalts in the CO_2-H_2O-SO_2-O_2 System. *Environ Sci Technol* **2014,** *48*, (9), 5298-5305.

60. Alcantar, N.; Israelachvili, J.; Boles, J., Forces and ionic transport between mica surfaces: Implications for pressure solution. *Geochim Cosmochim Ac* **2003,** *67*, (7), 1289-1304.

61. Niemeijer, A.; Spiers, C. J.; Bos, B., Compaction creep of quartz sand at 400-600 °C: experimental evidence for dissolution-controlled pressure solution. *Earth and Planetary Science Letters* **2002,** *195*, (3-4), 261-275.

62. de Meer, S.; Spiers, C. J.; Nakashima, S., Structure and diffusive properties of fluid-filled grain boundaries: An in-situ study using infrared (micro) spectroscopy. *Earth and Planetary Science Letters* **2005,** *232*, (3-4), 403-414.

63. Giammar, D. E.; Wang, F.; Guo, B.; Surface, J. A.; Peters, C. A.; Conradi, M. S.; Hayes, S. E., Impacts of Diffusive Transport on Carbonate Mineral Formation from Magnesium Silicate-CO_2-Water Reactions. *Environ Sci Technol* **2014,** *48*, (24), 14344-14351.

64. Wells, R.; Giammar, D.; Skemer, P. *Sample Library of Natural and Artificial Basalts*; 2016.

65. Oelkers, E. H.; Gislason, S. R., The mechanism, rates and consequences of basaltic glass dissolution: I. An experimental study of the dissolution rates of basaltic glass as a function of aqueous Al, Si and oxalic acid concentration at 25 °C and pH=3 and 11. *Geochim Cosmochim Ac* **2001,** *65*, (21), 3671-3681.

66. Saldi, G. D.; Daval, D.; Morvan, G.; Knauss, K. G., The role of Fe and redox conditions in olivine carbonation rates: An experimental study of the rate limiting reactions at 90 and 150 °C in open and closed systems. *Geochim Cosmochim Ac* **2013,** *118*, 157-183.

67. Boulard, E.; Guyot, F.; Fiquet, G., The influence on Fe content on Raman spectra and unit cell parameters of magnesite–siderite solid solutions. *Physics and Chemistry of Minerals* **2012,** *39*, (3), 239-246.

68. Qafoku, O.; Kovarik, L.; Kukkadapu, R. K.; Ilton, E. S.; Arey, B. W.; Tucek, J.; Felmy, A. R., Fayalite dissolution and siderite formation in water-saturated supercritical CO_2. *Chemical Geology* **2012,** *332*, 124-135.

69. Laurora, A.; Brigatti, M. F.; Malferrari, D.; Galli, E.; Rossi, A.; Ferrari, M., The Crystal Chemistry of Lizardite-1t from Northern Apennines Ophiolites near Modena, Italy. *Canadian Mineralogist* **2011,** *49*, (4), 1045-1054.

70. Pham, V. T. H.; Lu, P.; Aagaard, P.; Zhu, C.; Hellevang, H., On the potential of CO_2-water-rock interactions for CO_2 storage using a modified kinetic model. *Int J Greenh Gas Con* **2011,** *5*, (4), 1002-1015.

71. Gysi, A. P.; Stefansson, A., CO_2-water-basalt interaction. Numerical simulation of low temperature CO_2 sequestration into basalts. *Geochim Cosmochim Ac* **2011,** *75*, (17), 4728-4751.

72. Gysi, A. P.; Stefansson, A., Experiments and geochemical modeling of CO_2 sequestration during hydrothermal basalt alteration. *Chemical Geology* **2012,** *306*, 10-28.

73. Greenberg, J.; Tomson, M., Precipitation and Dissolution Kinetics and Equilibria of Aqueous Ferrous Carbonate Vs Temperature. *Appl Geochem* **1992,** *7*, (2), 185-190.

74. Jensen, D. L.; Boddum, J. K.; Tjell, J. C.; Christensen, T. H., The solubility of rhodochrosite ($MnCO_3$) and siderite ($FeCO_3$) in anaerobic aquatic environments. *Appl Geochem* **2002,** *17*, (4), 503-511.

75. Saar, M. O.; Manga, M., Permeability-porosity relationship in vesicular basalts. *Geophysical Research Letters* **1999,** *26*, (1), 111-114.

76. Schrag, D. P., Preparing to capture carbon. *Science* **2007,** *315*, (5813), 812-813.

77. Kintisch, E., New solution to carbon pollution? *Science* **2016,** *352*, (6291), 1262-1263.

78. Benson, S. M.; Cole, D. R., CO_2 sequestration in deep sedimentary formations. *Elements* **2008,** *4*, (5), 325-331.

79. Snæbjörnsdóttir, S. Ó.; Oelkers, E. H.; Mesfin, K.; Aradóttir, E. S.; Dideriksen, K.; Gunnarsson, I.; Gunnlaugsson, E.; Matter, J. M.; Stute, M.; Gislason, S. R., The chemistry and saturation states of subsurface fluids during the in situ mineralisation of CO_2 and H_2S at the CarbFix site in SW-Iceland. *Int J Greenh Gas Con* **2017,** *58*, 87-102.

80. Schaef, H. T.; McGrail, B. P.; Owen, A. T., Basalt reactivity variability with reservoir depth in supercritical CO_2 and aqueous phases. *Energy Procedia* **2011,** *4*, 4977-4984.

81. Wells, R. K.; Xiong, W.; Sesti, E.; Cui, J.; Giammar, D.; Skemer, P.; Hayes, S. E.; Conradi, M. S., Spatially-variable carbonation reactions in polycrystalline olivine. *Geochim Cosmochim Ac* **2017,** *204*, 252-266.

82. Sommer, C.; Straehle, C.; Koethe, U.; Hamprecht, F. A. In *Ilastik: Interactive learning and segmentation toolkit*, Biomedical Imaging: From Nano to Macro, 2011 IEEE International Symposium on, 2011; IEEE: 2011; pp 230-233.

83. Steefel, C. I.; Appelo, C. A. J.; Arora, B.; Jacques, D.; Kalbacher, T.; Kolditz, O.; Lagneau, V.; Lichtner, P. C.; Mayer, K. U.; Meeussen, J. C. L.; Molins, S.; Moulton, D.; Shao, H.; Simunek, J.; Spycher, N.; Yabusaki, S. B.; Yeh, G. T., Reactive transport codes for subsurface environmental simulation. *Computational Geosciences* **2015,** *19*, (3), 445-478.

84. Cadogan, S. P.; Maitland, G. C.; Trusler, J. M., Diffusion Coefficients of CO_2 and N_2 in Water at Temperatures between 298.15 K and 423.15 K at Pressures up to 45 MPa. *Journal of Chemical & Engineering Data* **2014,** *59*, (2), 519-525.

85. Pokrovsky, O. S.; Golubev, S. V.; Schott, J., Dissolution kinetics of calcite, dolomite and magnesite at 25 °C and 0 to 50 atm pCO_2. *Chemical Geology* **2005,** *217*, (3-4), 239-255.

86. Pokrovsky, O. S.; Schott, J., Surface chemistry and dissolution kinetics of divalent metal carbonates. *Environ Sci Technol* **2002,** *36*, (3), 426-432.

87. Tester, J. W.; Worley, W. G.; Robinson, B. A.; Grigsby, C. O.; Feerer, J. L., Correlating Quartz Dissolution Kinetics in Pure Water from 25 °C to 625 °C. *Geochim Cosmochim Ac* **1994,** *58*, (11), 2407-2420.

88. Kaiser, K.; Guggenberger, G., Mineral surfaces and soil organic matter. *European Journal of Soil Science* **2003,** *54*, (2), 219-236.

89. Palandri, J. L.; Kharaka, Y. K. *A compilation of rate parameters of water-mineral interaction kinetics for application to geochemical modeling*; DTIC Document: 2004.

90. Teir, S.; Revitzer, H.; Eloneva, S.; Fogelholm, C. J.; Zevenhoven, R., Dissolution of natural serpentinite in mineral and organic acids. *International Journal of Mineral Processing* **2007,** *83*, (1-2), 36-46.

91. Orlando, A.; Borrini, D.; Marini, L., Dissolution and carbonation of a serpentinite: Inferences from acid attack and high P-T experiments performed in aqueous solutions at variable salinity. *Appl Geochem* **2011,** *26*, (8), 1569-1583.

92. Knauss, K. G.; Johnson, J. W.; Steefel, C. I., Evaluation of the impact of CO_2, co-contaminant gas, aqueous fluid and reservoir rock interactions on the geologic sequestration of CO_2. *Chemical Geology* **2005,** *217*, (3), 339-350.

93. Golubev, S. V.; Benezeth, P.; Schott, J.; Dandurand, J. L.; Castillo, A., Siderite dissolution kinetics in acidic aqueous solutions from 25 to 100 °C and 0 to 50 atm pCO_2. *Chemical Geology* **2009,** *265*, (1-2), 13-19.

94. Carroll, S. A.; McNab, W. W.; Dai, Z. R.; Torres, S. C., Reactivity of Mount Simon Sandstone and the Eau Claire Shale Under CO_2 Storage Conditions. *Environ Sci Technol* **2013,** *47*, (1), 252-261.

95. Schneider, C. A.; Rasband, W. S.; Eliceiri, K. W., NIH Image to ImageJ: 25 years of image analysis. *Nature Methods* **2012,** *9*, (7), 671-675.

96. Thevenaz, P.; Ruttimann, U. E.; Unser, M., A pyramid approach to subpixel registration based on intensity. *Ieee Transactions on Image Processing* **1998,** *7*, (1), 27-41.

97. Goff, F.; Lackner, K., Carbon dioxide sequestering using ultramafic rocks. *Environmental Geosciences* **1998,** *5*, (3), 89-101.

98. Luhmann, A. J.; Tutolo, B. M.; Tan, C.; Moskowitz, B. M.; Saar, M. O.; Seyfried, W. E., Whole rock basalt alteration from CO_2-rich brine during flow-through experiments at 150° C and 150bar. *Chemical Geology* **2017,** *453*, 92-110.

99. Luhmann, A. J.; Tutolo, B. M.; Bagley, B. C.; Mildner, D. F.; Seyfried, W. E.; Saar, M. O., Permeability, porosity, and mineral surface area changes in basalt cores induced by reactive transport of CO_2-rich brine. *Water Resources Research* **2017**.

100. De Villiers, J. P. R. The Crystal Structures of Aragonite, Strontianite, and Witherite. University of Illinois at Urbana-Champaign, 1967.

101. Spek, A., Single-crystal structure validation with the program PLATON. *Journal of Applied Crystallography* **2003,** *36*, (1), 7-13.

102. Morse, J. W.; Arvidson, R. S.; Luttge, A., Calcium carbonate formation and dissolution. *Chemical Reviews* **2007,** *107*, (2), 342-381.

103. Morse, J. W.; Wang, Q.; Tsio, M. Y., Influences of temperature and Mg: Ca ratio on $CaCO_3$ precipitates from seawater. *Geology* **1997,** *25*, (1), 85-87.

104. Wiese, F.; Fridriksson, T.; Ármannsson, H. *www.os.is/gogn/Skyrslur/ISOR-2008/ISOR-2008-003.pdf*; Iceland Geosurvey: 2008.

105. Xu, T. F.; Apps, J. A.; Pruess, K., Numerical simulation of CO_2 disposal by mineral trapping in deep aquifers. *Appl Geochem* **2004,** *19*, (6), 917-936.

106. Gribb, T. T.; Cooper, R. F., Low-frequency shear attenuation in polycrystalline olivine: Grain boundary diffusion and the physical significance of the Andrade model for viscoelastic rheology. *Journal of Geophysical Research-Solid Earth* **1998,** *103*, (B11), 27267-27279.

107. Moore, J. K.; Surface, J. A.; Brenner, A.; Wang, L. S.; Skemer, P.; Conradi, M. S.; Hayes, S. E., Quantitative Identification of Metastable Magnesium Carbonate Minerals by Solid-State C-13 NMR Spectroscopy. *Environ Sci Technol* **2015,** *49*, (3), 1986-1986.

108. Davies, P. J.; Bubela, B., The transformation of nesquehonite into hydromagnesite. *Chemical Geology* **1973,** *12*, (4), 289-300.

109. Hanchen, M.; Prigiobbe, V.; Baciocchi, R.; Mazzotti, M., Precipitation in the Mg-carbonate system - effects of temperature and CO_2 pressure. *Chemical Engineering Science* **2008,** *63*, (4), 1012-1028.

110. Surface, J. A.; Skemer, P.; Hayes, S. E.; Conradi, M. S., In Situ Measurement of Magnesium Carbonate Formation from CO_2 Using Static High-Pressure and -Temperature ^{13}C NMR. *Environ Sci Technol* **2013,** *47*, (1), 119-125.

111. Qafoku, O.; Hu, J. Z.; Hess, N. J.; Hu, M. Y.; Ilton, E. S.; Feng, J.; Arey, B. W.; Felmy, A. R., Formation of submicron magnesite during reaction of natural forsterite in H_2O-saturated supercritical CO_2. *Geochim Cosmochim Ac* **2014,** *134*, 197-209.

112. Pokrovsky, O. S.; Schott, J., Kinetics and mechanism of forsterite dissolution at 25 °C and pH from 1 to 12. *Geochim Cosmochim Ac* **2000,** *64*, (19), 3313-3325.

113. Jarvis, K.; Carpenter, R. W.; Windman, T.; Kim, Y.; Nunez, R.; Alawneh, F., Reaction Mechanisms for Enhancing Mineral Sequestration of CO_2. *Environ Sci Technol* **2009,** *43*, (16), 6314-6319.

114. Daval, D.; Sissmann, O.; Menguy, N.; Saldi, G. D.; Guyot, F.; Martinez, I.; Corvisier, J.; Garcia, B.; Machouk, I.; Knauss, K. G.; Hellmann, R., Influence of amorphous silica layer formation on the dissolution rate of olivine at 90 °C and elevated pCO_2. *Chemical Geology* **2011,** *284*, (1-2), 193-209.

115. Olsson, J.; Bovet, N.; Makovicky, E.; Bechgaard, K.; Balogh, Z.; Stipp, S. L. S., Olivine reactivity with CO_2 and H_2O on a microscale: Implications for carbon sequestration. *Geochim Cosmochim Ac* **2012,** *77*, 86-97.

116. Sissmann, O.; Daval, D.; Brunet, F.; Guyot, F.; Verlaguet, A.; Pinquier, Y.; Findling, N.; Martinez, I., The deleterious effect of secondary phases on olivine carbonation yield: Insight from time-resolved aqueous-fluid sampling and FIB-TEM characterization. *Chemical Geology* **2013,** *357*, 186-202.

117. King, H. E.; Plumper, O.; Geisler, T.; Putnis, A., Experimental investigations into the silicification of olivine: Implications for the reaction mechanism and acid neutralization. *American Mineralogist* **2011,** *96*, (10), 1503-1511.

118. Casey, W. H.; Westrich, H. R.; Banfield, J. F.; Ferruzzi, G.; Arnold, G. W., Leaching and Reconstruction at the Surfaces of Dissolving Chain-Silicate Minerals. *Nature* **1993,** *366*, (6452), 253-256.

119. Gaus, I., Role and impact of CO_2-rock interactions during CO_2 storage in sedimentary rocks. *Int J Greenh Gas Con* **2010,** *4*, (1), 73-89.

120. Lin, H.; Fujii, T.; Takisawa, R.; Takahashi, T.; Hashida, T., Experimental evaluation of interactions in supercritical CO_2/water/rock minerals system under geologic CO_2 sequestration conditions. *J Mater Sci* **2008,** *43*, (7), 2307-2315.

121. Spycher, N.; Pruess, K.; Ennis-King, J., CO_2-H_2O mixtures in the geological sequestration of CO_2. I. Assessment and calculation of mutual solubilities from 12 to 100 °C and up to 600 bar. *Geochim Cosmochim Ac* **2003,** *67*, (16), 3015-3031.

122. Loring, J. S.; Thompson, C. J.; Wang, Z. M.; Joly, A. G.; Sklarew, D. S.; Schaef, H. T.; Ilton, E. S.; Rosso, K. M.; Felmy, A. R., In Situ Infrared Spectroscopic Study of Forsterite Carbonation in Wet Supercritical CO_2. *Environ Sci Technol* **2011,** *45*, (14), 6204-6210.

123. Kwak, J. H.; Hu, J. Z.; Turcu, R. V. F.; Rosso, K. M.; Ilton, E. S.; Wang, C. M.; Sears, J. A.; Engelhard, M. H.; Felmy, A. R.; Hoyt, D. W., The role of H_2O in the carbonation of forsterite in supercritical CO_2. *Int J Greenh Gas Con* **2011,** *5*, (4), 1081-1092.

124. Schaef, H. T.; McGrail, B. P.; Loring, J. L.; Bowden, M. E.; Arey, B. W.; Rosso, K. M., Forsterite [Mg_2SiO_4] Carbonation in Wet Supercritical CO_2: An in Situ High-Pressure X-ray Diffraction Study. *Environ Sci Technol* **2013,** *47*, (1), 174-181.